

DISS. ETH Nr.

**Quantum Phase Transitions
in a Magnetic Model System**

ABHANDLUNG

zur Erlangung des Titels

DOKTOR DER WISSENSCHAFTEN

der

ETH ZÜRICH

vorgelegt von

CONRADIN KRAEMER

Dipl. Phys. ETH, ETH Zürich

geboren am 31.08.1981

von Bern

Angenommen auf Antrag von

Prof. Dr. M. Sigrist, Referent

Prof. Dr. H. Rønnow, Korreferent

Prof. Dr. J. Mesot, Korreferent

2009

Zusammenfassung

Ein Model bestehend aus magnetischen Momenten gekoppelt alleine durch die schwachen aber grundlegenden Dipol-Dipol Wechselwirkungen ist zweifellos der Archetypus eines magnetischen Festkörpers. Die Isolatoren LiReF_4 , wobei Re für ein Element der seltenen Erde steht, stellen einzigartige, nahezu ideale Realisierungen eines solchen Systems dar. Obwohl die ersten Studien zurückreichen bis an die Anfänge der Diskussion von Phasenübergängen im Rahmen der Renormalisierungsgruppentheorie, blieb das Interesse an diesen Materialien bis heute ungebrochen, da sie bestens geeignet sind zur Untersuchung einer Vielzahl von Kollektiven Phänomenen, einschließlich Quantenkritikalität und Spin Glasser, die relevant sind für viele Hauptgebiete zeitgenössischer Festkörperphysik. Hier wird eine umfassende experimentelle Studie vorgelegt mit Hauptaugenmerk auf Neutronenstreuungen an LiHoF_4 , LiHoYF_4 und dem bisher beinahe unerforschten LiErF_4 . Zusätzlich wurde eine Charakterisierung des Kristallfeld in diversen LiReF_4 durchgeführt. – Der Ferromagnet LiHoF_4 wird als Paradebeispiel des transversal Feld Ising Models angesehen. Aufgrund des transversalen Feldes werden in einem an sich klassischen System Quantenfluktuationen induziert und in Folge dessen ein Quantenphasenübergang evoziert. Die schwache hyperfine Wechselwirkung stört allerdings in LiHoF_4 das kritische Verhalten, u.a. existiert kein Softmode am kritischen Punkt. Ein erhöhen der Temperatur reduziert die Koppelung an das Spin Bad und damit auch die besagten Effekte. In LiHoYF_4 erinnert sich das System, wie es in der Vergangenheit präpariert wurde, d.h. entweder im Feld gekühlt oder nicht. Die Glas Phase manifestiert sich entweder dann als lang reichweitig geordneter oder als ungeordneter aber korrelierter Zustand. Die althergebrachte Vorhersage über Antiferromagnetismus hervorgerufen durch Dipol-Wechselwirkung fand im planeren, schichtweise geordneten System LiErF_4 eine eindruckliche Bestätigung. Bereits bei einem geringen Feld erfolgt ein Quantenphasenübergang einhergehend mit einem dem weich werden der charakteristischen Moden am kritischen Punkt. Im weiteren wurden die Spektren in beiden Phasen bestimmt. Aufgrund der gemessenen kritischen Exponenten wird der thermische Phasenübergang der Universalitätsklasse eines 2-dimensionalen XY/h_4 Models zugeordnet, LiErF_4 zeigt folglich reduzierte Dimensionalität. Die Symmetrie Brechung geht zurück auf den Mechanismus von order-by-disorder.

Abstract

Certainly the most fundamental model of an archetypical magnetic solid is constituted by an array of spins interacting with each other only by the weak but elementary dipolar forces. The insulators of the family LiReF_4 , where Re stands for a rare earth element, represent an exceptionally clean and well characterized physical realization of such a system. Although the first extensive investigations were motivated by the advent of renormalization group theory decades ago, a broad interest in these compounds still continuous, because they host an ideal arena to study a variety of collective phenomena, including quantum criticality and spin glasses, which are relevant in several major fields in contemporary solid state physics. Here, a comprehensive neutron scattering investigation is presented, which was mainly focused on LiHoF_4 , its dilution series LiHoYF_4 and the so far unexplored LiErF_4 . Additionally, a full characterization of the crystal fields in various compounds was performed, that is inevitable for all further studies on collective phenomena. – LiHoF_4 is referred as the textbook realization of the transverse field Ising Model. Applying a transversal field is the natural way to introduce quantum fluctuations to an in fact classical system and evoke a quantum phase transition. However in LiHoF_4 quantum criticality is affected by the marginal hyperfine interaction with the nuclear moments, leading for example to an incomplete softening of the characteristic excitations at the critical point. The coupling to spin bath and the associated effects are governed by temperature. One of the most remarkable further results was the discovery of new aspects of a history dependent behavior in the random field magnet LiHoYF_4 . In the low temperature spin glass like phase the system can be prepared either in a short range correlated but disordered or long range ferromagnetic ordered state by choosing the appropriate annealing protocol, i.e. field cooling or zero field cooling, respectively. The studies on LiErF_4 directly address a longstanding prediction of antiferromagnetism induced by dipolar interactions. It could be demonstrated that the system is a realization of a planar antiferromagnet that exhibits layered ordering and undergoes a quantum phase transition in decent magnetic field. The excitation spectra was mapped out in the ordered phase as well as in the high-field phase. Remarkably the system exhibits a complete softening of the characteristic excitations when approaching the critical field, regarded as one of the hallmarks of a quantum phase transition. Furthermore, as a conclusion drawn from the critical exponents, the thermal phase transition falls into the 2D universality class XY/h_4 , implying that dimensional reduction takes place. The emergence of symmetry breaking is interpreted as a consequence of the effect referred as “order-by-disorder”.

Contents

1	Introduction	1
1.1	Quantum Phase Transitions	1
1.2	Spin Glass Physics	3
1.3	The LiReF ₄ System - Review of Research	5
1.4	Outline of this Work	6
2	Materials and Methods	8
2.1	The Compound LiReF ₄	8
2.2	Neutron scattering	9
2.2.1	Theory of Neutron Scattering	9
2.2.2	Neutron Scattering Techniques	13
2.3	Complementary Methods	16
2.4	Generic Models for Excitations, Correlation and Relaxation .	17
2.5	Sample Setup and Experimental Remarks	19
3	Aspects of Theory	23
3.1	Hamiltonian	23
3.1.1	Crystal Field	24
3.1.2	Magnetic Interactions	26
3.2	Transverse Field Ising Model - RPA/MF	27
3.3	LiReF ₄ System RPA/MF	32
3.4	Random Field Model Systems	36
4	Experimental Results and Discussion	38
4.1	Crystal Fields	38

4.1.1	Symmetry Arguments and General Considerations . . .	39
4.1.2	LiErF ₄	40
4.1.3	LiHoF ₄	44
4.1.4	LiHo _x Y _{1-x} F ₄ and the Effect of Dilution	46
4.1.5	LiTmF ₄	47
4.1.6	LiYbF ₄	51
4.2	LiHo _x Y _{1-x} F ₄	54
	Annealing Protocols	54
4.2.1	Ising Ferromagnet, Random Field Magnet, Spin Glass	55
	Phase Diagram	55
	$x = 0.83$	56
	$x = 0.67$ - Emergence of Hysteretic Effects	57
	$x = 0.25$	59
	$x = 0.20$ - The Marginal Concentration	60
4.2.2	LiHo _x Y _{1-x} F ₄ , $x = 1/3 - 1/2$	63
	Re-Entrant Spin Glass	63
	Magnetic Correlations and Critical Scattering	66
	Quantum Annealing - Susceptibility Results	67
	Quantum Annealing - Neutron Diffraction Results	70
	Conclusions	73
4.2.3	LiHo _x Y _{1-x} F ₄ , $x = 0.045$	75
	The Anti-Glass	75
	Coherent Oscillations of Spin Clusters	76
	Time-Resolved SANS	77
4.3	LiHoF ₄ - Quantum Magnet in a Spin Bath	80
4.3.1	Spin Bath and Decoherence	80
4.3.2	Nuclear-Electronic Criticality	82
4.3.3	Temperature Effects	84
4.3.4	Effective model	87
4.3.5	Conclusion and Outlook	91
4.4	LiErF ₄ - QPT in a dipolar XY-Antiferromagnet	94
4.4.1	Phase Diagram and Magnetic Structure	94

4.4.2	Specific Heat	98
4.4.3	Order by Disorder	100
4.4.4	Universality Class	101
4.4.5	Magnetic Correlations	102
4.5	LiErF ₄ - Excitations and Critical Dynamics	106
4.5.1	Excitations in the ordered phase at $H = 0$ T	106
4.5.2	Excitations in the phase above H_c	109
4.5.3	Softmodes at QPT	110
4.5.4	Conclusions	113
4.6	LiHo _{<i>x</i>} Er _{1-<i>x</i>} F ₄	114
4.6.1	Phase Diagram	114
4.6.2	Magnetic Correlations in LiHo _{0.25} Er _{0.75} F ₄	115
5	Conclusions and Outlook	118
	Appendix	121
A	Crystallographic Details of LiReF ₄	121
B	Representation of the group S_4	123
	Bibliography	123

Chapter 1

Introduction

The phenomena of magnetism in condensed matter, although fascinating matter of natural philosophy and science since ancient times, remained mysterious and an unsolved problem until a century ago, the advent of quantum mechanics just provides the foundation of the theoretical description. This time was also the hour of birth of magnetic model systems, like the Ising, XY and Heisenberg models. Despite of the fact that they are useless to describe common metals like iron or nickel and only address the question of magnetism in rather exotic materials, these model systems have been thoroughly investigated in theory as well as experiment and played an important role in the development of fundamental concepts in statistical physics, like the theory of critical phenomena. Most aspects of conventional long range ordered magnets are nowadays well understood. However magnetism is still a vivid topic and omnipresent in applied science and technology. In contemporary fundamental solid-state physics research the focus of interest changed towards order parameter free magnets, where frustration, low dimensionality or dimerization cause novel exotic effects. Nevertheless, there is still an appeal in the traditional model systems, like the Ising model, and because of their simplicity and stringency they provide an ideal arena to elucidate fundamental concepts.

1.1 Quantum Phase Transitions

The discussion of critical phenomena has a long tradition in solid state physics and statistical physics in general. Currently the particular class of quantum phase transitions is attracting interest in various fields of strongly correlated systems ranging from quantum magnetism to heavy fermion and high-temperature superconductivity. To explain the term “quantum phase transition” in particular the meaning of ‘quantum’ one could relate to the

following definition [1, 2, 3].

Definition A quantum phase transition is a phase transition at $T = 0$ K between different quantum ground states as a non-thermal control parameter g entering in the Hamiltonian $\mathcal{H}(g)$ is varied.

Examples for such a tuning parameter g are applied pressure, magnetic fields or the variation of doping concentration. As a corollary to the above definition all finite temperature transition are classical. This does not mean that the system itself is classical, quantum mechanics may still play an inevitable role, but in the vicinity of the phase transition, at the length and timescales associated to criticality, the behavior is classical in the sense that the transition is governed by thermal fluctuations. Often it is said that in contrast to this quantum phase transitions are driven by so called quantum fluctuations, which are a consequence of Heisenberg's principle and therefore exist even at $T = 0$ K. The textbook example for a model showing a quantum phase transition is the ferromagnetically coupled Ising model in a transversal field (TFIM). In view of LiHoF_4 , which can be regarded as a physical realization of this model, a detailed discussion follows in a subsequent chapter.

$$\mathcal{H}_{TFIM} = -J \left(\sum_i \sigma_i^z \sigma_{i+1}^z + g \cdot \sigma_i^x \right). \quad (1.1.1)$$

A schematic phase diagram for quantum critical system either with or without occurrence of an ordered phase is shown in figure 1.1. The transition point $g = g_c$ and $T = 0$ K is called the critical point QCP. At this point the conventional quasi-particle picture valid for $g < g_c$ or $g > g_c$ breaks down and the system is characterized by a quantum critical ground state. The cone spreading out at $T > 0$ above the QCP is called the critical region, where the behavior is dominated by thermal fluctuations out of the quantum critical state. This manifests in unusual power laws of physical quantities. Critical behavior is associated with a typical timescale $\tau_c \propto \xi^z$ and spatial correlation length $\xi \propto |g - g_c|^{-\nu}$ of the long distance order parameter fluctuations which diverges at the continuous transition. Therefore, the crossover to the quantum critical region is dictated by the thermal energy,

$$k_B T \simeq \hbar \omega \propto |g - g_c|^{z\nu}. \quad (1.1.2)$$

Towards higher temperatures the quantum critical region is bounded, if $k_B T$ approach certain microscopic energy scales of the problem the system crosses over to an non-universal region. In the case of an ordinary transition to an ordered state already at finite temperatures, where $T_c(g)$ is suppressed by

g and finally terminates at the QCP, there exists around the phase boundary line also a classical critical region which is only dominated by classical fluctuations.

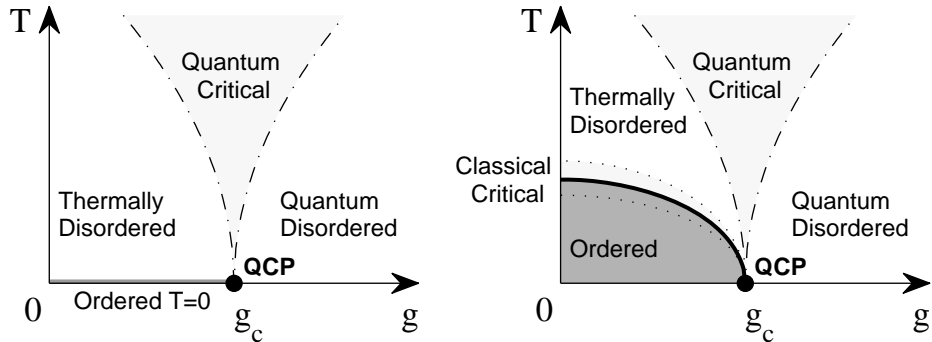


Figure 1.1: Schematic phase diagrams of two generic quantum critical systems. Either the ordered phase exists only at $T = 0$ (left) or persists towards finite nonzero temperatures (right).

The essential features of a quantum phase transition manifest in the mapping of the d -dimensional problem to a $d + z$ classical analogue [2, 3]. Here the extra dimensions are related formally to the imaginary time direction $\tau \in [0, \hbar\beta]$. Hence temperature introduces a finite size $L_\tau = \hbar\beta$ of the system and if τ_c exceeds L_τ a quantum-classical crossover from $d + z$ to d -dimensions is taking place. This is referred as finite-size scaling. Furthermore, in the vicinity of the phase transition the singular part of the free energy density can be expressed in form of a homogeneity law [3, 2]. This implies directly various universal scaling relations for static and dynamic observable, like for example the generalized susceptibility.

$$\mathcal{O}(t, k, \omega, T) = T^{-d_{\mathcal{O}}/z} \cdot \Phi\left(kT^{-1/z}, \frac{\omega}{T}, T\xi^z\right). \quad (1.1.3)$$

Here Φ is a scaling function associated to the observable \mathcal{O} , $d_{\mathcal{O}}$ the scaling dimension and k, ω denote wavevector and frequency, respectively. In particular at $g = g_c$ the correlation length diverges and considering the particular case $k = 0$ the function Φ depends on its second argument only and hence the observable fulfills a ω/T scaling relation.

1.2 Spin Glass Physics

Ordinary magnetic systems manifest themselves in various phases ranging from classical or quantum disordered to ordered. In a regular magnetic

system the evolution from disorder to order is associated with a phase transition which can be characterized by an ordering parameter and symmetry breaking. For spin glass systems there is no sharp transition but instead a freezing crossover to a state where the spins are aligned in a random manner (quenched disorder). Approaching the crossover temperature $T \rightarrow T_f^+$ is accompanied by increasing relaxation times and spin-spin correlation lengths, although there is still no clear evidence if there is a true divergence as known for critical systems [4]. The Edwards Anderson parameter $q_{EA} = [\langle S_i \rangle_T^2]_{av}$ is then often referred to as a kind of a spin glass order parameter, where $\langle \cdot \rangle_T$ denotes the thermodynamic average and $[\cdot]_{av}$ the configurational average. The physics of phase transitions is particularly well understood in the framework of Ginzburg-Landau and renormalization group theory, whereas the spin glass problem is still ambiguous in contemporary statistical physics. However, there are two general key ingredients that are characteristic for spin glass systems, namely randomness and frustration. In an intuitive picture a spin glass system may be identified by a complex free energy landscape. The system contains many energetically equally preferable configurations separated by large energy barriers. These energy barriers govern the relaxation dynamics and slow down the exploration of the free energy manifold such that the system is within the relevant time scale effectively trapped in small part of configuration space. This broken ergodicity and the resulting history dependent effects are further characteristics of spin glasses.

From an experimentalist point of view for the term spin glass can be defined according to three main criteria [4].

Definition A system is called a Spin Glass if there is

- Frozen-in magnetic moments below some freezing temperature T_f and hence a peak in the frequency-dependent susceptibility.
- Lack of periodic long-range magnetic order
- Remanence and magnetic relaxation on macroscopic time scales below T_f as response to a changing magnetic field.

A particular class of spin glasses form the so called quantum spin glasses. The defining property of these systems is that not only thermal fluctuations but also more important quantum fluctuations are able to drive the crossover from the frozen state to the non-glassy disordered phase. One can imagine two different scenarios either a quantum vector-spin-glass or starting from a classical spin glass and adding in the Hamiltonian as a perturbation a tunable quantum tunneling term. The simplest model for a quantum spin glass is the transverse field Ising spin glass (TFISG).

One topic is of particular interest in many investigations of quantum spin glasses: Quantum Annealing. However this term is not only related to spin

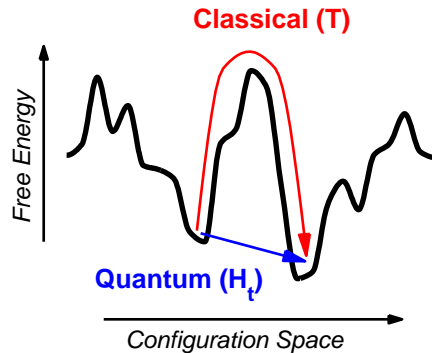


Figure 1.2: Quantum versus classical annealing in the transverse field Ising model. Schematic illustration of classical relaxation and quantum tunneling paths to find the optimal configuration with minimal free energy.

glasses and there is an affinity to other so called hard problems, like protein folding or the traveling sales problem.

Definition Quantum Annealing is a general optimization method to find the ground state of a complex system, i.e. the global minimum of the free energy functional. By adiabatically switching off an appropriate source of quantum fluctuations the initially complete disordered system settles into a local minimum, that should be comparable to the ground state.

In the transverse field Ising model two annealing protocols can be realized: classical annealing (CA) while decreasing adiabatically T at $H_t = 0$ or quantum annealing (QA) while decreasing H_t at $T = 0$. The route of relaxation to the optimal state involves either a thermally activated jumps over or quantum tunneling under the energy barriers in the complex energy configuration landscape, as depicted schematically in figure 1.2.

1.3 The LiReF₄ System - Review of Research

The compounds of the LiReF₄-series (Re=rare-earth) host a remarkably rich variety of collective quantum phenomena. Since the magnetic properties can be thoroughly characterized, these simple insulating materials offer ideal model systems, where experimental observations can be tested quantitatively by theory. The Hamiltonian is well established and it is possible to refine all parameters by experiments. The localized magnetic moments are

essentially affected by crystal field anisotropy and dominant long ranging and dipole-dipole interaction.

So far the research was mainly focused on the compound LiHoF_4 and its dilution series $\text{LiHo}_x\text{Y}_{1-x}\text{F}_4$, the host for a wide variety of phenomena, ranging from tunneling of single moments and domain walls to quantum annealing, entanglement and coherently oscillating spin clusters [5, 6, 7, 8]. The pure system is a physical realization of the famous transverse field Ising model, with ferromagnetic ordering below $T_c = 1.53$ K and a quantum critical point at $H_c = 5$ T [9]. As a function of dilution with nonmagnetic Yttrium the system evolves from a ferromagnet ($x = 1$) to a long range ordered ferromagnetic state with strong history dependent effects ($x = 0.44$), to a spin glass ($x = 0.1 - 0.3$) and to a spin liquid like phase ($x < 0.1$), which in literature is often referred as "antiglass"-state. Although the theorists still argue about several aspects of the understanding of the spin-glass compounds, it is agreed that the positional randomness introduced by the dilution through the dipole coupling and the transverse field lead to random fields along the Ising direction. The system can be considered as an almost perfect realization of the random field Ising model [10].

Although the effective Transverse field Ising model provides in the case of LiHoF_4 a good approximative description of the real system, inelastic neutron scattering [11] and susceptibility investigations [9] have demonstrated that the relatively weak hyperfine interaction to the nuclear spins, which acts as a spin bath, i.e. a bath of local degrees of freedom, in fact has dramatic effects on the phase diagram and the excitation spectrum around the quantum phase transition. The softening of the electronic mode remains incomplete, which can be regarded as a quantum decoherence effect, and the phase transition is shifted towards higher critical fields. This discovery makes LiHoF_4 an ideal system to study in a controlled way the robustness of quantum criticality in non-perfect (hence realistic) systems [12].

1.4 Outline of this Work

In the previous paragraph the concepts, terms and definitions relevant to the scientific case of LiReF_4 have been shortly introduced followed by a short exposition to the actual status of research, without the claim of completeness. The present work aims to continue the long-standing studies on $\text{Li}(\text{HoY})\text{F}_4$, pure as well as diluted compounds, and provide a complementary insight by means of an extended neutron scattering investigation. The topics addressed here are quantum criticality and the physics of random field magnets. As second main emphasis here the first extensive study of the compound LiErF_4 is presented, ranging from the discovery of a quantum phase transition and determination of the phase diagram to an investigation of the dynamics.

Further studies on crystal fields in several LiReF_4 compounds will be presented as well as a first study of mixed compounds $\text{Li}(\text{HoEr})\text{F}_4$.

In the chapter ‘materials and methods’, the general properties of the compounds are listed, an introduction to the neutron scattering technic is given and the details of the experiments and sample preparation are remarked.

In the chapter ‘theoretical aspects’, model systems are discussed, the Hamiltonian of the LiReF_4 is derived and meanfield/RPA calculations are explained.

The structure of the main part of this thesis is then divided according to the particular compounds and the associated effects. The results achieved during this thesis are discussed in comparison with previous studies refereed in literature. To end up with a consistent story certain concepts and further detailed review of research will be introduced in this context, when they are thematically required.

Chapter 2

Materials and Methods

2.1 The Compound LiReF₄

The lithium rare earth tetrafluorides LiReF₄ crystallize in a tetragonal scheelite structure with space group $I4_1/a$. The Re-ion, four per unit cell, occupy positions with point symmetry S_4 . In figure 2.1 the unit cell is depicted. Further crystallographic specifications and the lattice constants for various compounds are listed in the appendix A.

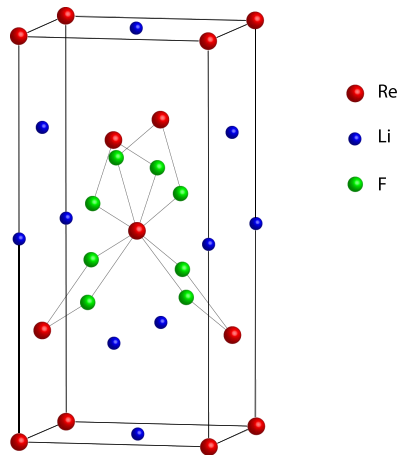


Figure 2.1: Unit cell of LiReF₄. To enhance visibility of the illustration the fluorine ions are only drawn around the $(a/2, a/2, c/2)$ Re position.

LiReF₄ is an ideal system to investigate an entire chemical series of compound, because it crystallizes for almost every element Re of the rare earth family without any significant structural change. The replacement only slightly affects the position of the fluorine ions and the lattice constants.

Another major advantage of the LiReF₄ family is the existence of an isostructural dilution series with non-magnetic Yttrium or Lutetium randomly substituted for the rare earth atoms, making available for experiments the full cross-over from isolated dipoles, through disordered interacting dipoles, to the pure limit. All compounds are optically transparent, electronically insulating, thermally stable and chemically inert under usual laboratory conditions. Further relevance with regard to intended magneto-optical experiments comes from the fact that LiYF₄ doped with up to a few percent magnetic Re-ions are widely used in laser technology [13].

2.2 Neutron scattering

2.2.1 Theory of Neutron Scattering

Neutron scattering is one of the most powerful methods to investigate a magnetic system, since in contrast to several other methods it provides direct information on static as well as dynamic properties of matter. Consider a monochromatic collimated neutron beam with flux Ψ_0 hitting a target, then the scattering intensity I detected in a angular sector $\Delta\Omega$ and an energy interval $\Delta E'$ is expressed via the scattering cross section:

$$I = \Psi_0 \frac{d^2\sigma}{d\Omega dE'} \Delta\Omega \Delta E'. \quad (2.2.1)$$

Since the interaction between neutron and target is weak, the transition probability from initial state λ to final state λ' of the systems, due to scattering of a neutron, can be derived from Fermi's Golden Rule. Incident and scattered neutrons will be described in the 1. Born Approximation as plane waves with wave vectors \mathbf{k} and \mathbf{k}' , respectively. The scattering process is characterized by the energy gain/loss $\hbar\omega = E - E'$ and the scattering vector $\mathbf{Q} = \mathbf{k} - \mathbf{k}'$. The general expression for the differential scattering cross section follows from summation over all transitions $\lambda \rightarrow \lambda'$ under consideration of momentum and energy conservation.

$$\frac{d^2\sigma}{d\Omega dE'} = \frac{k'}{k} \left(\frac{m}{2\pi\hbar^2} \right)^2 \sum_{\lambda\lambda'} p_\lambda \left| \langle \mathbf{k}'\lambda' | \hat{U} | \mathbf{k}\lambda \rangle \right|^2 \delta(\hbar\omega + E_\lambda - E_{\lambda'}). \quad (2.2.2)$$

Here \hat{U} denotes the interaction potential, m the mass of the neutron and p_λ the occupation probability for the state λ .

In the case of pure nuclear scattering the interaction \hat{U} between a neutron at position \mathbf{r} and the nuclei at positions \mathbf{R}_j can be described approximatively by the so called Fermi pseudo potential.

$$\hat{U}(\mathbf{r}) = \frac{2\pi\hbar^2}{m} \sum_j b_j \delta(\mathbf{r} - \mathbf{R}_j). \quad (2.2.3)$$

The scattering length b_j varies from isotope to isotope and are dependent from the relative orientation of the neutron spin compare to nuclear spins, if there is a nuclear spin present at all. The master formula for nuclear scattering follows from (2.2.2) und (2.2.3) by writing the delta function in form of an integral and the operators in Heisenberg picture:

$$\frac{d^2\sigma}{d\Omega dE'} = \frac{k'}{k} \frac{1}{2\pi\hbar} \sum_{jj'} b_j b_{j'} \int \left\langle e^{-i\mathbf{Q}\mathbf{R}'_j(0)} e^{i\mathbf{Q}\mathbf{R}_j(t)} \right\rangle e^{-i\omega t} dt. \quad (2.2.4)$$

Here the $\langle . \rangle$ denotes the thermal expectation value. If there is no correlation neither considering the isotopic distribution nor the nuclear spin configuration between the positions j and j' , the product $b_j b_{j'}$ of the scattering lengths can be replaced by the average values $\bar{b}_j \bar{b}_{j'}$ in the case of $j \neq j'$ or \bar{b}_j^2 in the case of $j = j'$. The scattering cross section then separates in two parts: coherent scattering originating from $\bar{b}_j \bar{b}_{j'}$ and incoherent scattering originating from $\bar{b}_j^2 - \bar{b}_j \bar{b}_{j'}$ respectively. In the elastic case the incoherent part only contributes to the background. The coherent elastic part can be rewritten by doing an explicit fourier transformation.

$$\left(\frac{d\sigma}{d\Omega} \right)_{coh, el} = N_0 \frac{(2\pi)^3}{v_0} \sum_{\boldsymbol{\tau}} |F_{\boldsymbol{\tau}}|^2 \delta(\mathbf{Q} - \boldsymbol{\tau}). \quad (2.2.5)$$

Here v_0 denotes the volume of the unit cell, N_0 the number of unit cells and the sum in $\boldsymbol{\tau}$ is running over the whole reciprocal lattice. The δ -function explicitly highlights the quasimomentum conservation, whereas the nuclear structure factor

$$F_{\boldsymbol{\tau}} = \sum_d b_d e^{i\boldsymbol{\tau} \cdot \mathbf{d}}. \quad (2.2.6)$$

is a reference of the order inside the unit cell. The Laue condition $\mathbf{Q} = \boldsymbol{\tau}$ is noting else as another form of Bragg's law, which connects the scattering angle 2ϑ and the wavelength with the distance d_{hkl} between crystallographic planes.

$$\lambda = 2d \sin \vartheta, \quad d_{hkl} = \frac{2\pi}{|\boldsymbol{\tau}_{hkl}|}. \quad (2.2.7)$$

Since the neutron incorporates a spin, it is able to interact also with the magnetic moments in a solid and can therefore be regarded as an ideal

microscopic magnetic probe. The interaction potential is given as

$$\hat{U} = -\boldsymbol{\mu}\mathbf{H} = -\boldsymbol{\mu} \left[\text{rot} \left(\frac{\boldsymbol{\mu}_e \times \mathbf{R}}{|\mathbf{R}|^3} \right) - \frac{e}{m_e c} \frac{\mathbf{p}_e \times \mathbf{R}}{|\mathbf{R}|^3} \right], \quad (2.2.8)$$

where the magnetic moment of the neutron is $\boldsymbol{\mu} = -\gamma\mu_N\boldsymbol{\sigma}$ with the gyro-magnetic factor $\gamma = 1.913$. The first term in (2.2.8) describes the spin-spin interaction with the intrinsic electronic moments $\boldsymbol{\mu}_e$ and the second with the orbital moments. Since the second term causes some difficulties the formalism will here be further developed for the spin term only. However, the orbital moments can be considered in the dipole approximation according to Johnston [14] by replacing subsequently the spin operators S^α in the resulting formulas with the total angular momentum $\frac{1}{2}g_L J^\alpha$. Starting with expression (2.2.2) and (2.2.8) finally the master formula for magnetic scattering is obtained.

$$\frac{d^2\sigma}{d\Omega d\omega} = (\gamma r_0)^2 \frac{k'}{k} F^2(\mathbf{Q}) e^{-2W(\mathbf{Q})} \sum_{\alpha\beta} \left(\delta_{\alpha\beta} - \frac{Q_\alpha Q_\beta}{Q^2} \right) S^{\alpha\beta}(\mathbf{Q}, \omega). \quad (2.2.9)$$

Here r_0 denotes the classic electron radius and the magnetic formfactor F describes the localized magnetic spin density. In the derivation of (2.2.9) magneto-elastic interference terms are neglected. Instead the fluctuations R_j are incorporated in form of the Debye-Waller factor $\exp(-2W(\mathbf{Q}))$. The magnetic scattering function is in fact nothing else than the fourier transformed time dependent spin-spin-paircorrelation function. According to the fluctuation-dissipation theorem this observable related to the imaginary part $\chi''(\mathbf{Q}, \omega)$ of the general susceptibility. This relation can be used also as the starting point to write down the inelastic cross-section, since from theoretical calculation often χ is obtained explicitly, as for example within linear response theory.

$$S^{\alpha\beta}(\mathbf{Q}, \omega) = \sum_{jj'} e^{i\mathbf{Q}(\mathbf{R}_j - \mathbf{R}_{j'})} \sum_{\lambda\lambda'} p_\lambda \langle \lambda | S_j^\alpha | \lambda' \rangle \langle \lambda' | S_{j'}^\beta | \lambda \rangle \delta(\hbar\omega + E_\lambda - E_{\lambda'}). \quad (2.2.10)$$

$$S(\mathbf{Q}, \omega) = \frac{1}{\pi} \frac{1}{1 - e^{-\beta\hbar\omega}} \chi''(\mathbf{Q}, \omega). \quad (2.2.11)$$

The cross section investigated in a neutron diffraction experiment is usually dominated by the elastic or quasielastic processes and can be related to the instantaneous structure factor $S(\mathbf{Q})$ obtained from (2.2.10) integrated over ω .

$$S^{\alpha\beta}(\mathbf{Q}) = \frac{1}{2\pi} \int_{-\infty}^{\infty} d\omega S^{\alpha\beta}(\mathbf{Q}, \omega) = \sum_{jj'} e^{i\mathbf{Q}(\mathbf{R}_j - \mathbf{R}_{j'})} \langle S_j^\alpha S_{j'}^\beta \rangle \quad (2.2.12)$$

$$= \sum_{jj'} e^{i\mathbf{Q}(\mathbf{R}_j - \mathbf{R}_{j'})} \langle S_j^\alpha \rangle \langle S_{j'}^\beta \rangle + \sum_{jj'} e^{i\mathbf{Q}(\mathbf{R}_j - \mathbf{R}_{j'})} C^{\alpha\beta}(j, j'). \quad (2.2.13)$$

Here $C^{\alpha\beta}(j, j') = \langle (S_j^\alpha - \langle S_j^\alpha \rangle)(S_{j'}^\beta - \langle S_{j'}^\beta \rangle) \rangle$ denotes the spin correlations of the system and its fourier transformed is the \mathbf{Q} -dependent susceptibility $\chi^{\alpha\beta}(\mathbf{Q})$. The first term in $S(\mathbf{Q})$ describes Bragg scattering, the second the diffuse scattering contribution, originating for example from finite size clusters or critical scattering close to a phase transition. Furthermore, the correlation length ξ of the system is proportional to the inverse width of the intensity distribution in reciprocal space.

The cross section for elastic scattering on long range ordered magnetic structures can be written in the most general form as follow.

$$\begin{aligned} \left(\frac{d\sigma}{d\Omega} \right)_{mag, el} &= N \left(\frac{1}{2} g \gamma r_0 \right)^2 F^2(\mathbf{Q}) \sum_{\alpha\beta} (\delta_{\alpha\beta} - q_\alpha q_\beta) \\ &\times \sum_{lrs} \exp(i\mathbf{q}(\mathbf{l} + \mathbf{d}_s - \mathbf{d}_r)) \langle J_{0r}^\alpha \rangle \langle J_{ls}^\beta \rangle. \end{aligned} \quad (2.2.14)$$

Here the indices l denotes the unit cells of the lattice and s , respectively r , the ions within the cell. In a static structure associated with an ordering wave vector $\boldsymbol{\kappa}$, the moments of the particular ions are given by

$$\langle J_{ls}^\alpha \rangle = \frac{1}{2} (\langle J_s^\alpha \rangle e^{i\boldsymbol{\kappa}\mathbf{R}_{ls}} + \langle J_s^\alpha \rangle^* e^{-i\boldsymbol{\kappa}\mathbf{R}_{ls}}). \quad (2.2.15)$$

By substituting this expression in formula (2.2.14) and taking the lattice sum it becomes obvious that magnetic Bragg scattering occurs if $\mathbf{Q} = \boldsymbol{\tau} \pm \boldsymbol{\kappa}$ is satisfied, where $\boldsymbol{\tau}$ denotes a reciprocal lattice vector. Certainly the magnetic lattice can be different from the structural lattice. Furthermore in the non-Bravais case the scattering cross section is proportional to the absolute square of the magnetic structure factor, which reflects the orientation of the moments inside the unit cell.

$$F_\alpha(\boldsymbol{\tau}) = |\langle J^\alpha \rangle|^{-1} \sum_{s=1}^n \langle J_s^\alpha \rangle e^{-i\boldsymbol{\tau}\mathbf{d}_s}. \quad (2.2.16)$$

Inelastic neutron scattering is the method of choice in crystal field spectroscopy. In the approximation of systems with N noninteracting ions according to the master formula (2.2.9) the cross section for the transition between the crystal field states $\Gamma_n \rightarrow \Gamma_m$ can be written as follows:

$$\frac{d^2\sigma}{d\Omega d\omega} = N \left(\frac{g\gamma r_0}{2} \right)^2 \frac{k'}{k} F^2(\mathbf{Q}) e^{-2W(\mathbf{Q})} p_n |\langle \Gamma_m | \mathbf{J}_\perp | \Gamma_n \rangle|^2 \delta(E_n - E_m + \hbar\omega), \quad (2.2.17)$$

$$|\langle \Gamma_m | \mathbf{J}_\perp | \Gamma_n \rangle|^2 = \sum_{\alpha, \beta} \left(\delta_{\alpha\beta} - \frac{Q_\alpha Q_\beta}{Q^2} \right) \langle \Gamma_m | J^\alpha | \Gamma_n \rangle \langle \Gamma_m | J^\beta | \Gamma_n \rangle. \quad (2.2.18)$$

Here p_n denotes the occupation probability of the initial state and \mathbf{J}_\perp the projection of the momentum operator perpendicular to \mathbf{q} . For a powder sample the average over \mathbf{Q} can be performed and the final cross section only depends on three diagonal matrix elements.

$$\left. \frac{d^2\sigma}{d\Omega d\omega} \right|_p = N \left(\frac{g\gamma r_0}{2} \right)^2 \frac{k'}{k} F^2(\mathbf{Q}) e^{-2W} \sum_{n,\alpha} \frac{2p_n}{3} |\langle \Gamma_m | J^\alpha | \Gamma_n \rangle|^2 \delta(E_n - E_m + \hbar\omega). \quad (2.2.19)$$

In any real neutron scattering experiment there are always imperfections like a finite spectral width, beam divergence, mosaicity of samples, non ideal transmission of filters and collimators and many other factors. All this effects lead to finite resolution. The experimental measured intensity at a point (\mathbf{Q}, ω) is therefore the cross section folded by a resolution function R , which can be modeled in good approximation by a gaussian.

$$I(\mathbf{Q}_0, \omega_0) = \int d\omega d\mathbf{Q} R(\mathbf{Q} - \mathbf{Q}_0, \omega - \omega_0) \cdot \frac{d^2\sigma}{d\Omega d\omega}(\mathbf{Q}, \omega). \quad (2.2.20)$$

2.2.2 Neutron Scattering Techniques

In the here presented work the following neutron scattering technics have been used.

Three Axis Spectroscopy As the name suggests the three axis spectrometer (TAS) contains three essential blocks: Monochromator, Sample, and Analyzer. A schematic outline for a typical instrument is shown in figure 2.2. According to the required energy range of interest the existing spectrometers subdivide essentially in two categories either cold $E_i \approx 2 - 15$ meV or thermal $E_i \approx 15 - 100$ meV. From the white incident neutron beam in the crystal monochromator a wavevector \mathbf{k}_i is selected by bragg reflection. The monochromatic beam is focused or collimated on the sample and the crystal analyzer selects from

the scattered neutrons again by Bragg reflection a particular wavevector \mathbf{k}_f . Finally, the neutrons are counted in the detector. Since the neutron source fluctuates, the number of counts is measured usually not per time but instead is referred to the incident flux recorded by the monitor. Collimators, diaphragms, and filters (often Beryllium or Graphite) can be installed at several positions of the scattering path to shape the beam, tailor the spectral and angular spread and optimize signal to noise ratio. The choice of a particular $\mathbf{k}_i, \mathbf{k}_f$ corresponds to certain position and orientation of the three components monochromator, sample and analyzer, represented by six angles labeled as A1 to A6. The advantage of the three axis method is selectivity in (\mathbf{Q}, ω) .

$$\mathbf{k}_i - \mathbf{k}_f = \mathbf{Q}. \quad (2.2.21)$$

$$\frac{\hbar^2 k_i^2}{2m_n} - \frac{\hbar^2 k_f^2}{2m_n} = \hbar\omega. \quad (2.2.22)$$

Since these relations contain only three constraints but \mathbf{k}_i and \mathbf{k}_f represent four degree of freedoms in the scattering plane there are several instrumental configuration associated to the same (\mathbf{Q}, ω) . In the experiment a particular choice is made that optimizes the resolution and intensity requirements. Two configurations are standard, either fixed \mathbf{k}_i or fixed \mathbf{k}_f . The overall merit of the TAS is its high versatility and the possibility the extend the setup for example towards polarized neutron scattering or neutron spin echo techniques and advanced sample environments including large pressure, high magnetic fields and low temperature.

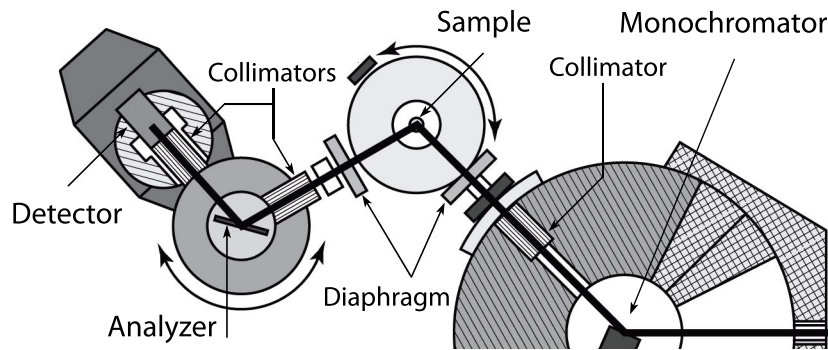


Figure 2.2: Schematic outline of a three axis instrument. (Reproduced from [15]).

Time of Flight Spectroscopy In the time of flight method the neutron beam is chopped in pulses and the incident energy is selected by passing several consecutive choppers sometimes in combination with a single crystal monochromator. Measuring the arrival time of the pulses at the detector at certain scattering angles provides the energy gain or loss and momentum transfer due to the scattering process. Compare to the TAS solution the TOF is not selective, a particular set $\hbar\omega$ and \mathbf{Q} cannot be chosen independently. On the other hand the advantage is a fast and parallel data collection, since the spectra of an entire reciprocal space submanifold is recorded simultaneously by the multidetector array.

Neutron Diffraction Most of the here presented neutron scattering experiments have been performed on so called two axis instrument designed for the purpose of single crystal diffraction. The outline of the instrument is similar to the three axis instrument, except that the third axis (the analyzer) is omitted and therefore all the neutrons which are scattered under a selected angle 2θ are collected in the detector. Nevertheless sometimes when signal to noise matters, the TAS is the instrument of choice to measure weak elastic signals, because the energy analyzer strongly reduces the background as compared to a diffractometer.

SANS Small Angle Neutron Scattering is a neutron diffraction technic to explore objects at nm scale and covers the range $Q = 10^{-6} \text{ nm}^{-1}$ up to 10^{-3} nm^{-1} . The white beam from the neutron source first passes a pure mechanical velocity selector acting as a monochromator and an adjustable collimator that controls the divergence of the beam. Neutrons scattered by the sample then enter an air evacuated flight tube, they spread out according to the transferred momentum Q while passing a flight path of typically 3 – 50 m and are collected finally by the position sensitive area detector. Before the sample the beam has to be cut down laterally by means of several masks, typical cadmium, tailored to fit the sample size. The reason is twofold, on one hand obviously to reduce the background originating from scattering from the sample environment, on the other hand to prevent reflections from the edges and side surfaces of the sample which are very intense and could lead to a severe damage of the detector.

2.3 Complementary Methods

Macroscopic methods measuring bulk properties like magnetization, susceptibility and specific heat are widely used in fundamental condensed matter research on magnetic systems as well as in applied physics. Since this laboratory based techniques are available fast and require only small samples, a first material characterization precedes almost every of the costly synchrotron or neutron scattering investigations. Although these techniques provide microscopic insight but the information obtained by elaborated macroscopic measurements are complementary and therefore inevitable to achieve a comprehensive understanding. Furthermore, bulk methods in conjunction with a tailored sample environment and using high quality samples are for example very convenient for high accuracy determination of phase transitions and critical exponents, whereas neutron scattering is often practically limited due to statistics and resolution.

Two techniques gained importance to study LiReF_4 : ac-susceptibility and specific heat. The heat capacity is defined as the amount of heat δQ transferred to the system per infinitesimal change in temperature dT . At low temperatures the relaxation method is used. There a heat pulse is applied to the sample for certain time period and while the system relax back to equilibrium the temperature is recorded as a function of time. From the measured relaxation c_p can be determined. The technical details of the experimental setup and data evaluation procedure used in case of the here presented c_p measurement in LiErF_4 are described in [16, 17]. The appeal of specific heat, in particular with regard to phase transitions, is its direct relation to the entropy. AC-Susceptibility measures the frequency dependent magnetic response of a system to an external excitation in form of an ac-field. This can be at any DC field including zero field. Since susceptibility is a complex quantity two quantities are measured, first the magnitude and second the phase shift between the measured and the drive signal. Technically the susceptometer is usually designed in a gradiometer setup. The outermost coil, the so called primary coil, is generating an excitation field. In the two secondary coils then a current is induced. The two secondary coils are designed and connected in such a way that their total signal is exactly canceled out when no sample is present. Since the filling factor, the fraction of the volume of the secondary coil which is filled by the sample is different for the two coils, the induced currents are also different. The net signal then corresponds to the flux generated by the sample only. The strength of the signal and the phase shift relative to the excitation can be detected by means of a lock-in amplifier. AC-susceptibility is particularly suitable to investigate spin glasses like compounds, recording the frequency dependence of susceptibility allows to probe the relaxation dynamics of the system.

2.4 Generic Models for Excitations, Correlation and Relaxation

Since often an applicable theoretical prediction of spectra and line shapes is missing to calculate the cross section, neutron scattering data can be evaluated instead by using generic model functions, which guarantee at least the minimal formal requirements as for example complexity and causality.

Excitations and Line Shapes The generalized susceptibility appearing in the cross section for neutron scattering can be related to the retarded Green's function of the system via a proportionality factor $\chi''(\mathbf{q}, \omega) = Z_q \cdot G''(\mathbf{q}, \omega)$. In the limit of sharp excitations ω_q with infinite lifetime one obtains

$$G_0(\mathbf{q}, \omega) = \lim_{\epsilon \rightarrow 0^+} \left[\frac{1}{\omega - \omega_q + i\epsilon} - \frac{1}{\omega + \omega_q + i\epsilon} \right]. \quad (2.4.1)$$

$$G''_0(\mathbf{q}, \omega) = \lim_{\epsilon \rightarrow 0^+} \pi [\delta(\omega + \omega_q) - \delta(\omega - \omega_q)]. \quad (2.4.2)$$

The Dyson Equations state that the general Green's function can be written in the following form introducing the self energy $\Sigma(\mathbf{q}, \omega) = \Delta_q(\omega) + i\Gamma_q(\omega)$.

$$G(\mathbf{q}, \omega) = \frac{G_0(\mathbf{q}, \omega)}{1 - G_0(\mathbf{q}, \omega)\Sigma(\mathbf{q}, \omega)}. \quad (2.4.3)$$

The selfenergy term can be derived for example by means of diagrammatic methods. The real part leads to a shift in the excitation energy, whereas the imaginary part introduces a damping and is directly related to the inverse of the finite excitation lifetime. Starting from this formula several line shape models can be derived by making assumptions on particular parametrizations for Σ . One example is the damped harmonic oscillator model DHO.

$$G''(\mathbf{q}, \omega) = \frac{4\omega_q\omega\Gamma_q}{(\omega^2 - \Omega^2)^2 - 4\omega^2\Gamma_q^2} \quad \Omega_q^2 = \omega_q^2 + 2\omega_q\Delta_q. \quad (2.4.4)$$

As a shortfall generic models such as the DHO can produce unphysical behavior in a certain regime, because they are based obviously on more or less crude approximations. However, there is another simple formula to construct useful generic model functions that are at least fully consistent with Kramers Kronig relation and causality.

$$\chi(\omega) = \frac{\chi(0)}{2} \left(\frac{A_1}{B_1 - \omega} + \frac{A_2}{B_2 - \omega} \right). \quad (2.4.5)$$

The restrictions on the poles to fulfill causality are $\Im B_i < 0$. For the two in this work considered models the parameters A and B are given as follows.

$$\text{Lorentzian: } B_i = \pm \omega_q - i\gamma \quad A_i = \pm \frac{\omega_q^2 + \gamma^2}{\omega_0}. \quad (2.4.6)$$

$$\text{DHO: } B_i = \pm \sqrt{\omega_q^2 - \frac{\gamma^2}{4}} - i\frac{\gamma}{2} \quad A_i = \pm \frac{\omega_q^2}{\sqrt{\omega_q^2 - \frac{\gamma^2}{4}}}. \quad (2.4.7)$$

Correlations In real space correlations can be approximatively described by means of an exponential model with one parameter ξ , the correlation length.

$$C(i, j) = f(\mathbf{r}_i - \mathbf{r}_j) e^{-|\mathbf{r}_i - \mathbf{r}_j|/\xi}. \quad (2.4.8)$$

With the prefactor $f(r) = 1$ one obtains in reciprocal space by Fourier transform a Lorentzian function for $\chi(\mathbf{q})$, in analogy to Ornstein Zernike theory.

$$\chi(\mathbf{q}) \sim \frac{1}{1 + \xi^2 q^2}. \quad (2.4.9)$$

Relaxations Describing AC-susceptibility spectra theoretically by an analytical model based on first principles is often impossible, because this problem involves the long range and low energy dynamic of the system. Therefore, experimental results are often discussed within phenomenological models. In the Debye model an exponential relaxation is assumed, where the response of the system is associated to a single relaxation time τ . By means of fourier transformation the following formula for frequency dependent complex susceptibility is obtained.

$$\chi(\omega) = \frac{\chi_0}{1 - i\omega\tau}. \quad (2.4.10)$$

A glassy system is not characterized by a single relaxation time only but instead there is a distribution $\rho(E)$ of different energy barriers, hence

$$\chi(\omega) = \chi_0 \int_0^\infty dE \frac{\rho(E)}{1 - i\omega\tau(E)}. \quad (2.4.11)$$

A common feature is that the energy dependence of the relaxation times $\tau(E)$ fulfills the Arrhenius law.

$$\tau(E) = \tau_0 e^{E/k_B T}. \quad (2.4.12)$$

The measured $\chi(\omega)$ allows then to draw conclusions about the underlying $\rho(E)$ of the system. For example in the compound $\text{LiHo}_x\text{Y}_{1-x}\text{F}_4$, $x = 0.167$ it turned out that the barriers are gaussian distributed, i.e. the relaxation times log-normal [18].

2.5 Sample Setup and Experimental Remarks

Samples Since LiReF_4 , also called as Re:YLF, is widely used in Laser technology, growth of single crystal in excellent qualities is well established and therefore large sample well adapted for neutron scattering have been available either from the laboratories of academic collaborators, namely K. W. Kraemer of the University Bern, or commercial suppliers. To reduce the neutron absorption, all compounds were synthesized from isotopic pure lithium ^7Li . For purpose of crystal field time of flight spectroscopy and powder diffraction powder samples are measured in standardized aluminum or at low temperatures in copper sample containers. To thermalize the sample the container was filled with He gas under 1 – 5 bar pressure. Nevertheless most of the neutron experiments have been performed on single crystals mounted on a sample holder from oxygen free copper. To guarantee a sufficient thermalization of the nonconducting samples at temperatures below 1 K a particular effort was accomplished. Often the simple mechanical contact to a clean copper surface was not sufficient to have enough thermal conductivity. One working solution was to put the whole sample in a container filled with He exchange gas. However in the case of the huge single crystals with dimensions in order of $1 \times 1 \times 3 \text{ cm}^3$ thermalizing the crystal as a whole by cooling its surface would never be possible due the vanishing thermal conductivity of LiReF_4 at low temperatures. The only practical solution was to cut the crystal in slices of 1 – 2 mm and reassemble them into a multi-sample, i.e. making a stack alternating the crystal with thin copper foil that ensure the thermal contact. In the most sophisticated version a thin gold film of a few μm thickness was sputtered directly on the crystal slices. The orientation of the samples was usually performed by means of X-Ray Laue diffraction and on the single crystal neutron diffractometer MORPHEUS at the Swiss Spallation Neutron Source (SINQ) at Paul Scherrer Institut (PSI). An accuracy of the alignment preferably within less than one degree was crucial in all experiments in which a

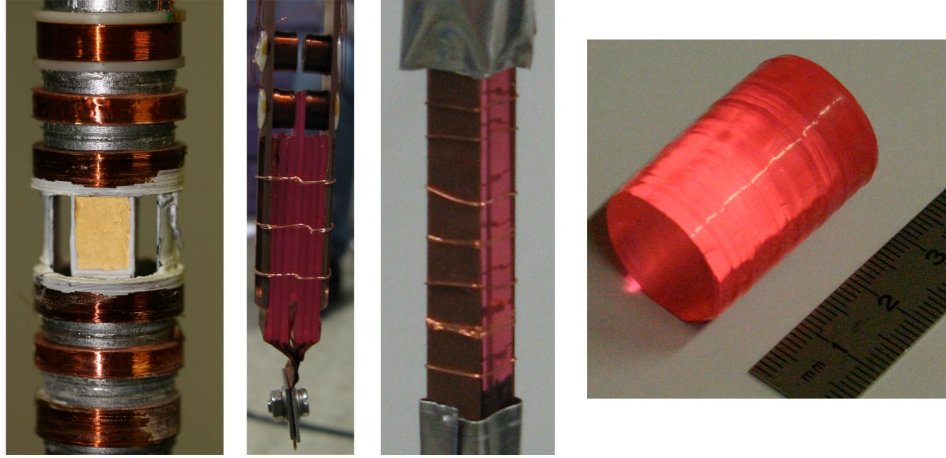


Figure 2.3: Selection of investigated samples. From left to right: $\text{LiHo}_{0.045}\text{Y}_{0.955}\text{F}_4$ together with insitu-susceptibility-SANS setup, $\text{Li}(\text{Ho,Er})\text{F}_4$ and insitu-susceptibility-diffraction setup, LiErF_4 measured by means of inelastic neutron spectroscopy, LiErF_4 ingot.

magnetic field has to be applied along a predefined crystal axis. Already a small miss-orientation would cause a systematic error and may change the physics completely as for example in the transverse field Ising model.

Sample Environment The neutron experiments performed in LiReF_4 requires low temperatures below 1 K and decent magnetic fields in the range of 1–6 Tesla. As typical sample environment a dilution refrigerator together with cryo-magnet was used providing temperatures down to $T \approx 50$ mK. The common magnet field direction is perpendicular to the scattering plane, however in the case of the planar antiferromagnet LiErF_4 for a few experiments a horizontal magnet was used instead.

Single Crystal Diffraction The single diffraction experiments have been performed on the instruments E4 at Helmholtz-Zentrum Berlin (HZB), D23 at Institut Laue-Langevin (ILL) in Grenoble, MORPHEUS, RITAI and TRICS on SINQ PSI. In these investigations mainly the field and temperature dependence of the magnetic signal, Bragg reflections as well as broad diffuse scattering, were mapped out by means of either field or temperature scans. One possibility are stepwise scans, at each field/temperature point a whole rocking curve or another reciprocal space scan is performed. This way is rather time consuming but allows to determine integrated intensities, provides the whole information about changes in the distribution of magnetic signal over the reciprocal space and allows to separate the different contributions for

Bragg and diffuse scattering. The other possibility is to count at fixed points in reciprocal space and ramping the field or temperature. This has the advantage of fast data collection and since the instrument has not to move, systematic errors arising from positioning inaccuracies are circumvented. But on the other hand from an experimental point of view any disturbance in positioning and orientation of the sample that may occur during the scan is not under control.

Three Axis Spectroscopy The inelastic neutron scattering investigations have been performed on the cold three-axis instruments TASP at SINQ PSI, PANDA at Forschungsneutronenquelle Heinz Maier-Leibnitz (FRMII) in Munich, 4F-2 at Laboratoire Léon Brillouin in Saclay and V2 at HZB Berlin. As instrumental configuration (double) focusing mode and no collimators have been used. A Beryllium filter mounted in front of the analyzer removed contributions from higher harmonics. The investigation of the spectra was carried out by means of energy scans in fixed k_f mode. Because the typical energy scale in LiReF_4 is far below 1 meV the achievable instrumental resolution on a three axis is the main limiting factor for the inelastic experiments, it was only in particular cases possible to resolve and distinguish discrete modes in the spectra. This required to measure at unusual low $k_f \leq 1.2 \text{ \AA}$. The corresponding drop in intensity could only be afforded by the fact that rare earth ions provide a strong scattering signal due to their large moments. For example on TASP a resolution of $95 \mu\text{eV}$ of the elastic line was obtained at fixed $k_f = 1.2 \text{ \AA}$ and on PANDA at $k_f = 1.079 \text{ \AA}$ a resolution of $37 \mu\text{eV}$ respectively. It has to be mentioned that a low k_f also reduces the accessible range in Q-space. In LiHoYF_4 it was for example desirable to be able to reach $Q = (200)$. For this purpose on V2 $k_f = 1.25 \text{ \AA}$ was the best compromise. But it turned out that the required resolution could be regained even at this relative large k_f by reducing the horizontal opening of the mask just before the detector to 1 cm approximatively. The resulting resolution of the elastic line was $74 \mu\text{eV}$.

Time-of-Flight Spectroscopy The time-of-flight method was used for the purpose of crystal-field spectroscopy. The experiments have been performed at the cold-neutron instruments FOCUS at SINQ PSI, TOFTOF at FRMII in Munich and the thermal-neutron instrument LRMCS at the Intense Pulsed Neutron Source (IPNS) at Argonne National Laboratory. To be able to separate the spectral lines from each other, a good energy resolution was crucial. But on the other hand a large accessible energy window was necessary too, which required a sufficient large incident energy E_i . The optimal instrumental configuration was a compromise of the two requirements. On FOCUS the unique op-

portunity was used to measure on the higher order reflections of the monochromator, i.e. PG400 instead of PG200. In the case of the copper-spectrometer TOFTOF the disks-copper windows could be reduced to half-width opening. Due to the large rare earth moments, the scattering intensity was not a limiting factor. Therefore, one could gain around a factor of two in resolution using these non-standard monochromator settings on TOFTOF and FOCUS.

SANS with insitu Susceptibility As sample environment the unique 11 Tesla horizontal field cryomagnet was used at SANSI SINQ. The orientation of the field can be chosen either parallel or perpendicular to the beam. For magnetic scattering this results either in a symmetric or asymmetric scattering due to the polarization factor in the cross section. For the AC-pumping, we built a coil setup (figure 2.3) with 4 split excitation coils and 2 counter-wound pick-up coils. Since the experiment has to be performed in the subkelvin temperature range, the crucial point was to achieve high enough magnetic fields without inducing too much heating power to the sample. A further difficulty arose from the limited available space for the sample in a dilution cryostat. In our setup the coil system was thermally connected to the IVC and disconnected from the sample. The built insitu susceptometer was able to achieve high enough excitation fields as well as a high sensitivity without any disturbance in the cooling performance of the dilution cryostat. Since these measurements were not at all standard in terms of sample environment, preparation and building up the setup was the most demanding and time-consuming part of the whole experiment.

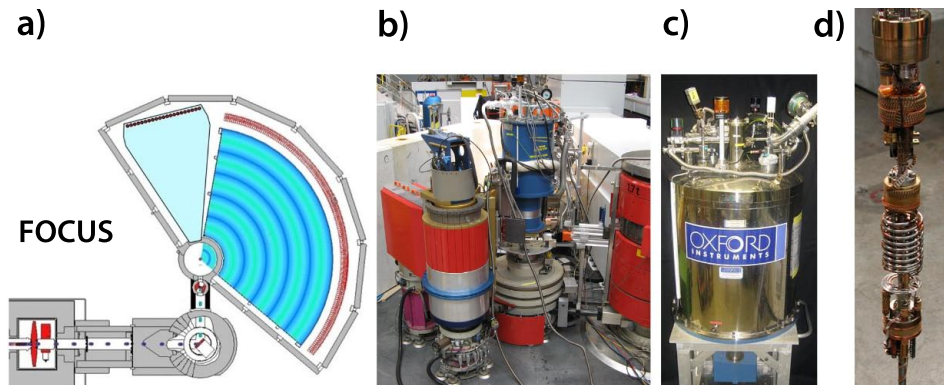


Figure 2.4: Neutron instruments and sample environment: a) Schematic view of TOF-spectrometer FOCUS at SINQ, b) TASP at SINQ, c) 11 Tesla magnet MA11 at SINQ, d) Dilution cryostat.

Chapter 3

Aspects of Theory

3.1 Hamiltonian

For the magnetic properties in rare earth compounds the 4f electrons play a crucial role. In contrast to the 6s and 5d electrons, which contribute to the conduction band in form of delocalized Bloch states, the 4f electrons maintain their character as localized moments. According to the Russell-Saunders scheme the particular spins s_i and angular momenta l_j combines to a total spin S and total orbital momentum L . This is a consequence of the dominance of exchange interaction and coulomb repulsion compared to spin orbit coupling. As a further perturbation spin-orbit coupling can then be included using the Wigner-Eckart Theorem.

$$\mathcal{H}_{SO} = \pm\zeta(LS) S \cdot L, \quad (3.1.1)$$

Here the coupling constant ζ is only dependent from L and S and the sign is given, either if the shell is more or less than half filled. The total angular momentum $J = L+S$ together with S and L are therefore the suitable quantum numbers to diagonalize this term. The ground state multiplet $^{2S+1}L_J$ is then given by Hund's rules. In contrast to transition metal compounds in the rare earth the effect of spin-orbit coupling is dominant compared to the crystal field splitting. Therefore the Hamiltonian relevant for the magnetic and low temperature thermodynamic properties can be written in the subspace of the ground state multiplet.

The complete Hamiltonian operator to describe the LiReF₄ system includes first a single ion part containing crystal fields, Zeeman term, hyperfine interaction and second a part covering the coupling between the spins. The different terms are discussed in the following.

$$\mathcal{H} = \sum_i [\mathcal{H}_{CF}(\mathbf{J}_i) + A\mathbf{J}_i \cdot \mathbf{I}_i - g\mu_B\mathbf{J}_i \cdot \mathbf{H}] - \frac{1}{2} \sum_{ij} \sum_{\alpha\beta} \mathcal{J}_D D_{\alpha\beta}(ij) J_{i\alpha} J_{j\beta} - \frac{1}{2} \sum_{ij, n.n.} \mathcal{J}_{12} \mathbf{J}_i \cdot \mathbf{J}_j. \quad (3.1.2)$$

The magnetic field is from an experimental point of view in the LiReF₄ system the main control parameter apart from temperature. Recall Wigner-Eckart theorem that the matrix elements of $\mathbf{L} + 2\mathbf{S}$ is proportional to the matrix elements of \mathbf{J} within the multiplet and the Zeeman term can be written as

$$\mathcal{H}_Z = -\mu_B g \mathbf{H} \cdot \mathbf{J}, \quad (3.1.3)$$

where

$$g = \frac{3}{2} + \frac{S(S+1) - L(L+1)}{2J(J+1)} \quad (3.1.4)$$

denotes the Lande factor.

The hyperfine interaction between the 4f moments and the nuclear spins

$$\mathcal{H}_{hf} = A \sum_i \mathbf{I}_i \cdot \mathbf{J}_i, \quad (3.1.5)$$

can often be neglected in rare earth magnetism, since the typical order of magnitude of A is in the range of a few μeV . Nevertheless in the considered case of LiHoYF₄ $A_{\text{Ho}} = 3.36 \mu\text{eV}$ this marginal coupling affects decisively critical behavior and dynamics around the quantum phase transition.

3.1.1 Crystal Field

Embedded in a crystal the Re-ion is affected by the electrical potential induced by the neighboring ions, the so called crystal field. This breaks the $J(J+1)$ degeneracy of $^{2S+1}L_J$ and the splitting is given by the symmetry of the particular site inside the crystal. The potential can be developed in form of a multipole expansion.

$$v_{cf}(r, \theta, \phi) = \sum_{lm} A_l^m r^l Y_{lm}(\theta, \phi). \quad (3.1.6)$$

The matrix elements of v_{cf} evaluated within the sub-Hilbertspace of a particular J are according to Stevens [19] proportional to the matrix elements of operator equivalents build up from products of the momentum operators. The crystal field Hamiltonian is now written in terms of these operator equivalents.

$$\mathcal{H}_{cf} = \sum_i \sum_{lm} A_l^m \alpha_l \langle r^l \rangle \left(\frac{2l+1}{4\pi} \right)^{1/2} \tilde{O}_{lm}(J_i). \quad (3.1.7)$$

Hereby the α_l denotes the Stevens factors and the Racah operators $\tilde{O}_{lm}(J_i)$ are the operators associated to the spherical harmonics. Instead of the Racah operators it is appropriate to use the so called Stevens operators $O_l^m(J)$, which are equivalent to the tesseral harmonics, the real linear combinations of the spherical harmonics.

$$\mathcal{H}_{cf} = \sum_i \sum_{lm} B_l^m O_l^m(J_i). \quad (3.1.8)$$

In the case of f electrons there are only multipoles up to the order $l = 6$ relevant and from the remaining crystal field parameters B_l^m all except seven are vanishing due to symmetry arguments. Not only crystal symmetry matters but also time reversal symmetry, because the nature of the crystal field is purely electronic. The remaining crystal field parameters can hardly be calculated from first principles in a sufficient accuracy and therefore usually an experimental determination is indicated.

In LiReF₄ the crystal field Hamiltonian is given explicitly as follows:

$$\mathcal{H} = \sum_{l=2,4,6} B_l^0 O_l^0 + \sum_{l=4,6} B_l^4(c) O_l^4(c) + B_l^0(s) O_6^4(s). \quad (3.1.9)$$

Hereby the x-axis was chosen by rotation of the coordinate system around the crystal symmetry axis z, such that the parameter $B_4^4(s)$ is zero. Otherwise the additional term $O_6^4(s)$ has to be considered. The Stevens operators (3.1.10) are written here according to the convention of Hutchings [20]. To make the formulas clearer the abbreviation $X \equiv J(J+1)$ is introduced.

$$\begin{aligned} O_2^0 &= 3J_z^2 - X \\ O_4^0 &= 35J_z^4 - (30X - 25)J_z^2 + 3X^2 - 6X \\ O_4^4 &= \frac{1}{2}(J_+^4 + J_-^4) \\ O_6^0 &= 231J_z^6 - (315X - 735)J_z^4 + (105X^2 - 525X + 294)J_z^2 \\ &\quad - 5X^3 + 40X^2 - 60X \\ O_6^4(c) &= \frac{1}{4}[(11J_z^2 - X - 38)(J_+^4 + J_-^4) + (J_+^4 + J_-^4)(11J_z^2 - X - 38)] \\ O_6^4(s) &= \frac{1}{4i}[(11J_z^2 - X - 38)(J_+^4 - J_-^4) + (J_+^4 - J_-^4)(11J_z^2 - X - 38)]. \end{aligned} \quad (3.1.10)$$

As it has been already mentioned, an accurate theoretical calculation of crystal field parameters is often difficult. However, as a first approximation a simple point charge model could provide an illustrative insight. Thereby at each crystal site R_j a charge q_j of the corresponding ion is placed and the potential at place of the Re-ions is calculated. The formula used for this calculation can be written as:

$$V_{pointcharge}(r, \theta, \phi) = \sum_{n=0}^{\infty} \sum_{\alpha=-n}^n r^n \gamma_{n\alpha} Z_{n\alpha}(\theta, \phi). \quad (3.1.11)$$

$$\gamma_{n\alpha} = \sum_{j=1}^k \frac{4\pi}{2n+1} q_j \frac{Z_{n\alpha}(\theta_j, \phi_j)}{R_j^{n+1}}. \quad (3.1.12)$$

In the formula (3.1.12) $Z_{n\alpha}$ denotes the tesseral harmonics and the $\gamma_{n\alpha}$ correspond up to a tabulated prefactor (see for example [20]) to the crystal field parameters B_n^α .

3.1.2 Magnetic Interactions

Responsible for magnetic ordering in LiReF_4 is first and foremost the long range and anisotropic dipole-dipole coupling between the Re-ions.

$$\mathcal{H}_{dipol} = -\frac{1}{2} \sum_{ij} \sum_{\alpha\beta} \mathcal{J}_D D_{\alpha\beta}(ij) J_{i\alpha} J_{j\beta}, \quad (3.1.13)$$

with the classical dipole tensor

$$D_{\alpha\beta}(ij) = \frac{3(r_{i\alpha} - r_{j\alpha})(r_{i\beta} - r_{j\beta}) - |\mathbf{r}_i - \mathbf{r}_j|^2 \delta_{\alpha\beta}}{N |\mathbf{r}_i - \mathbf{r}_j|^3}. \quad (3.1.14)$$

The dipole coupling parameter is given as $\mathcal{J}_D = (g\mu_B)^2 N$, where N is the number of ions per unit volume. Furthermore there should also be considered a nearest neighbor exchange coupling in form of an isotropic Heisenberg term.

$$\mathcal{H}_{ex} = -\frac{1}{2} \sum_{ij, n.n.} \mathcal{J}_{12} \mathbf{J}_i \cdot \mathbf{J}_j. \quad (3.1.15)$$

It can be experimentally verified that the exchange interaction is weak compare to the dipolar coupling in the case of LiReF_4 . Nevertheless \mathcal{J}_{12} is one of the few unknown parameters in the model and if not otherwise determined often used as a tuning parameter to match the calculated and measured phase diagram.

In the meanfield/RPA treatment of the system it was required to perform the fourier transformation of the coupling tensor $\bar{\mathcal{J}}$. Numerically the dipolar sum has been calculated with the method of Bowden and Clark [21] for $q \neq 0$ and with direct summation in the case of $q = 0$. Not to forget, in the limit of $\mathbf{q} = \mathbf{0}$ the long range nature of the dipolar interaction is crucial and leads to the additional so called Lorentz term. To derive this term the summation can be split up in two parts a discrete finite sum over the range of a sphere and a continuous integral incorporating the couplings outside this sphere up the sample margins.

$$\tilde{D}_{\alpha\beta}(\mathbf{0}) = \sum_j D_{\alpha\beta}(ij) = \sum_{j \in \text{sphere}} D_{\alpha\beta}(ij) + \frac{1}{V} \int_{\partial \text{sphere}}^{\partial \text{sample}} \frac{3r_\alpha r_\beta - \delta_{\alpha\beta} r^2}{r^5} d\mathbf{r}. \quad (3.1.16)$$

Here V denotes the volume per ion inside the crystal. The integral vanishes for $\alpha \neq \beta$. Explicitly, one can show that the diagonal elements of the integral term are equal to the Lorentz term $4\pi/3$ minus the demagnetization factor of the sample N_α .

3.2 Transverse Field Ising Model - RPA/MF

The transversal field Ising model (TFIM) describes a general system of particles sitting each in a double well shaped potential, a coupled together via J_{ij} and able to tunnel with a probability Γ between the two possible states. In order to generalize the discussion of the following meanfield treatment, the Hamilton operator considered contains, additional to the TFIM part, also a longitudinal random field term.

$$\mathcal{H} = -\frac{1}{2} \sum_{ij} J_{ij} \sigma_i^z \sigma_j^z - \Gamma \sum_i \sigma_i^x - \sum_i h_i \sigma_i^z. \quad (3.2.1)$$

Here σ^α stands for the Pauli matrices. The first simplification made is to replace the h_i by their averaged value $h = \bar{h}$. Write

$$\sigma_i^z \sigma_j^z = -\langle \sigma_i^z \rangle \langle \sigma_j^z \rangle + \sigma_i^z \langle \sigma_j^z \rangle + \langle \sigma_i^z \rangle \sigma_j^z + (\sigma_i^z - \langle \sigma_i^z \rangle)(\sigma_j^z - \langle \sigma_j^z \rangle), \quad (3.2.2)$$

where $\langle \sigma_j^z \rangle$ denotes the thermal expectation value. Neglecting the correlation term, i.e. the term quadratic in the fluctuations, and the constant that anyway drops out in the calculation of the partition sum, the many body Hamiltonian can be decoupled and reduced to a single ion problem.

$$\mathcal{H}_i = -h_i \sigma_i^z - \Gamma \sigma_i^x - \sigma_i^z \sum_j J_{ij} \langle \sigma_j^z \rangle. \quad (3.2.3)$$

$$\mathcal{H}_{MF} = \sum_j \mathcal{H}_j = - \sum_j \gamma_j \cdot \sigma_j. \quad (3.2.4)$$

Hereby it was further assumed that the expectation value $\langle \sigma_j^z \rangle$ is identical for all spins equal $\langle \sigma^z \rangle$. γ denotes an effective field and by the following definition there is obviously $\gamma \geq \Gamma$.

$$\gamma = (\Gamma, 0, J_0 \langle \sigma^z \rangle + \bar{h}) = \gamma(\sin \theta, 0, \cos \theta). \quad (3.2.5)$$

Here $J_0 = \sum_j J_{ij}$. Digitalizing (3.2.3) leads to the eigenvalues $\pm\gamma$ and the following thermal expectation value for of the spins.

$$\langle \sigma \rangle = (\sin \theta, 0, \cos \theta) \cdot \tanh(\beta\gamma). \quad (3.2.6)$$

To fulfill selfconsistency this expression must be in accordance to the relation in (3.2.5):

$$\langle \sigma^z \rangle = \frac{\gamma \cos \theta - \bar{h}}{J_0} = \cos \theta \tanh(\beta\gamma). \quad (3.2.7)$$

For the disordered phase, but only if $h = 0$ there is $\gamma = \Gamma$ because of $\langle \sigma \rangle = 0$. In all other cases the selfconsistency relation can written explicitly in the following form.

$$\sqrt{\gamma^2 - \Gamma^2} \cdot |\gamma - J_0 \tanh(\beta\gamma)| - |h|\gamma = 0. \quad (3.2.8)$$

Consider now the special case of $h = 0$. In the ferromagnetic phase the $\cos \theta \neq 0$ can be canceled out on both side of the equation and it follows

$$\gamma = J_0 \tanh(\beta\gamma). \quad (3.2.9)$$

The resulting expectation values for s^x , s^z and the phase diagram are shown in figure 3.1. Especially for $T = 0$ K there is $\tanh(\beta\gamma) = 1$ and the magnetization as a function of Γ can be written explicitly as

$$\langle \sigma^z \rangle = \sqrt{1 - \Gamma^2/J_0^2} \quad \text{for } h = 0, T = 0 \text{ K}, \Gamma \leq \Gamma_c. \quad (3.2.10)$$

The critical field value, where the quantum phase transition takes place, is $\Gamma_c = J_0$. Furthermore the critical temperature in zero field is $T_c = J_0 k_B^{-1}$ and the phase boundary as a function of temperature is given by the relation

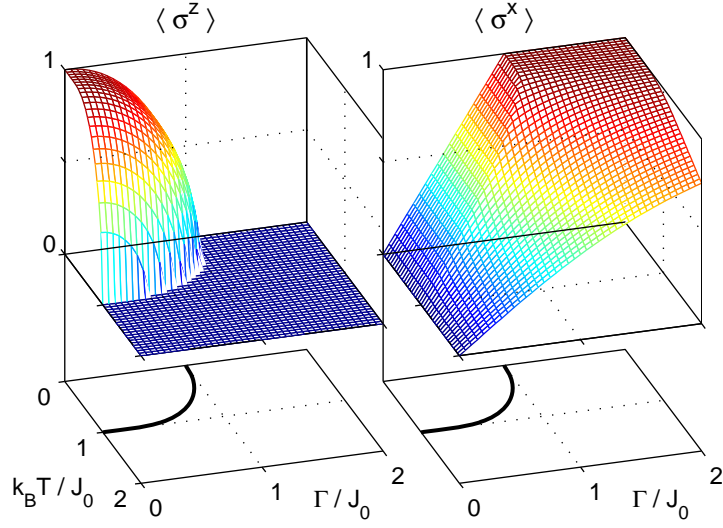


Figure 3.1: Meanfield expectation values of $\langle \sigma^z \rangle$, $\langle \sigma^x \rangle$ and phase diagram as a function of transversal field Γ and temperature.

$$\Gamma_c(T) = J_0 \tanh(\beta \Gamma_c(T)). \quad (3.2.11)$$

Considering the presence of longitudinal field $h \neq 0$, there is no sharp transition anymore but instead a cross-over, see figure 3.2. The magnetization decays continuously and the susceptibility χ^{zz} is rounded and vanishes with increasing field h . Furthermore the position of the peak in χ^{zz} is shifted towards higher Γ . Already this simple meanfield calculation highlights the fact that quantum criticality is not preserved under the presence of even small longitudinal (random) fields [10].

The simplest approach to discuss the dynamics of the system is a random phase approximation RPA. The generalized susceptibility in a generic system is given by the following RPA-selfconsistency relation [22]:

$$\bar{\bar{\chi}}(ij, \omega) = \bar{\bar{\chi}}_i^0(\omega) \left(\delta_{ij} + \sum_{j'} \bar{\bar{J}}(ij') \bar{\bar{\chi}}(j'j, \omega) \right). \quad (3.2.12)$$

Here the double bar denotes a tensorial quantities and $\bar{\bar{\chi}}^0$ the single ion susceptibility calculated within the meanfield states, $\bar{\bar{J}}(ij')$ the total interaction between the ions, dipolar as well as exchange coupling.

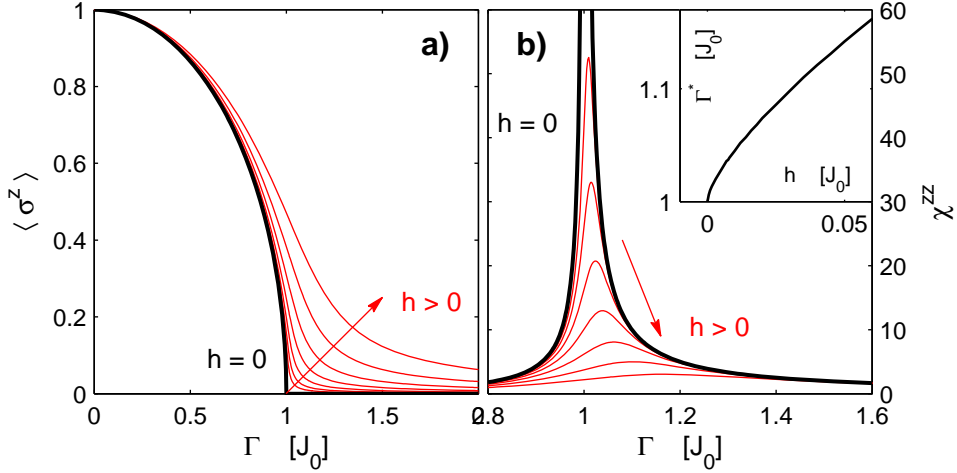


Figure 3.2: The meanfield calculated magnetization (a) and susceptibility χ^{zz} (a) of the TFIM in presence of a longitudinal field. Even a small perturbation h leads to a crossover instead of a sharp transition. The marginal field Γ^* for the crossover, defined as the point where χ^{zz} reach its maximum, increases with h (Inset).

$$\begin{aligned} \chi_i^{0,\alpha\beta}(\omega) &= \lim_{\varepsilon \rightarrow 0^+} \sum_{nm} \frac{\langle n | \sigma_i^\alpha | m \rangle \langle m | \sigma_i^\beta | n \rangle}{E_m - E_n - \omega - i\varepsilon} (n_n - n_m) \\ &= \lim_{\varepsilon \rightarrow 0^+} \frac{4\gamma \Re\{c_{\alpha\beta}\} + 2i(\omega + i\varepsilon)\Im\{c_{\alpha\beta}\}}{4\gamma^2 - (\omega + i\varepsilon)^2} \tanh\left(\frac{\gamma}{k_B T}\right). \end{aligned} \quad (3.2.13)$$

The population factors n_m respectively n_n are derived from the energy levels of the mean field Hamiltonian. To further simplify the notation the abbreviation $c_{\alpha\beta} = \langle 1 | \sigma^\alpha | 2 \rangle \langle 2 | \sigma^\beta | 1 \rangle$ was used, where $|1\rangle, |2\rangle$ denotes the two eigenstates of the single ion meanfield Hamiltonian. The infinitesimal parameter ε is introduced to guarantee the correct analyticity of the formulas with real ω . The physical meaning of this is that the perturbation of the system is switched on adiabatically. The sign of ε is chosen to reproduce the correct asymptotic behavior and fulfill causality. In the limit $\varepsilon \rightarrow 0$ a delta function results, meaning that in the framework of RPA the spectral lines are infinitely sharp. However in numerical calculations the parameter epsilon is often set to a sufficient small value to circumvent performing the limit explicitly.

The above set of formulas (3.2.12) can be further decoupled by means of Fourier transforms. In the here considered case of an Ising Model only one

component of the coupling tensor $\bar{J}(\mathbf{q})$ is nonzero, namely $\bar{J}^{zz}(\mathbf{q})$ further denoted as J_q . The final RPA equation is then given explicitly by the following expression.

$$\begin{aligned} \bar{\chi}^{\alpha\beta}(\omega, q) &= \left(id - \bar{\chi}_0 \bar{J}_q \right)^{-1} \bar{\chi}_0 \\ &= \begin{pmatrix} \chi_0^{xx} + \frac{J_q \chi_0^{xz} \chi_0^{zx}}{1 - J_q \chi_0^{zz}} & \chi_0^{xy} + \frac{J_q \chi_0^{xz} \chi_0^{zy}}{1 - J_q \chi_0^{zz}} & \frac{J_q \chi_0^{zz} \chi_0^{xz}}{1 - J_q \chi_0^{zz}} + \chi_0^{xz} \\ \chi_0^{yx} + \frac{J_q \chi_0^{yz} \chi_0^{zx}}{1 - J_q \chi_0^{zz}} & \chi_0^{yy} + \frac{J_q \chi_0^{yz} \chi_0^{zy}}{1 - J_q \chi_0^{zz}} & \frac{J_q \chi_0^{zz} \chi_0^{yz}}{1 - J_q \chi_0^{zz}} + \chi_0^{yz} \\ \frac{\chi_0^{zx}}{1 - J_q \chi_0^{zz}} & \frac{\chi_0^{zy}}{1 - J_q \chi_0^{zz}} & \frac{\chi_0^{zz}}{1 - J_q \chi_0^{zz}} \end{pmatrix}. \end{aligned} \quad (3.2.14)$$

If $J_q \chi_0^{zz} = 1$ there is a singularity in χ . This corresponds to a collective excitation of the system. Considering (3.2.13) and recalling from the meanfield calculation that $c_{zz} = \sin^2 \theta = \Gamma^2 / \gamma^2$ the dispersion relation results.

$$\omega_q^2 = 4\gamma^2 - 4J_q \Gamma^2 \frac{\tanh \beta\gamma}{\gamma}. \quad (3.2.15)$$

As an illustrative example the dispersion as a function of momentum q and transversal field in the simplest case of a Ising chain with nearest neighbor interaction is depicted in figure 3.3. There is a characteristic softmode in the spectra, the excitation corresponding to the ferromagnetic ordering vector $q = 0$ soften at the quantum critical point $\Gamma = \Gamma_c$.

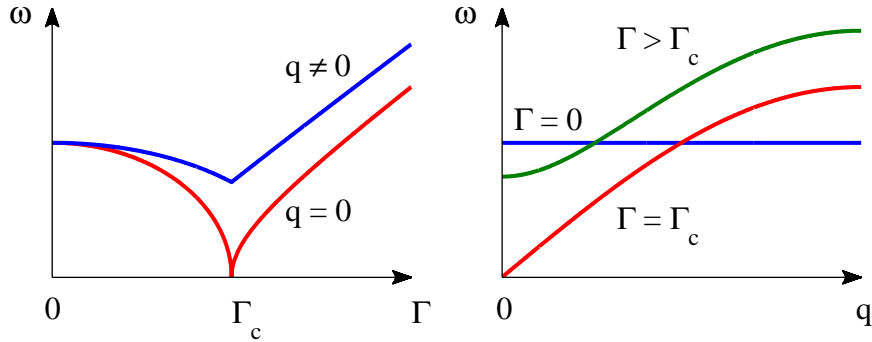


Figure 3.3: Schematic illustration of the RPA-dispersion relation for the TFIM. The characteristic excitations $\omega(q = 0)$ soften at the quantum critical point.

A perturbation in form of a longitudinal (random) field h leads to a gapped spectra instead of a soft mode at the quantum phase transition. The RPA formula derived above has not to be modified, only the inserted meanfield

parameter γ is affected by the additional longitudinal term. The excitation energy at zone center $q = 0$ as function of transversal field Γ for various strength of the perturbation h is shown in figure 3.4. Numerically it can be demonstrated that the gap follows in a good approximation a power law $\omega^* \sim h^\mu$ with $\mu \approx 0.36$.

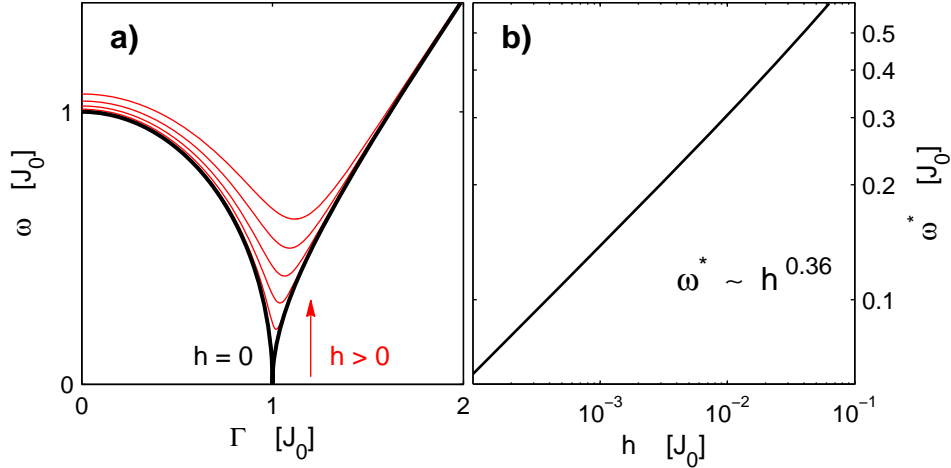


Figure 3.4: RPA calculations for the TFIM with longitudinal perturbation field h . (a) Excitation spectra $\omega(q = 0)$ as a function of the transversal field Γ . The true soft mode at the quantum critical point is revealed only in the limit of $h = 0$, whereas the dependence of the gap ω^* from perturbation h at the cross over point is described effectively by a power law (b).

The aim of the following section is to develop the meanfield/RPA formulas for the real LiReF_4 system. Nevertheless an assignment of LiHoF_4 to the effective TFIM is an efficient break down in complexity and leads to a reasonable and illustrative approximation to reproduce for example the phase diagram [9, 23]. In this mapping, the parameter Γ is essentially proportional to half of the splitting between the two lowest energy levels. Of course there is also a slightly field dependent renormalization of the absolute value of the moments. The energy splitting induced by the Zeeman term is linear to the real magnetic field H_t only in the limit of large fields, because of $g_\perp = 0$ for the ground state doublet. For small fields the lowest non-vanishing term in perturbation theory is of second order, hence $\Gamma \propto H_t^2$.

3.3 LiReF_4 System RPA/MF

In LiReF_4 the unit cell contains four magnetic ions with equivalent crystal field environments. In the ferromagnetic case, for example LiHoF_4 , each site

can be considered equivalently and the effective coupling between them is given by

$$\tilde{\mathcal{J}}(\mathbf{0}) = \overline{\mathcal{J}_D \tilde{D}_{cc}}(\mathbf{0}) + 4\mathcal{J}_{12}. \quad (3.3.1)$$

Here, $\tilde{\mathcal{J}}$ and \tilde{D} denotes the Fourier transformed quantities. In the particular example of LiHoF₄ an exchange coupling constant of $\mathcal{J}_{12} = -0.1 \mu\text{eV}$ is reported [24] and the dipolar contribution $\tilde{D}_{\alpha\alpha}(\mathbf{0})$ equals to

$$\begin{aligned} \mathcal{J}_D \tilde{D}_{aa}(\mathbf{0}) &= (\mu_B g)^2 N \left(\frac{4\pi}{3} - 0.83225 \right) = 3.912 \mu\text{eV} \\ \mathcal{J}_D \tilde{D}_{cc}(\mathbf{0}) &= (\mu_B g)^2 N \left(\frac{4\pi}{3} + 1.66451 \right) = 6.821 \mu\text{eV}, \end{aligned} \quad (3.3.2)$$

where the first term originates from numerical lattice sum whereas the second term $\frac{4\pi}{3}$ represents the Lorentzfactor. The number of Re-ions per unit volume is $N = 1.389 \cdot 10^{22} \text{ cm}^{-3}$.

The cases where it is required to incorporate also the hyperfine interactions involve a diagonalization of the MF-Hamiltonian in the full $(2J+1) \cdot (2I+1)$ dimensional subspace instead of $(2J+1)$. However in some compounds like for example LiErF₄ this leads to a marginal influence on the final result and counts anyway only in the temperature region which is hardly accessible by experiments. This is contrary to LiHoF₄, where the effect not can be neglected. The meanfield phase diagram obtained in calculations with and without considering hyperfine coupling are shown in figure 3.5.

In the meanfield calculation for an antiferromagnet for each sublattices ι an expectation value $\langle \mathbf{S}_\iota \rangle$ has to be assigned. The generic choice was four sublattices, one for each ion in the unit cell. This approach enabled to predict the experimentally confirmed magnetic structure. An attempt to improve the approximation was to perform a meanfield calculation based on clusters of spins rather than separate ions and treat the cluster itself by means of exact diagonalization. However from a practical point of view this was only possible for sizes up to a few spins and lead only to neglectable changes in the calculated H_c and T_c .

For multi composite systems like LiRe^ARe^BF₄ where A and B stand for different rare earth ions the virtual crystal approximation (VCA) can be used to formulate a simple meanfield approach. The momentum operators at site j can be written as

$$\mathbf{J}_j^{VC} = n_j \mathbf{J}_j^A \oplus (1 - n_j) \mathbf{J}_j^B, \quad (3.3.3)$$

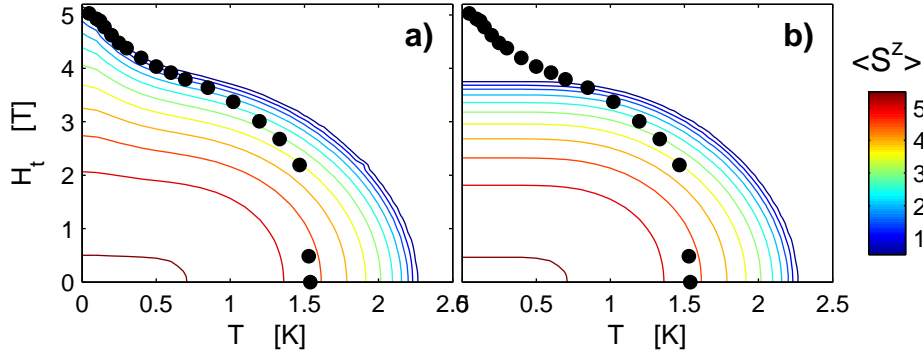


Figure 3.5: Contour plot of the mean field expectation values S^z and phase diagram as function of temperature and transversal field for the compound LiHoF_4 . The points are the experimentally determined values according to [9]. The meanfield calculation is shown for the case in which hyperfine interaction is considered (a) or neglected (b). The calculated T_c and H_c is sensitive to the assumed exchange coupling \mathcal{J}_{12} . Here the in the literature generally accepted value form [24] was used, although a larger (antiferromagnetic) \mathcal{J}_{12} would be able to reproduce at least T_c [9].

where $n_j = 1$ for an ion A and $n_j = 0$ for an ion B. The approximation is now to replace n_j by the doping concentration $n_j \sim x_A$ assuming a homogeneous distribution of the ions. This decouples the problem into two separate meanfield Hamilton operators for A and B connected only by an induced field. In the algorithm iteratively both Hamiltonian are diagonalized and the meanfields are updated until selfconsistency is reached. In the special case of dilution with nonmagnetic ions, like for example in $\text{LiHo}_x\text{Y}_{1-x}\text{F}_4$, the virtual crystal approximation is trivial and equivalent to the treatment of the pure system but with a scaling of the interaction $\tilde{\mathcal{J}}(\mathbf{0})$ proportional to the concentration x . Hence also T_c and H_c are scaled by this factor, because of their linear relation to $\tilde{\mathcal{J}}(\mathbf{0})$.

To calculate the generalized susceptibilities in RPA the starting point is again the general relation 3.2.12 in real space.

$$\bar{\chi}(ij, \omega) = \bar{\chi}_i^0(\omega) \left(\delta_{ij} + \sum_{j'} \bar{\mathcal{J}}(ij') \bar{\chi}(j'j, \omega) \right). \quad (3.3.4)$$

Here the non-bravais lattice has to be considered in the decoupling by means of Fourier transform. Finally the following expression is obtained.

$$\bar{\chi}(\mathbf{q}, \omega) = \frac{1}{4} \sum_{rs} \bar{\chi}_{rs}(\mathbf{q}, \omega) = \frac{1}{4} \sum_{rs} \left[\bar{\mathcal{M}}^{-1}(\mathbf{q}, \omega) \right]_{rs} \cdot \bar{\chi}_r^0. \quad (3.3.5)$$

$$\left[\bar{\mathcal{M}}(\mathbf{q}, \omega) \right]_{rs} = \delta_{rs} \bar{\mathbb{1}} - \bar{\chi}_r^0(\omega) \cdot \bar{\mathcal{J}}_{rs}(\mathbf{q}). \quad (3.3.6)$$

In expression (3.3.6) the (12×12) matrix $\bar{\mathcal{M}}$ is defined block wise, where $[\cdot]_{rs}$ labels the (3×3) block that corresponds to the indices r and s . $\bar{\mathbb{1}}$ stands for the identity matrix. Furthermore, $\bar{\mathcal{J}}_{rs}(\mathbf{q})$ denotes the Fourier transformed coupling tensor with respect to the ions of sublattice r and s . The transformation for $\bar{\chi}_{rs}(\mathbf{q}, \omega)$ are defined similarly.

$$\mathcal{J}_{rs}^{\alpha\beta}(\mathbf{q}) = \frac{1}{N} \sum_{j \in r} \sum_{j' \in s} \mathcal{J}^{\alpha\beta}(j, j') e^{-i\mathbf{q}(\mathbf{R}_j - \mathbf{R}_{j'})}. \quad (3.3.7)$$

The single-ion susceptibilities $\bar{\chi}_r^0$ of an ion in the sublattice r are calculated within the meanfield eigenstates $|n\rangle$ and energies E_n

$$\bar{\chi}_r^{0,\alpha\beta}(\omega) = \lim_{\varepsilon \rightarrow 0^+} \sum_{nm} \frac{\langle n | J_r^\alpha | m \rangle \langle m | J_r^\beta | n \rangle}{E_m - E_n - \omega - i\varepsilon} (n_n - n_m). \quad (3.3.8)$$

Although the meanfield/RPA treatment leads to a qualitatively correct description of the LiReF₄ system there are some shortfalls with regards to systematic overestimations of the critical fields and temperatures as well as partly underestimation of the energies of the collective excitations. The deeper reason for this is the fact that fluctuations are neglected in the approximation already by definition. Therefore it is also understandable that in case of the Ising ferromagnet LiHoF₄ meanfield treatment leads to acceptable results and fits better compare to the case of the planar antiferromagnet LiErF₄. There are a few attempts reported for a more sophisticated theoretical modeling of the LiHoYF₄, like classical and quantum monte carlo [25, 23] or exact diagonalization [10]. Furthermore there is also a more analytical approach, an improvement towards the next higher order in the Dyson relation of the Greensfunction in form of a $1/z$ expansion [24]. In this framework RPA would be the zero order result. Nevertheless also this method has its own limitations, among others it is applying only to truncated effective Hamiltonians with reduced complexity. Hence a sophisticated theoretical description beyond meanfield is still missing.

3.4 Random Field Model Systems

Random field magnets provide an arena to address the question how imperfection and disorder affect the magnetic properties in real magnets in comparison to the clean ideal system. In this models there is a perturbation field that varies from site to site in magnitude and polarization, whereas the overall mean equals zero. Experiments have demonstrated that the presence of random field is able to change significantly critical exponents [26].

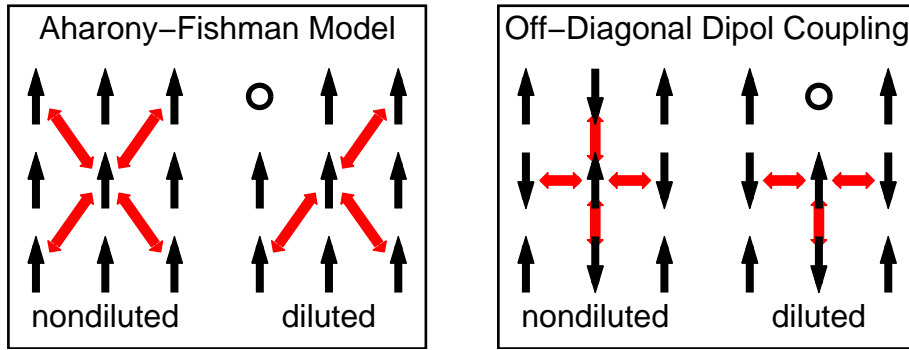


Figure 3.6: Two methods to realize a random-field model: Site diluted antiferromagnet (Aharony-Fishman) or via off-diagonal coupling terms in a diluted Ising ferromagnet. The interactions (red) are drawn schematically in the pure and diluted compounds to emphasis that in the nondiluted case random fields cancel out by symmetry. Figure reproduced from [27].

A tunable random field can be realized for example in the two different models as shown in figure 3.6. The first proposition according to Aharony and Fishman [28], is a site-diluted antiferromagnet in an external magnetic field. The second model is a diluted Ising ferromagnet where longitudinal random fields are induced by an applied transversal field via off-diagonal interactions. This is exactly the situation in $\text{LiHo}_x\text{Y}_{1-x}\text{F}_4$ where off-diagonal terms are an intrinsic feature of dipolar coupling [29, 30, 10, 31]. As a second perturbation theory results the random field at site j is given as

$$h_j = \frac{2SH_t}{\Omega_0} \sum_i \mathcal{J}_{ji}^{zx}, \quad (3.4.1)$$

where Ω_0 denotes the splitting between the doublet ground state and the first excited singlet. The magnitude of the random field is governed by the grade of dilution and can be tuned in each particular compound via the applied transversal field. For any $x < 1$ and a decent $H_t > 0$ the system can be regarded as an almost perfect realization of a classical Random Field Ising

Model (RFIM). Although this picture and the manifestation of random fields due to dipolar interactions is generally accepted, some theoretical details and the consequences are controversially debated [29, 30, 10, 31].

It was argued [10] that for $\text{LiHo}_x\text{Y}_{1-x}\text{F}_4$ a true spin glass state can exist in the limit of $H_t = 0$ only, whereas for any $H_t > 0$ the random fields limit the correlation length. Instead of a quantum critical spin glass transition a ‘quasi’-spin glass to paramagnet cross-over takes place as a function of the transversal field. Hence it is assumed that the presence of dipolar interactions circumvent the formation of a quantum spin glass and the TFISG is questioned as an adequate model for $\text{LiHo}_x\text{Y}_{1-x}\text{F}_4$. Nevertheless, there is so far neither a strict theoretical nor experimental verification or falsification of the emergence of a spin glass in its quantum limit and it seems that the subtle interplay between the counteracting random fields and quantum fluctuations may be decisive. In the less diluted $\text{LiHo}_x\text{Y}_{1-x}\text{F}_4$ compounds, which are ferromagnetically ordered, the consequences of the random fields are suppressed values for the critical fields and the appearance of Griffith singularities [27].

Chapter 4

Experimental Results and Discussion

The structure of this chapter is subdivided according to the particular compounds and the associated effects. An exception is the next section, in which the characterization of the crystal fields for various compounds is summarized. For the understanding of the investigations presented later on in this thesis only the crystal field properties of LiErF_4 and LiHoF_4 are relevant, whereas the other compounds are listed only for completeness. The section 4.2 is assigned to aspects of spin glass physics and random field magnets in the compounds of the dilution series $\text{Li}(\text{HoY})\text{F}_4$. In section 4.3 the quantum phase transition in LiHoF_4 , in particular the effect of coupling to a spin bath, will be discussed. The sections 4.4 and 4.5 are devoted to the antiferromagnet LiErF_4 . The discussions of the general magnetic properties of the system, the phase diagram and the thermal and quantum criticality are covered in 4.4, whereas in 4.5 the dynamical properties of the system are considered. Finally, as an outlook some preliminary results of the mixed crystals $\text{Li}(\text{HoEr})\text{F}_4$ are presented in the last section.

4.1 Crystal Fields

The local magnetic properties of the ion, like the effective magnetic moment or the anisotropy, i.e. whether Ising or planar is defined by the crystal field. An accurate characterization of the local single ion behavior is inevitable for all further experimental investigations and attempts to theoretical modeling of the collective effects, which are in the focus of interest. The intention is therefore to refine the 6 crystal field parameters experimentally. The method of choice is inelastic neutron spectroscopy, since this provides directly the energy levels and via the transition matrix elements information on the cor-

responding wave functions. The crystal field levels are non dispersive and the general advantage in selectivity of three axis instruments is less important compare to the total required beam time. A time of flight spectrometer on the other hand has a high data acquisition rate for several wave vectors in parallel and gives the full spectra in a particular energy window. In the following a time of flight neutron spectroscopy crystal field investigation on the compounds LiReF_4 , $\text{Re}=\text{Ho}, \text{Er}, \text{Tm}, \text{Yb}$ is presented. Symmetry arguments are not only helpful in the data interpretation and refinement of the crystal field parameters but also has general direct consequences to the spin anisotropy and the level splitting in LiReF_4 .

4.1.1 Symmetry Arguments and General Considerations

The symmetry at the position of the rare earth ions in LiReF_4 is given by the S_4 group. In a crystal field the $2J + 1$ degenerated multiplet is splitting up according to four irreducible representations, hence the digitalization of \mathcal{H}_{cf} can be done blockwise in the following subspaces.

$$V_\alpha = \text{span}\{|m = \alpha\rangle, |\alpha \pm 4\rangle, |\alpha \pm 8\rangle, \dots\}. \quad (4.1.1)$$

$$\begin{aligned} \alpha &= 0, \pm 1, 2 && \text{for J integer.} \\ \alpha &= \pm \frac{1}{2}, \pm \frac{3}{2} && \text{for J half integer.} \end{aligned}$$

Since the crystal field splitting are induced by electrical fields of the neighboring ions only, i.e. has a nonmagnetic origin, the time reversal is symmetry of the Hamiltonian. The time reversal operator maps the states from $|m\rangle$ to $| -m\rangle$ and therefore acts in the following way on the subspaces V_α .

$$T = e^{-i\pi J_y} K : V_\alpha \rightarrow V_{-\alpha}. \quad (4.1.2)$$

Here K denotes the complex conjugate. Since $T|\psi\rangle$ of an eigenstate $|\psi\rangle$ is itself an eigenstate to the same energy one obtains the following level splitting schema.

- J integer singlet A: $\{V_0\}$ B: $\{V_2\}$
 doublet E: $\{V_{\pm 1}\}$
- J half integer doublet E': $\{V_{\pm 1/2}\}$ E'': $\{V_{\pm 3/2}\}$

A, B, E is the notation often used in representation tables. Obviously the doublet degeneracy in the half integer case is a consequence of Kramers Theorem.

Furthermore from the breakdown in terms of the subspace V_α it is evident that $g_\perp = 0$ for all doublets belonging to E in the case of J integer and for all singlets $g_{\perp/\parallel} = 0$, obviously. Therefore the doublet states E represent Ising spins along the z-axis and usually large g_\parallel factors. On the other side for J half integer a realization of almost planar effective spin anisotropy is within the realms of possibility.

In the neutron scattering cross-section the matrix elements of \mathbf{J} between two states are involved. In each transition between two different types of representation, for example from E' to E'' , the matrix elements involving J_z are zero. Furthermore in the J integer case for the transitions between A and B or within the sets A, B and E the matrix elements involving J_x , J_y are zero. Therefore there is a momentum dependent anisotropy in the scattering intensity. From an experimental point of view this provides further directly assignable information from the measured spectra. Hence, in some cases one can afford to choose a powder sample instead of a single crystal without causing restrictions in the data evaluation and crystal field parameter refinement.

4.1.2 LiErF₄

In LiErF₄ the $2J + 1 = 16$ dimensional ground state multiplet is split into 8 doublets of E' and E'' in each case. The neutron measurements have been performed on a single crystal sample in two different orientations, the low energy part on the FOCUS (SINQ, PSI) spectrometer with $E_i = 12$ meV as well as the high energy part on the LRMCS (IPNS, Argonne) spectrometer with $E_i = 80$ meV. Although the instrument is not Q-selective the sample alignment has been optimized such that the covered reciprocal space region is centered either around $Q = (\xi, 0, 0)$ or $Q = (0, 0, \xi)$. The crystal was oriented with one a-axis pointing perpendicular to the scattering plane, therefore a 90° rotation of the sample around this axis allowed to change between the two different configurations under otherwise fixed conditions. Collecting data sets at different temperatures, here 2 K and 20 K for the experiment in the low energy sector (figure 4.1) respectively 11 K and 100 K for the high energy part (figure 4.2), has the advantage of determining ground state transitions as well as transitions from a few of the next lowest excited states. This provides additional as well as redundant information than measuring at only one particular temperature and therefore enhances the consistency of the determined quantities.

The anisotropy visible from the spectra and the above mentioned symmetry considerations anticipate already qualitatively the level splitting. However from the quantitative analysis it is known that the ground state belongs to the representation E'' . In the transition to second excited state $E = 3.52$ meV there is little intensity in the configuration $Q \sim (0, 0, \xi)$ compared

to the pronounced peak visible in the case of $Q \sim (\xi, 0, 0)$. Hence the J_z matrix element is nonzero, leading to the conclusion that the second excited state must belong to the same representation E'' as the ground state. The same argument holds for the $E = 43.4$ meV state. On the other side there is slightly more intensity in the c-axis orientation for the transition to the first and third state but less for the transition between these two. Considering these ratios and the fact that each representation has four doublets the only possible conclusion is that the first and third excited state must belong to the other representation E' .

The limited data published on the magnetic properties of LiErF_4 to date include susceptibility, specific heat, EPR and optical measurements of crystal field levels [32, 33, 34, 35], agreeing on planar XY anisotropy $g_\perp \simeq 8.09 - 8.105 \gg g_\parallel \simeq 3.14 - 3.32$, although lacking a globally consistent set of parameters allowing detailed prediction of low-temperature properties. Based only on the neutron data here a more reliable full refinement of the crystal field Hamiltonian is presented. The determined crystal field parameters are compared with the values reported from literature in table 4.1. Furthermore as a consistency check the bulk susceptibility, measured on a SQUID magnetometer, can be reproduced well by the calculation using the actual parameter set (figure 4.3). The resulting level schema, measured and calculated, is given in table 4.2. As a conclusion the crystal field yield a ground state doublet with $\Delta = 2.25$ meV to the next excited Kramers doublet. Within the ground-state doublet, an effective system for the low-temperature magnetic properties that can be derived, suitable for future theoretical work. Inside this subspace the effective spin operators can be written as $S^\alpha = C_\alpha \sigma^\alpha$, where $C_x = C_y = 3.480$ and $C_z = 0.940$, which directly feature the pronounced XY-anisotropy of the system. Furthermore with the refined crystal field parameters the values $g_\parallel = 2.25$ and $g_\perp = 8.35$ are calculated.

	$10^3 B_2^0$	$10^3 B_4^0$	$10^3 B_4^4(c)$	$10^3 B_4^4(s)$	$10^6 B_6^0(c)$	$10^6 B_6^4(c)$	$10^6 B_6^4(s)$
Refinement	63.0 ± 5.9	-0.55 ± 0.03	-5.54 ± 0.07	0.47 ± 0.01	-0.006 ± 0.006	-108.2 ± 1.2	-14.6 ± 0.5
Pointcharge	26.9	-0.12	-1.74		-0.040	-11.5	-2.4
Ref. [36]	67.7	-0.68	-6.82		-0.080	-133.0	-24.3

Table 4.1: Crystal-field parameters in meV for LiErF_4 . The present refinement is compared with values reported in [36] and a point charge calculation.

Neutron spectr.	calculated	EPR [34]	Opt. spectr. [35]	Ref. [36]
2.23 ± 0.01	2.23	2.26	2.23	2.33
3.52 ± 0.01	3.52	2.90	2.48	3.79
7.00 ± 0.01	7.01		7.44	8.19
31.3 ± 0.2	31.9			39.0
35.8 ± 0.2	36.7			44.6
	40.1			49.3
43.4 ± 0.3	43.2			52.9

Table 4.2: Crystal-field level energies for LiErF_4 in meV, relative to the ground state. All states are Kramers degenerate doublets. The results obtained from neutron spectroscopy in comparison with the calculated energies (refined parameters) and with the values reported in literature.

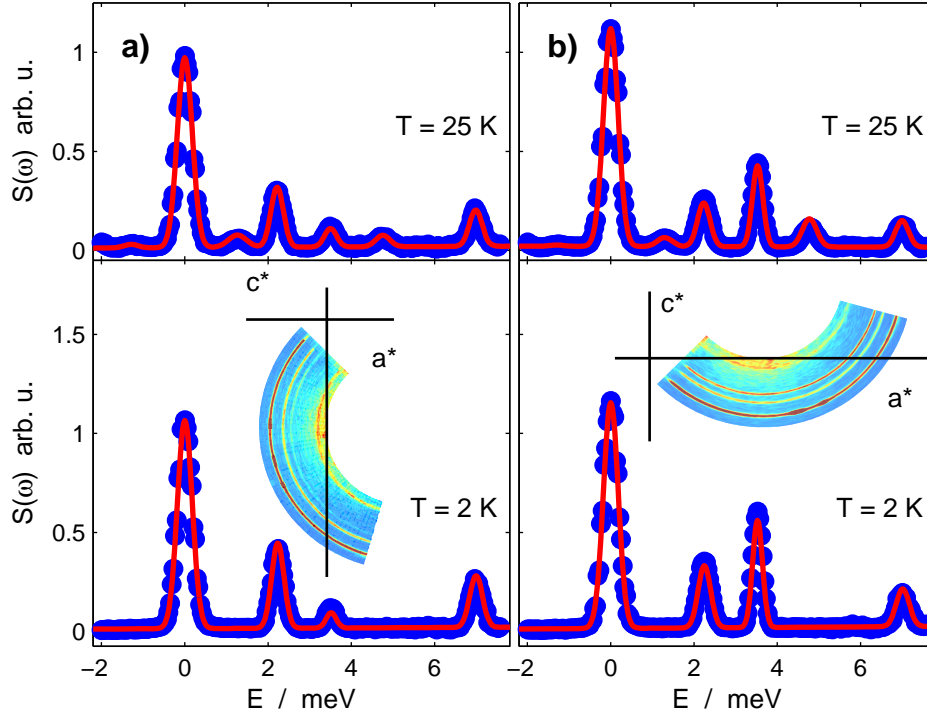


Figure 4.1: Time-of-flight spectra for LiErF_4 measured on the FOCUS spectrometer at two different temperatures and two different crystal orientations. a) $Q \approx$ along the 'c-axis', b) $Q \approx$ along the 'a-axis'. In the insets the considered region in reciprocal space is visualized. The red line shows calculated intensity with the refined set of the crystal field parameters.

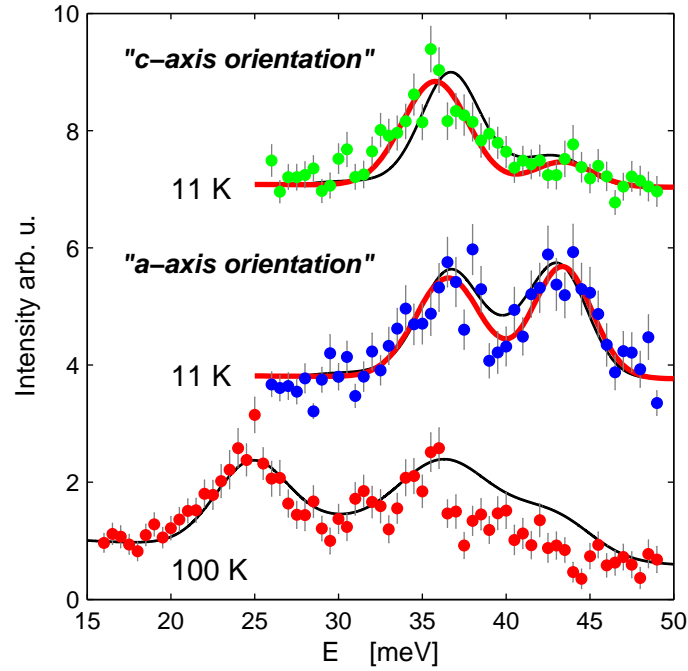


Figure 4.2: High energy part of the LiErF_4 crystal field spectrum measured on LRMCS for two different crystal orientations. The red line represents a fit with gaussian curves, used to extract the transition energies. The black curves show the spectra obtained from a calculation based on the refined set of the crystal field parameters.

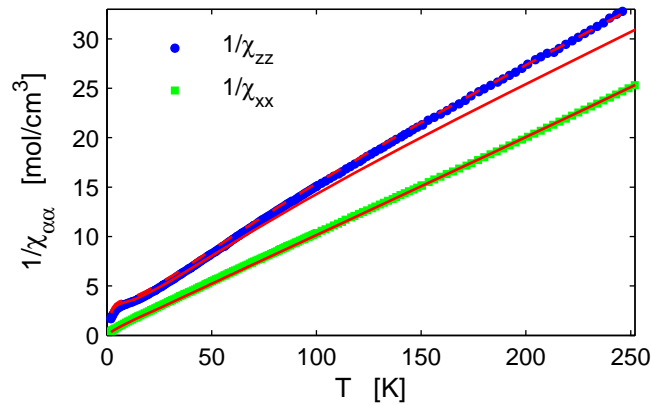


Figure 4.3: Bulk susceptibility of LiErF_4 obtained from SQUID magnetometry with a field of 1 kOe. The calculation based on the crystal field Hamiltonian is able to reproduce well the experimental results, without any scaling parameter (red curve). The dashed curve shows the c-axis susceptibility enhanced about 7.5%.

4.1.3 LiHoF₄

In LiHoF₄ the $2J + 1 = 17$ dimensional ground state multiplet is split into 4 doublets and 9 singlets. Although no neutron data exist in literature, already a quite accurate crystal field parameter set is reported, based on a refinement of the data from several independent bulk investigations [36]. The here presented neutron measurements has been performed with a powder sample at the TOFTOF time-of-flight spectrometer at FRMII in Munich. For the instrument configuration an incident wavelength of 2.8 Å has been chosen, which allows to collect data on the crystal field transitions up to an energy around 9 meV. The use of a powder sample circumvents in the data evaluation the uncertainties arising of an improper orientation of a single crystal. On the other hand in the powder cross-section the information of anisotropy in the matrix elements is averaged out. Three data sets have been collected at temperatures of 4, 25 and 70 K, see Fig 4.4. The measured transition energies are summarized in table 4.3.

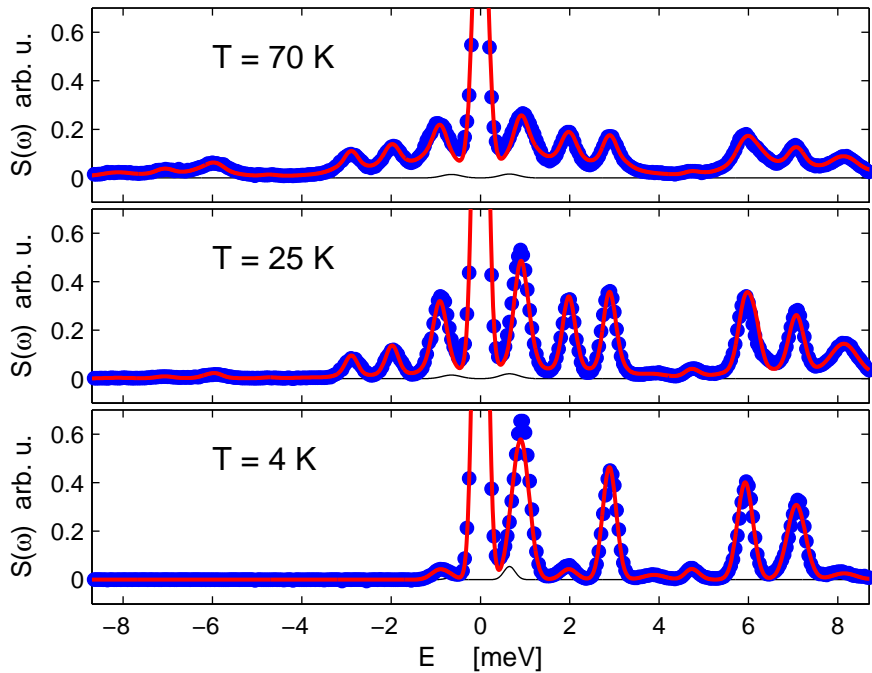


Figure 4.4: Time of flight spectra for LiHoF₄ measured at three different temperatures. The red line shows calculated intensity with the refined set of the crystal field parameters. The sample contained traces of HoF₃ from incomplete synthesis. In the data evaluation this contribution to the spectra was considered, shown as black line.

Based on this data a full refinement of the crystal field Hamiltonian was possible and the crystal field parameters are compared with the values reported from literature in Table 4.4. The resulting level schema is given in Table. 4.3. The ground state doublet is separated ≈ 11 K from the next higher state, which is a singlet. All doublets belong to the representation E and $g_{\perp} = 0$ is a direct consequence of the symmetry. Therefore at low temperatures LiHoF₄ is a perfect realization of an Ising system.

neutron spectr.	calc.	[24]	[36]	[34]	[35]	[37]
0.90 ± 0.01	0.92	0.95	0.78	0.90	0.99	
2.90 ± 0.01	2.89	2.76	3.36	2.87	3.22	
5.94 ± 0.01	5.90	6.20	6.38		6.08	
7.08 ± 0.01	7.02	7.24	7.93		7.56	7.33
9.06 ± 0.01	8.98 [†]	9.39	10.69		9.67	8.79
	25.7	28.3	34.3			
	31.7	34.8	42.4			
	32.0 [†]	35.3	42.8			35.1
	32.9	36.2	44.0			
	35.2	37.7	46.1			
	35.9 [†]	38.2	47.1			39.0
	37.8	40.4	49.6			

Table 4.3: Crystal-field level energies in meV, relative to the ground state doublet, for LiHoF₄. The results obtained from neutron spectroscopy in comparison with the calculated energies based on the refined crystal field parameters and with the values reported in literature, i.a. experimental results from previous EPR [34] and optical spectroscopy [35]. The doublets are indicated by [†].

	$10^3 B_2^0$	$10^3 B_4^0$	$10^3 B_4^4(c)$	$10^6 B_6^0(c)$	$10^6 B_6^4(c)$	$10^6 B_6^4(s)$
refinement	-63.2±4.8	0.318±0.016	3.42±0.04	0.55±0.01	60.1±0.1	18.9±0.1
Ref. [24]	-60.0	0.350	3.60	0.40	70.0	9.8
Ref. [36]	-65.0	0.426	4.53	0.10	85.5	16.9
Ref. [38]	-52.0	0.281	3.70	0.70	70.4	
Ref. [39]	-56.0	0.325	3.61	0.20	75.8	

Table 4.4: Crystal-field parameters in meV for LiHoF₄ from the present refinement compared with values reported in literature.

4.1.4 $\text{LiHo}_x\text{Y}_{1-x}\text{F}_4$ and the Effect of Dilution

The method, which was far mostly used to determine crystal field parameters in $\text{LiRe}_x\text{Y}_{1-x}\text{F}_4$ was optical spectroscopy on very dilute isolated Re-ions. Nevertheless it has not been tested, whether crystal field parameters determined in very dilute systems remain valid in the Re-rich system and vice versa. Two compounds have been chosen, LiHoF_4 and $\text{LiHo}_x\text{Y}_{1-x}\text{F}_4$ with $x = 4.5\%$, to measure both under exactly the same experimental configuration on the TOFTOF spectrometer. Since there is much less scattering from the diluted compound, not the same settings could be used as presented in the previous paragraph for LiHoYF_4 . A high resolution configuration is mandatory to distinguish accurately the small differences between the two samples. This, on the other hand, causes a reduction of the instrumental accessible energy window. In the present window only the first three lines are observable, which is unfortunately not sufficient information for a full refinement of the crystal parameters. The main result of the measurement is that there is a significant shift in the crystal level energy between the diluted and pure compound (Fig. 4.5, 4.6).

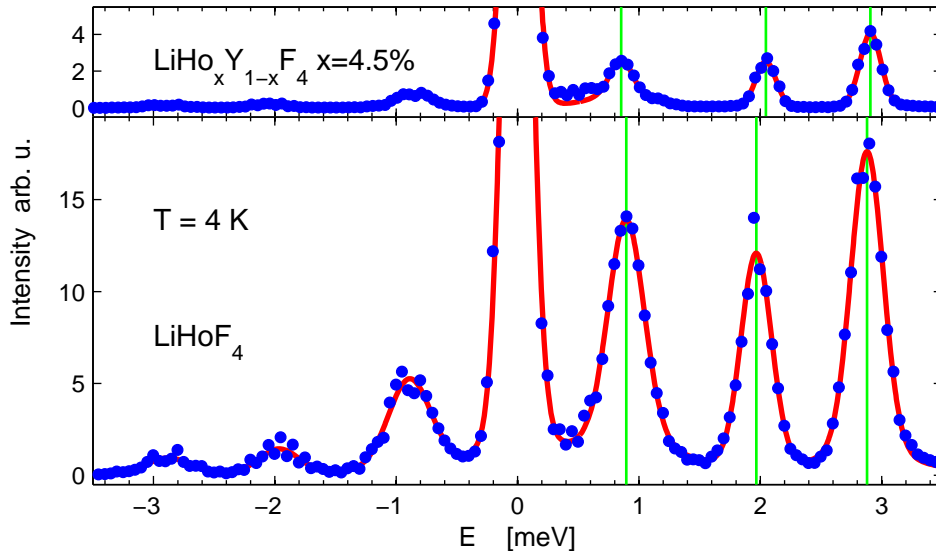


Figure 4.5: Comparison of the time of flight spectra for LiHoF_4 and $\text{LiHo}_x\text{Y}_{1-x}\text{F}_4$, $x = 4.5\%$. The shift in the energy levels between the two compounds is visualized by the green vertical lines, which indicate the positions of the spectral lines according to the fit (red curve).

Additionally, also the crystal field transition from the ground state doublet to the first excited singlet state was measured with enhanced resolution (figure 4.6). The line width in the pure compound is approximately five times

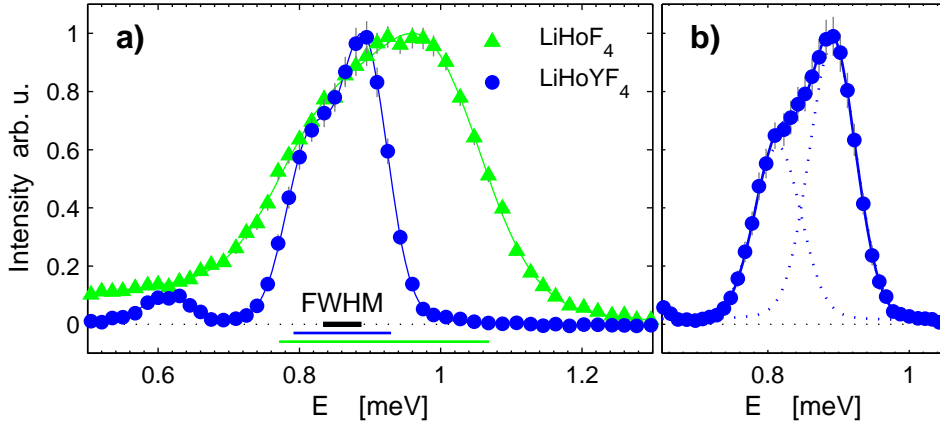


Figure 4.6: High resolution neutron time of flight spectra of the first spectral line in $\text{LiHo}_x\text{Y}_{1-x}\text{F}_4$, $x = 4.5\%$ compared with LiHoF_4 . The FWHM is indicated through the bars on the bottom of the graph, where the black one corresponds to the resolution of the elastic line. The broadening is enhanced in the pure compound compare to the diluted (a), whereas in the latter splitting is visible in the peak shape(b).

broader than the instrumental resolution and in the spectra of the diluted compound a double-peak shape was observed. The obvious interpretation would be that this originates from the zeeman-splitting in the ground state doublet due to the magnetic interaction between the ions. Hence the broadening is related to the statistical distribution of the different interactions. The splitting observed in the diluted compound is in the order of the energy expected from the dipolar coupling between two neighbouring ions. Therefore, this interpretation seems plausible. Furthermore, the splitting due to the rather strong hyperfine interaction in Holmium will contribute to a smearing out of the spectra too.

4.1.5 LiTmF_4

In LiTmF_4 the $2J + 1 = 13$ dimensional multiplet is split into 3 doublets and 7 singlets. The low energy part of the spectrum has been measured on a powder sample at the FOCUS spectrometer with $E_i = 7$ meV and the high energy part at the LRMECS spectrometer with $E_i = 80$ meV. At base temperature there are two clearly identifiable spectral lines one at $E = (3.77 \pm 0.01)$ meV and the other at $E = (34.6 \pm 0.1)$ meV, see figure 4.7&4.8. From optical spectroscopy [40, 41] it is reported that the ground state is a singlet and the first excited state a doublet at 3.84 meV.

Since the available information from the neutron data is far from sufficient for a full determination of the six crystal field parameters also the optical determined energy levels [41] are considered in the refinement. Recently reported data on bulk magnetization [42] show that the inplane magnetization $M_{\perp(001)}$ is highly anisotropic in high fields and at low temperatures around 4.2 K. The maximal value of the magnetization is reached at an angle $\phi = 12.5^\circ$ between applied field and crystallographic a-axis. For a field of $H_{\perp(001)} \approx 50$ kOe the anisotropy $M_{\perp}(\phi_{max}) - M_{\perp}(\phi_{min})$ is 1.11 Bohr magneton per ion or 32% of the mean value. The low field susceptibility $\chi_{\perp}(T = 4.2 \text{ K}) = 0.071 \mu\text{B}/\text{kOe}$ is isotropic according to first order perturbation theory. By a rotation in the xy-coordinate frame the obtained crystal field parameters $B_4^4(c)$, $B_4^4(s)$ and $B_6^4(c)$, $B_6^4(s)$ have been transformed to match the calculated with the experimental determined orientation of maxima and minima of the inplane magnetization. Such a coordinate transformation from old parameters B to new \tilde{B} is given as follows, where the rest of the parameters remains the same.

$$\begin{aligned}
\tilde{B}_4^4(c) &= B_4^4(c) \cos(4\alpha) + B_4^4(s) \sin(4\alpha) \\
\tilde{B}_4^4(s) &= B_4^4(s) \cos(4\alpha) - B_4^4(c) \sin(4\alpha) \\
\tilde{B}_6^4(c) &= B_6^4(c) \cos(4\alpha) + B_6^4(s) \sin(4\alpha) \\
\tilde{B}_6^4(s) &= B_6^4(s) \cos(4\alpha) - B_6^4(c) \sin(4\alpha).
\end{aligned} \tag{4.1.3}$$

Here α denotes the rotation angle between the old and new coordinate frame. If the reported data is scaled by a consistent factor of 0.88, the magnetization calculated using the new refined crystal field parameters coincides well with the experimental values, except that the anisotropy is underestimated, similar as in the model of [42]. It was not possible to circumvent this scaling factor by a different choice of the crystal field parameters, without disturbing significantly the energy level schema. The needed scaling factor is maybe due to some incorrectness in the treatment of the demagnetization in the reported data from [42]. Nevertheless the agreement in regards of the the bulk magnetization data is as good as in the model of [42], but here in contrast to their reorganization also the correct energy levels are taken into account.

	$10^3 B_2^0$	$10^3 B_4^0$	$10^3 B_4^4(c)$	$10^3 B_4^4(s)$	$10^6 B_6^0(c)$	$10^6 B_6^4(c)$	$10^6 B_6^4(s)$
Refinement	224.3 ± 8.2	-1.85 ± 0.06	-11.7 ± 0.4	-15.2 ± 0.5	2.0 ± 1.9	264.5 ± 27.4	137.7 ± 26.5
Ref. [40]	224.6	-1.54	-17.9		7.5	306.8	

Table 4.5: Crystal-field parameters for LiTmF_4 in meV. The parameters from the present refinement are compared with values reported in [40].

Neutron spectr.	calculated	Ref. [41]
3.77 ± 0.01	3.77^\dagger	3.84
	7.69	7.69
	34.6	35.6
	39.2	39.2
	45.3	45.3
34.6 ± 0.1	47.4^\dagger	47.4
	50.8^\dagger	50.8
	52.2	52.2
	54.1	54.1

Table 4.6: Crystal-field level energies of LiTmF_4 in units of meV relative to the ground state singlet. The doublets are indicated by † . The results obtained from neutron spectroscopy in comparison with the values reported from previous optical spectroscopy investigations and the calculated energies using refined parameters.

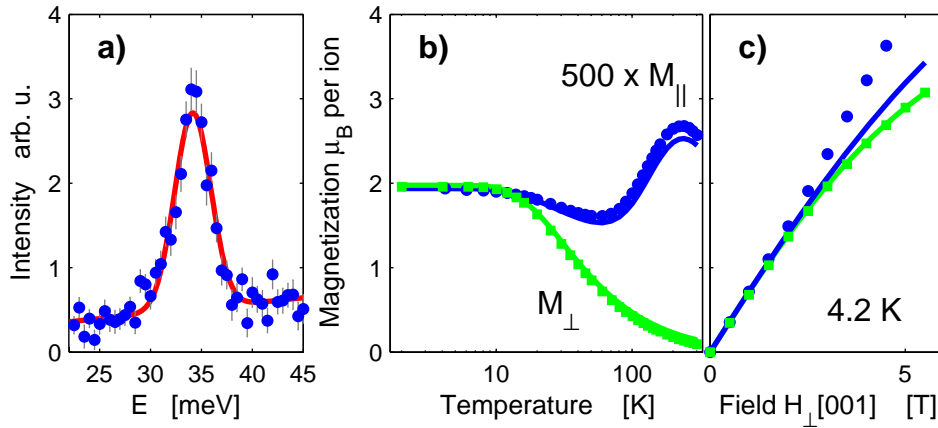


Figure 4.7: (a) Spectral line at $E = (34.6 \pm 0.1)$ meV measured with time of flight on a LiTmF_4 powder sample. (b) Temperature of the parallel and perpendicular component of the magnetization. M_{\perp} is measured for a field along the direction with minimal in plane magnetization. (b) Anisotropy of in plane magnetization at 4.2 K, field dependence in maximal direction (blue) and minimal direction (green). The data points in (b,c) are taken from [42]. The lines (b,c) showing the calculated curves according to the presented crystal field parameters.

As a difference to the majority of cases observed in LiReF_4 , where the spectral lines are nearly resolution limited, in LiTmF_4 the line width of the 3.8 meV transition increases enormous at increasing temperatures (figure 4.8 & 4.9). Further contribution of other crystal field transition due to thermal population can be ruled out as origin of the broadening, since they are located at much higher energies. Therefore we conclude that the broadening is due to magnetic interactions and coupling to collective, nonlocal degree of freedoms. In a metal for example the magnetic interactions with conduction electrons induce a temperature dependent finite life time of an excited CEF state leading to the line width linear in temperature, which is known as Korringa law. Furthermore giant, strong anisotropy magnetostriction effects are reported for LiTmF_4 [43], therefore the damping could be a consequence of a magneto-phononic hybridization with the crystal field states.

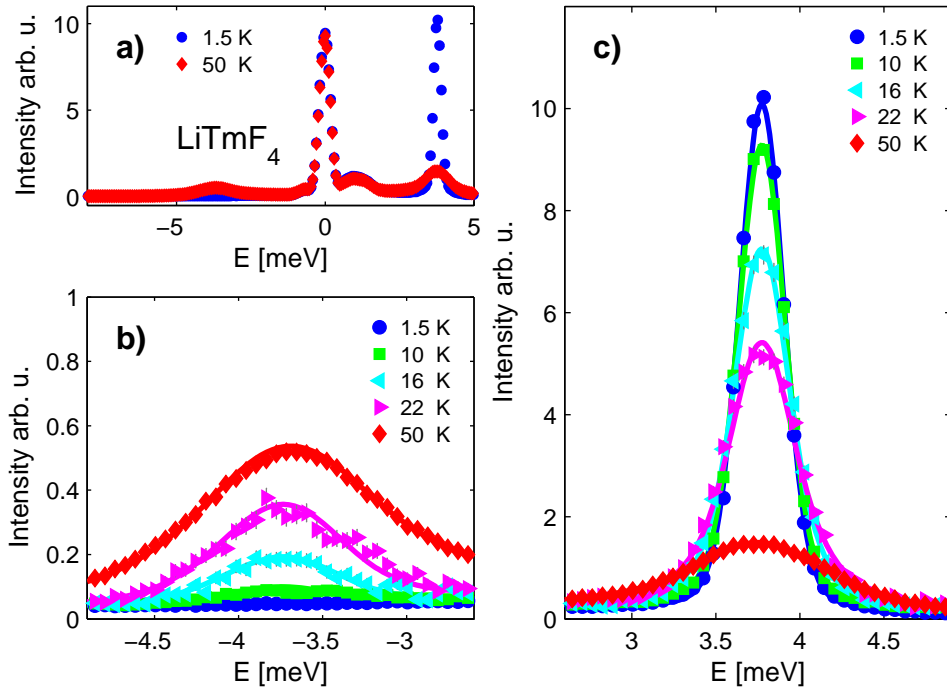


Figure 4.8: Crystal field neutron scattering spectrum measured in LiTmF_4 . Panel (b) and (c) are zoomed in illustration on energy gain and loss side respectively to visualize the temperature dependence of the peak shape. The line width dramatically increase with temperature (figure 4.9). The lines correspond to a fit using a detailed balance Lorentzian model function.

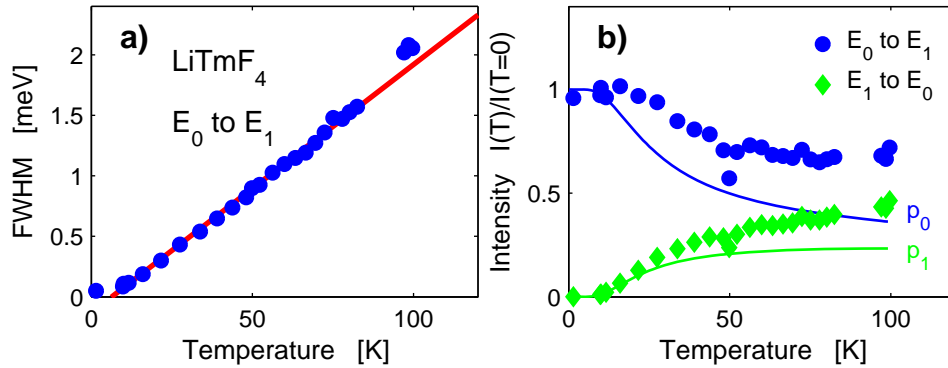


Figure 4.9: Line width (a) and intensity (b) of the $E = 3.77$ meV transition in LiTmF_4 determined from the fits to data as shown in figure 4.8. The intensity for the gain and loss processes are related to each other by the detailed balance condition. Solid lines in (b) are showing the population factors according to the crystal field level splitting, i.e. the expected temperature dependence of the scattering intensities in the isolated ion picture cross section.

4.1.6 LiYbF_4

In LiYbF_4 the $2J + 1 = 8$ dimensional multiplet is split up into 4 Kramers degenerate doublets. All transitions from the ground state to the 3 excited doublets were measurable on the LRMCS spectrometer with $E_i = 80$ meV using a powder sample (Fig. 4.10). The determined energy levels are similar to the values reported from optical spectroscopy [44], see Tab. 4.7 for comparison. The refined crystal field parameters are listed in table 4.8. In the refinement the parameter $B_4^4(s)$ was kept zero, because the available data is insensitive to the orientation of the xy-coordinate frame. Furthermore, also the parameter $B_6^4(s)$ was set to zero, since the fit was almost insensitive to this value. For the sample used in the neutron spectroscopy also the bulk susceptibility was measured with a PPMS. Based on the new adjusted parameters the calculation is able to describe the susceptibility as well as the neutron data (Fig. 4.10).

Neutron spectr.	calculated	Optical spectr. [44]
29.0 ± 0.2	28.9	29.4
46.3 ± 0.4	45.9	46.5
55.2 ± 0.3	55.2	59.1

Table 4.7: Crystal-field level energies of LiYbF_4 in units of meV relative to the ground state. All states are Kramers degenerate doublets. Comparison of neutron spectroscopy results with the values reported from previous optical spectroscopy investigations and the energies calculated using the refined parameter set.

$10^3 B_2^0$	$10^3 B_4^0$	$10^3 B_4^4(c)$	$10^3 B_6^0(c)$	$10^3 B_6^4(c)$	$10^3 B_6^4(s)$
663 ± 80	12.5 ± 4.5	102 ± 41	-0.62 ± 0.73	-16.0 ± 1.7	0

Table 4.8: Crystal-field parameters for LiYbF_4 from the present refinement in meV.

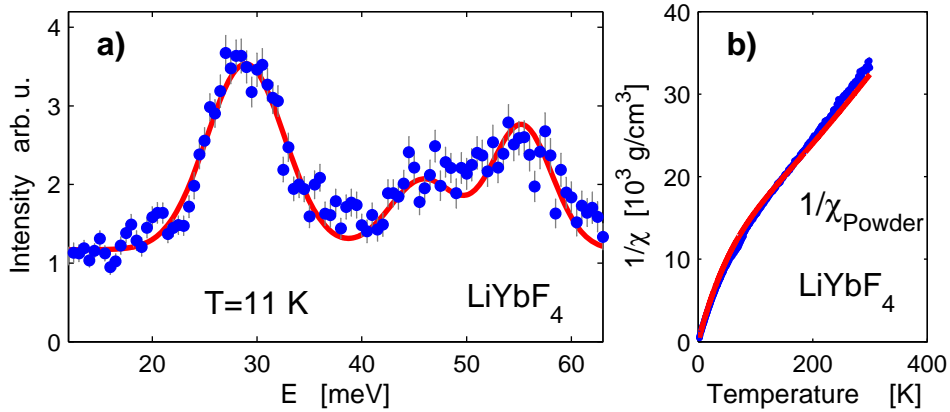


Figure 4.10: (a) Time of flight spectra of LiYbF_4 (powder sample). (b) Susceptibility of the same sample, measured with PPMS. The red curves in both panels are the results obtained from calculation using the refined crystal field parameters.

Summary 4.1:

A crystal field investigation and by means of neutron spectroscopy and a comprehensive crystal field parameter refinement was presented for the compounds LiReF_4 with $\text{Re}=\text{Er}$, Ho , Yb and Tm . Furthermore the following results and conclusions have been obtained:

- Based on symmetry considerations a derivation of the energy level schema is given.
- LiErF_4 is within its ground-state doublet a realization of an XY model.
- LiHoF_4 is within its ground-state doublet a perfect realization of an Ising Model with $g_{\perp} = 0$ fulfilled exactly.
- In the diluted compound $\text{LiHo}_x\text{Y}_{1-x}\text{F}_4$, $x = 0.045$, the crystal field energy levels are slightly shifted (< 0.1 meV) compare to the values found for the pure compound. The Line width of the first crystal field transition line is significantly broadened in the case of the pure compound.
- In LiTmF_4 the line width exhibit a linear increase as a function of temperature.

4.2 $\text{LiHo}_x\text{Y}_{1-x}\text{F}_4$

The dilutions series LiHoYF_4 are without question so far the most celebrated representative of the LiReF_4 compounds because of their model character and numerous collective quantum phenomena. The main experimental method of almost all investigations was ac-susceptibility. The here presented neutron diffraction results are complementary to the reported macroscopical measurements and provide a new inevitable insight into the microscopic picture. This section is subdivided in three parts. In the first part (4.2.1), the evolution of the phase diagram as function of dilution x and particular aspects of the measured compounds are discussed. However, the reentrant spin glass systems $x = 0.33$ and $x = 0.46$ and quantum annealing are presented in a self-contained paragraph, i.e. in the second part (4.2.2) of this section. Finally, the third part (4.2.3) is devoted to the coherent oscillations of spin clusters in the so called anti glass phase of $\text{LiHo}_{0.045}\text{Y}_{0.955}\text{F}_4$.

Annealing Protocols

Since the compounds show in their spin glass like phase history dependent phenomena the path in temperature and transversal field space was crucial during all experiments. The terms and definitions of the annealing protocols are mentioned here in the introduction, because they will be used in the following discussions in various contexts. The different paths of the two annealing protocols are defined schematically in figure 4.11.

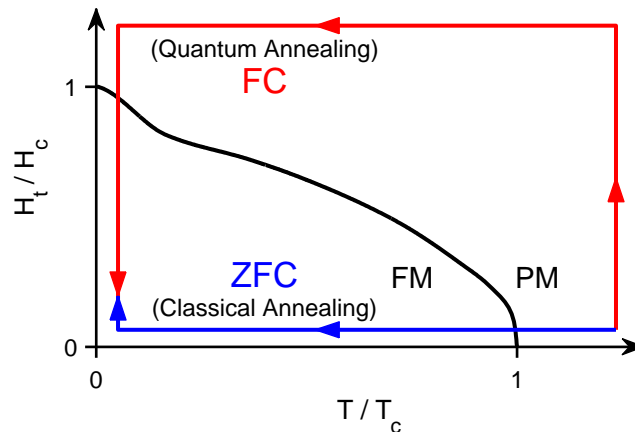


Figure 4.11: Two different annealing protocols shown in the phase diagram: field cooling (FC) and zero field cooling (ZFC)

4.2.1 Ising Ferromagnet, Random Field Magnet, Spin Glass

Phase Diagram

By replacing Holmium with nonmagnetic Yttrium the LiHo_xY_{1-x}F₄ compound evolves from an Ising ferromagnet towards a random field magnet and a spin glass like system. The phase diagram as a function of Holmium concentration x is depicted in figure 4.12. The critical temperatures determined by means of neutron scattering are in agreement with the susceptibility results [18]. Under light doping LiHo_xY_{1-x}F₄ remains ferromagnetically ordered but the Curie temperature is linearly suppressed $T_c(x) = x \cdot T_c(x = 1)$ as it would be expected from a meanfield calculation. Nevertheless, a recent classical Monte Carlo calculation [25] calls in question that the linear decrease in T_c has its origin in the mean field behavior of the system. The authors dispute that instead the phase diagram results from the combination of fluctuations and the effect of exchange coupling in the dipolar interaction dominated system. Below a marginal concentration around $x \approx 0.2$ ferromagnetic ordering is circumvented by the interplay of disorder and frustration arising from the anisotropy of dipolar interaction. Instead the system behaves as a spin glass. On further dilution the cross over temperature decreases to zero and for concentration around $x = 0.05$ there is no spin freezing at all. This phase is referred in literature as spin liquid “anti-glass” or “decoupled cluster glass”,

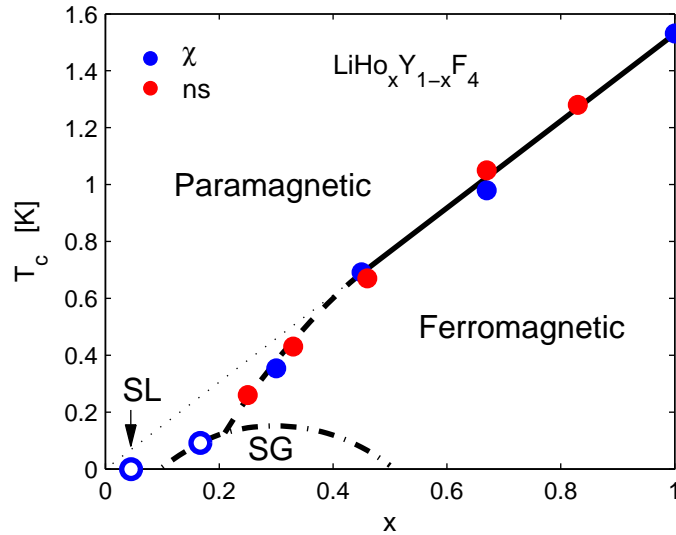


Figure 4.12: Phase diagram of LiHo_xY_{1-x}F₄. The measured T_c by means of neutron scattering is in accordance with the susceptibility data from [18].

according to its unusual behavior [7, 18, 8].

The temperature versus transverse field phase diagram of the different compounds investigated by means of diffraction are summarized in figure 4.13. From a mean-field point of view $H_c(x) = x \cdot H_c(x = 1)$ is expected. Normalizing the field and temperature in the phase diagram by the associated predicted meanfield values visualize the scaling of H_c and T_c . In contrast to T_c which is proportional to the dilution x , the critical transversal field $H_c(x)$ of the quantum critical point is suppressed faster than linear.

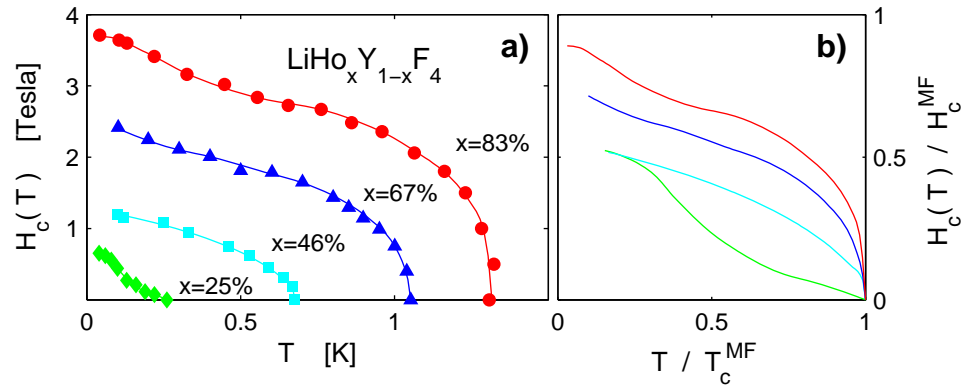


Figure 4.13: Summary of the transverse field versus temperature phase diagrams of the measured $\text{LiHo}_x\text{Y}_{1-x}\text{F}_4$ compounds (a). The curves are guides to the eye. In (b) the curves are normalized with the meanfield values $T_c^{\text{MF}} = x \cdot T_c(x = 1)$ and $H_c^{\text{MF}} = x \cdot H_c(x = 1)$. $T_c(x)$ is linear in x , whereas the critical fields are suppressed stronger than meanfield predicts.

$$x = 0.83$$

For this concentration the phenomenology is similar to the pure compound, resolution limited Bragg peaks indicates true long range ferromagnetic ordering below $T_c = (1.31 \pm 0.01)$ K. A critical transversal field of $H_c = (3.74 \pm 0.01)$ T was determined at a base temperature of around 50 mK. In figure 4.14 the measured integrated intensity as a function of field and temperature is shown.

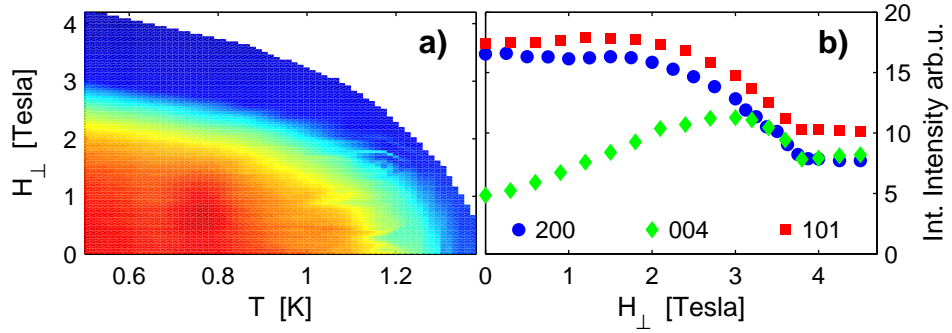


Figure 4.14: LiHo_xY_{1-x}F₄, $x = 83\%$. (a) Pseudocolormap visualizing the field and temperature dependence of the (200) Bragg peak. (b) Integrated intensity as function of applied transversal field. Each value was determined by means of a rocking curve through the selected magnetic Bragg peaks.

$x = 0.67$ - Emergence of Hysteretic Effects

Below the critical temperature of $T_c = (1.05 \pm 0.01)$ K ferromagnetic ordering appears and the critical transversal field is $H_c = (2.42 \pm 0.01)$ T, determined at base temperature of around 100 mK. The magnetic Bragg peaks appear resolution limited in the ordered phase for all tested annealing protocols, i.e. field cooled FC and zero field cooled ZFC. Although the Brillouin zone was effectively mapped out, no diffuse magnetic scattering signal was detected which would be an indication for the presence of short range correlations.

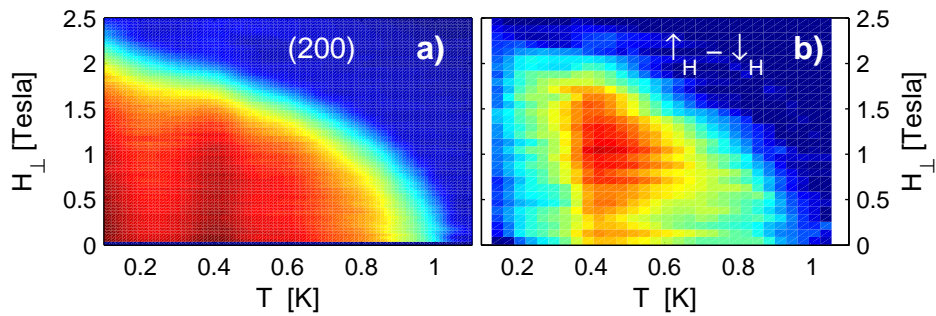


Figure 4.15: Pseudocolormaps visualizing the field and temperature dependence of the (200) Bragg peak intensity for LiHo_xY_{1-x}F₄, $x = 67\%$. (a) Absolute signal measured in sweeps in direction from low to high fields. (b) Difference from scans performed in increasing respectively decreasing field direction.

The system shows history dependent behavior. While sitting at the position of the magnetic Bragg peak at fixed temperature the field and ramping the field from zero to a value strictly above the critical field and back to zero again, then the final scattering intensity is decreased compared to its initial value, although the start and end position in the field-temperature diagram are identical. In figure 4.15 the field and temperature dependence of a magnetic Bragg peak is shown, the absolute value as well as the difference obtained by ramping the field either up or down. Beyond the phase boundary line the state of the system is independent from the annealing history. At intermediate temperatures of around 0.5 K the effect is maximal. Furthermore changing the polarity of the transversal field has a dramatic effect. In figure 4.16 a full hysteresis loop is depicted. The full scattering signal is recovered already at decent fields after crossing the zero point.

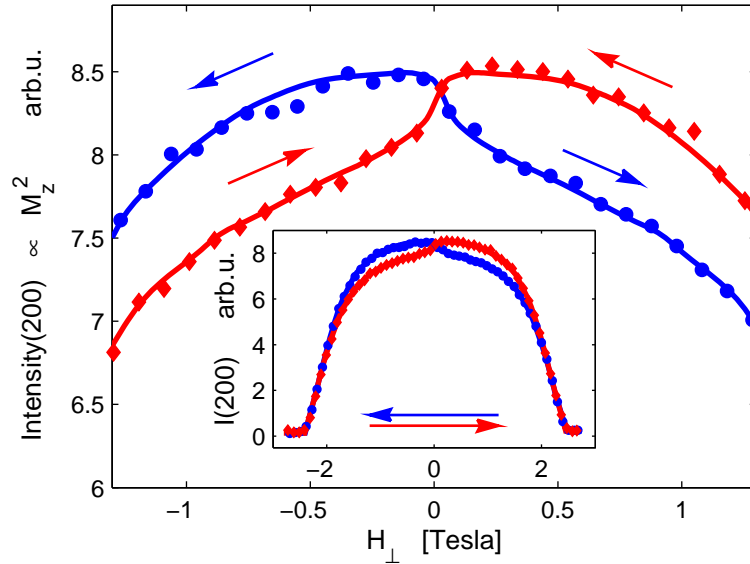


Figure 4.16: Hysteresis of the (200) Bragg peak intensity in $\text{LiHo}_x\text{Y}_{1-x}\text{F}_4$, $x = 67\%$ measured at $T = 120$ mK. In the inset the entire scans are shown. Changing the polarity of the field relive the full scattering signal.

As an interpretation one could argue by means of the longitudinal random field induced by the transversal field via off-diagonal dipolar interactions. At high transversal fields the random fields are large and preset the formation of the clusters. The spins tend to align along the direction predefined by the local random fields.

As the transversal field is switched off at low enough temperatures the system may remain partly trapped in the clustered structure. The barriers in the energy landscape are too large to overcome and to establish the more ho-

mogenous ordered ferromagnetic state as obtained by the first cooling down in zero applied field. By changing the polarity of the applied transversal field, the local longitudinal fields also switch in direction and therefore the potential landscape is inverted. Due to this provided activation energy, the system then is able to leave the trapped state and relax back to the optimal ground state as indicated by the increase in scattering intensity.

$$x = 0.25$$

The LiHo_xY_{1-x}F₄, $x = 0.25\%$ compound can be considered as a spin glass like system. The nature of the low temperature phase is associated with the cooling down procedure and the glassy state demonstrates history dependent behavior. Zero field cooling (ZFC) lead to long range ferromagnetic ordered state below $T_c = (237 \pm 5)$ mK, as indicated by the appearance of magnetic scattering in from of a sharp Bragg peak. At base temperature of $T = 40$ mK a critical transversal field of $H_c = (0.61 \pm 0.01)$ T was determined. On the contrary if the system was cooled down in a field $H > H_c$ before the field was set to zero again, i.e. field cooled (FC), there is no magnetic contribution to the Bragg peaks. The same state results by ramping up the field above H_c and down again, even if the compound was previously ZFC annealed. The Bragg peak intensity obtained in a measurement according to the FC and ZFC protocol respectively is shown in figure 4.17. Furthermore the field and temperature dependence of the signal in the ZFC phase indicates the phase diagram. As far as investigated in the present experiment the history dependent behavior range over the entire temperature region up to T_c in contrast to the less diluted compounds like LiHo_xY_{1-x}F₄, $x \approx 45\%$, which resembles in its phase diagram a reentrant spin glass.

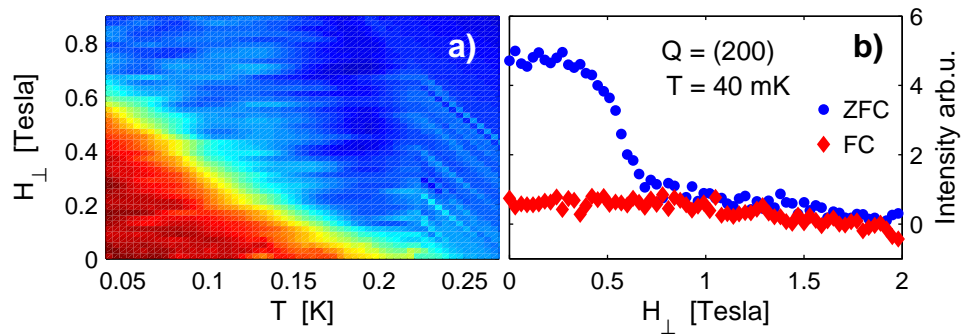


Figure 4.17: LiHo_xY_{1-x}F₄, $x = 25\%$. (a) Pseudocolormap visualizing the field and temperature dependence of the (200) Bragg peak intensity measured in the state obtained via zero field cooling. (b) Difference between field cooling (FC) and zero field cooling protocols.

In the FC state the magnetic scattering intensity has a broad distribution in reciprocal space. In the short scans across the Bragg peak position this becomes manifest effectively only in form of a decent changing background. A further characterization of the magnetic scattering in terms of shape and width in reciprocal space was experimentally impracticable, due to the unfavorable signal to noise ratio.

$x = 0.20$ - The Marginal Concentration

In early investigations of $\text{LiHo}_x\text{Y}_{1-x}\text{F}_4$ the focus of interest was on one side in the less diluted compounds around $x = 0.5$ or on the other hand on the very diluted. The concentration around $x = 20\%$ is marginal since this is the region in the phase diagram, where the line $T_c(x)$ hits the dome of the spin glass phase. Recently an investigation of the phase diagram in $\text{LiHo}_x\text{Y}_{(1-x)}\text{F}_4$, $x = 19.8\%$ by means of AC-susceptibility [45] has been reported. The authors discussed the crossover from random field dominated behavior in the 19.8% sample to entanglement dominated behavior in the 16.7% sample. One possibility to define the transition to a spin glass is the emergence of a flat spectral response at low frequency ω in χ'' , which corresponds to a logarithmic divergence in $\chi' \sim \log(\omega/\omega_0)$. In the region above the spin glass transition, the authors fitted the low frequency tail $\chi''(\omega)$ to a power law form, ω^α . The critical field for the transition $T_g(H_t)$ is defined as $\alpha \rightarrow 0$. In their interpretation the characteristic frequency ω_0 is related to the fastest relaxation process available to the system and characterizes the quantum tunneling rate. They have shown that the dynamically-determined phase boundary coincides with that derived from the maxima of the nonlinear susceptibility coefficient χ_3 [45]. Since the susceptibility provides as a bulk technique only indirect information about the system, the microscopic picture remained an open issue.

The main outcome from the here presented neutron experiment is that there is no long range ordered state down to 40 mK. Rocking curves through the ferromagnetic Bragg peak (200) has been performed as function of field and temperature. No change in the integrated intensity was found, and therefore there is no magnetic contribution to the Bragg peaks. Nevertheless, the field scans with higher statistic while sitting in center of the Bragg peak instead of performing ω -scans, show a weak field dependence of the signal. But it has to take into account that the background as well may change with field. In scans over an extended range in reciprocal space, i.e. extended over the range of more than half of a Brillouin zone, a broad magnetic signal around the position of the ferromagnetic Bragg peak (200) has been found. To map out the field and temperature dependence of these short range correlations scans sitting slightly off the Bragg peak has been performed (figure 4.18). There is no indication of a phase transition at any field up to 3 T and down to

40 mK in contradiction to the suggestions from the dynamical susceptibility measurements. Instead of a sharp transition the change in signal is cross over like. In particular the temperature dependence can be fitted in good approximation to a T^α power law. This clearly marks a difference to the only slightly higher doped $x = 0.25$ compound with its sharp transition, see figure 4.18.

Since it was known from former experiments on less diluted compounds that hysteresis effects could play a role, taking care to follow a strict annealing protocol was indicated. Each scan has been done first in a ZFC way at increasing field, then again decreasing after the field was risen to a high enough field value of 3 T to get in the state which is regarded as equivalent to a FC one. To judge if there is an hysteresis or not in the $x = 20\%$ compounds is not as obvious as in the less diluted compounds. Remarkably the difference at base temperature is less pronounced than at intermediate temperature > 100 mK. But the fact that the up and down ramping curves do not coincide exactly, could also be explained by magneto caloric effect. Considering the temperature scan it is reasonable that the difference in the scattered signal could originate from a slight shift in temperature.

How the peak shape of the magnetic scattering signal evolves as a function of field was elucidated in a series of high statistic reciprocal space scans (figure 4.19). Also here FC and ZFC protocols turned out to be equivalent. The data was fitted with a Lorentzian model folded with the experimental resolution in form of a gaussian. As a function of field the intrinsic line increases but the integrated intensity remains constant. At $H = 0$ T the system is indeed dominated by magnetic correlations ranging only over a short distance in the order of a few unit cells.

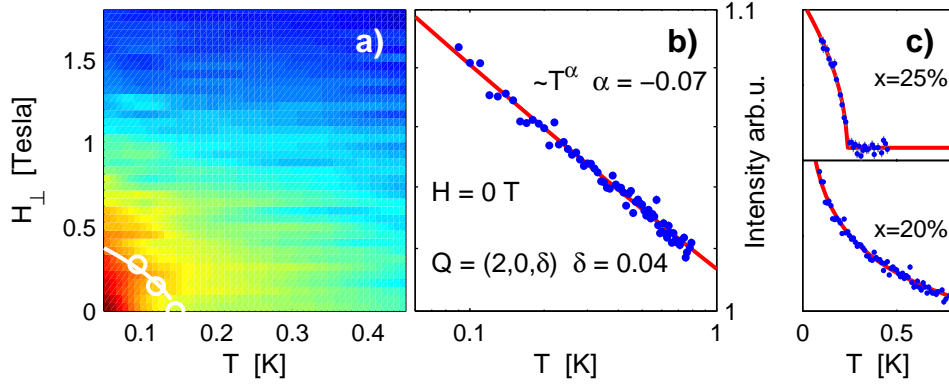


Figure 4.18: $\text{LiHo}_x\text{Y}_{1-x}\text{F}_4$, $x = 20\%$. (a) Pseudocolormaps visualizing the field and temperature dependence of the intensity measured slightly off the Bragg peak at $Q = (2, 0, \delta)$. The white dots represent the results from susceptibility measurements [45]. (b) The measured neutron scattering intensity shows a power law like temperature dependence, in contrast to the sharp transition found in $\text{LiHo}_x\text{Y}_{1-x}\text{F}_4$, $x = 25\%$

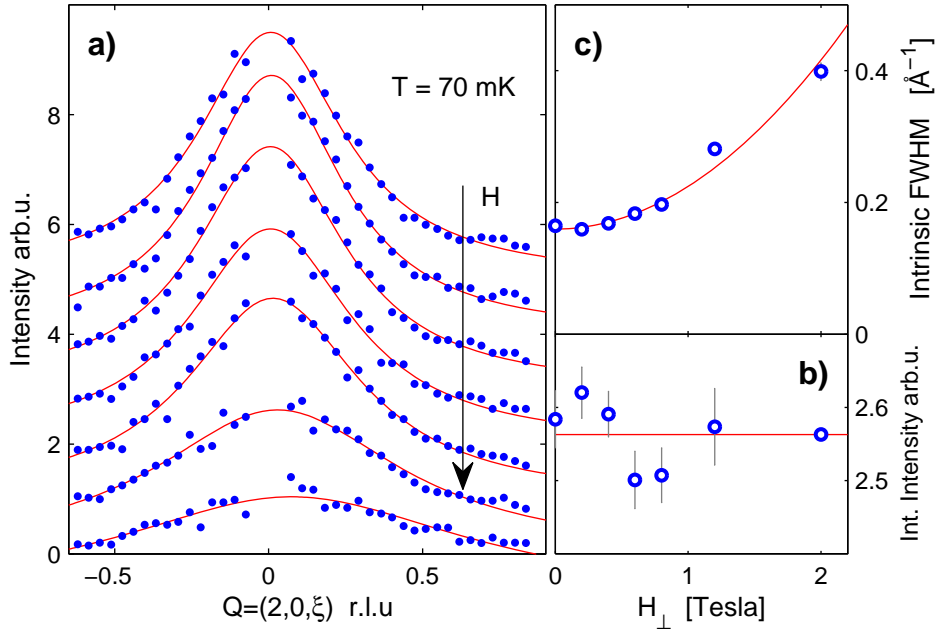


Figure 4.19: $\text{LiHo}_x\text{Y}_{1-x}\text{F}_4$, $x = 20\%$ field dependence of the short range magnetic correlations (a). The width is increasing with field (b), whereas the integrated intensity remains almost constant (c).

4.2.2 LiHo_xY_{1-x}F₄, $x = 1/3 - 1/2$

The phase diagram and magnetic correlations in LiHo_xY_{1-x}F₄, $x = 0.46$ and $x = 0.33$ have been investigated on the 2-axis neutron diffractometer E4 at HMI and at the three-axis spectrometer 4F-2 at LLB Saclay. As configuration in each case the a-axis of the crystal as well as the magnetic field directions have been chosen perpendicular to the scattering plane. For LiHo_xY_{1-x}F₄, $x = 0.33$ the history dependent effects have even more pronounced signature in neutron scattering as in the case of $x = 0.46$, as it will be shown in the next paragraphs. But the experiments have been performed first on the basis of $x = 0.46$ and this is the reason why the majority of the here presented data was available for this concentration. Furthermore, the similarity of our $x = 0.46$ with the $x = 0.44$ compound widely investigated by means of ac-susceptibility in T. F. Rosenbaums group in Chicago [6, 5, 27] is supposed in the following discussion. There is no significant change in the phase diagram around this concentration and from an experimental point of view only nominal values for the exact concentration are known anyway.

Re-Entrant Spin Glass

In LiHo_xY_{1-x}F₄, $x = 0.46$ long range ferromagnetic ordering appears below the critical temperature of $T_c = (0.675 \pm 0.005)$ K. By applying a transversal field, the system undergoes a quantum phase transition, whereas a critical field of $H_c = (1.21 \pm 0.01)$ T was measured at a temperature of 30 mK. The critical exponents β for both regions has been exterminated from the onset of the magnetic Bragg peak intensity (figure 4.20). The critical scattering strongly contributes to the neutron scattering signal and was subtracted in the final analysis. A question of interest is whether or not dilution may affect the critical behavior. Famous examples are so called Griffith singularities [46]. These anomalies in the magnetization are theoretically expected in randomly diluted ferromagnetic Ising systems below the critical temperature of the pure compound. An experimental indication of such an effect in LiHo_xY_{1-x}F₄, $x = 0.44$ was reported recently [27]. Nevertheless, the critical exponents β determined from the neutron data are identical for the diluted and pure compounds. For the quantum phase transition $\beta_H = 0.47 \pm 0.02$ is close to the meanfield exponent $\beta_{MF} = 0.5$, whereas $\beta_T = 0.32 \pm 0.02$ for the thermal phase transition at T_c is lower and corresponds to the renormalization group result $\beta_{RG} = 1/3$ for the 3D-Ising model.

Below temperatures of around 250 mK there is a crossover to a phase with history dependent behavior depending on a chosen annealing protocol. By entering this phase from the high field state above H_c the magnetic scattering signal appears in form of a broad Lorentzian-like peak shape instead of a resolution limited gaussian. This is the signature of short range corre-

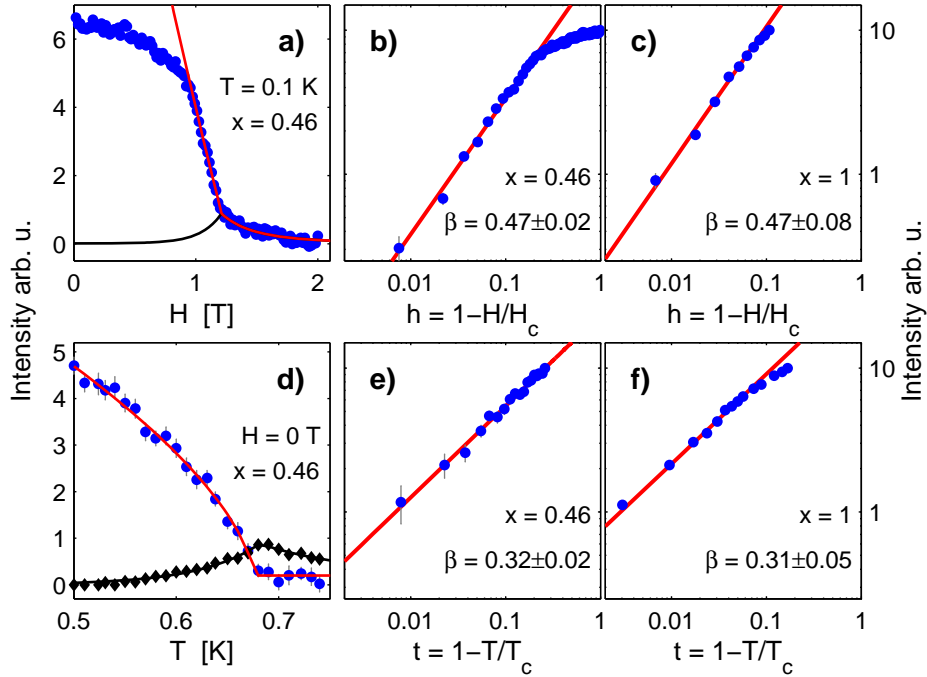


Figure 4.20: Intensity of the magnetic Bragg peak (200) around the phase transition in $\text{LiHo}_x\text{Y}_{1-x}\text{F}_4$, $x = 0.46$ compared with $x = 1$. The signal originating from critical scattering is indicated by the black curve in (a,d) and was subtracted for the further analysis (b,c,e,f). The critical exponents β of the magnetization in the diluted and pure compound are identical.

lated states instead of a long range ordered phase. This low temperature phase characterized by lack of true ordering and history dependent behavior can therefore be regarded as spin glass like state. The phase diagram of $\text{LiHo}_{0.46}\text{Y}_{0.54}\text{F}_4$ therefore resembles that of a 'Reentrant Spin Glass', see figure 4.21.

The phase boundary was determined by means of field scans at a fixed $Q = (2, 0, 0.04)$ slightly off the magnetic Bragg peak position as indicated in figure 4.21 d). Experimentally this was achieved by rotating the crystal by 0.6° and keeping the scattering angle fixed. Since the signal is broad compare to the instrumental resolution almost the full amplitude of the diffuse magnetic scattering is measurable without any significant contribution from nuclear Bragg scattering. In this particular measurement the spin

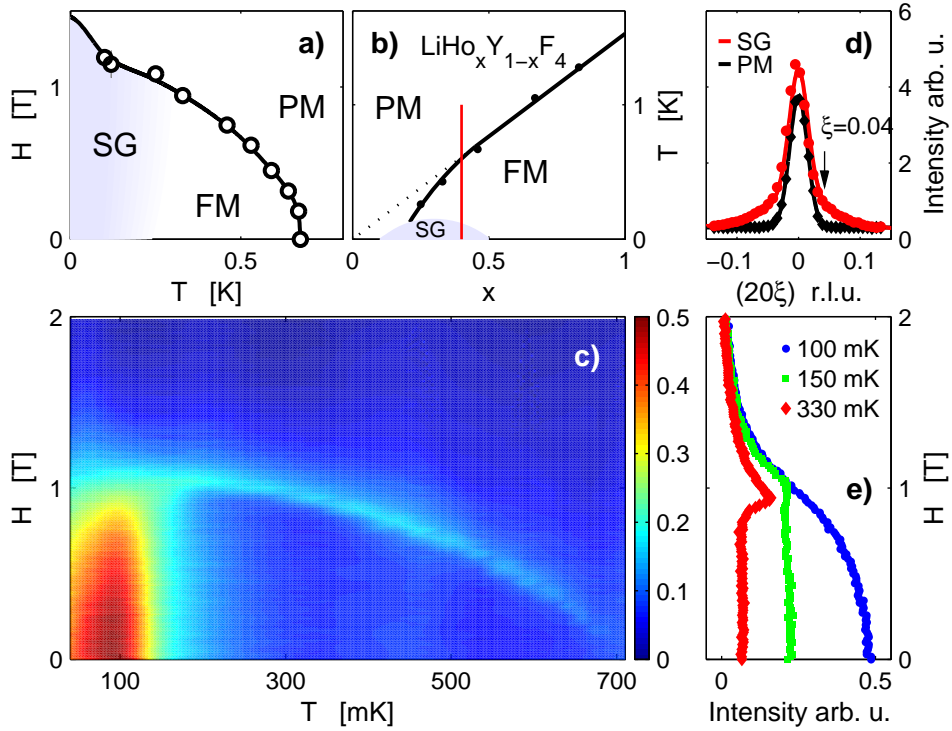


Figure 4.21: The phase diagram of LiHo_{0.46}Y_{0.54}F₄ resembles that of a reentrant Spin Glass (a,b). The field and temperature dependent intensity of the diffuse magnetic scattering (c) was measured via field scans (e) at fixed $Q = (2, 0, 0.04)$ slightly off the magnetic Bragg peak (d). This highlights the spin glass region as well as the ferromagnetic phase boundary via critical scattering.

glass phase is mapped out. Because of the appearance of critical scattering, which manifests itself by a broad diffuse scattering around the Bragg peak, this method is not only sensitive to detect the spin glass region but also the frontier between paramagnetic and long range ordered ferromagnetic phases (figure 4.21 c).

LiHo_xY_{1-x}F₄, $x = 0.33$ is in its behavior, to our current understanding, comparable to the $x = 0.46$ compound. The determined critical temperature is $T_c = (0.430 \pm 0.005)$ K and the critical field measured at 50 mK is $H_c = (0.844 \pm 0.004)$ T.

Magnetic Correlations and Critical Scattering

To further elucidate the fine structure in the momentum dependence of the magnetic correlations the diffuse scattering was mapped out in reciprocal space over the entire Brillouin zone (figure 4.22). For this purpose the required Q-resolution and a proper signal to noise ratio could only be achieved in a three-axis experiment, although already in the diffraction data the characteristic anisotropy was indicated. The measurement was performed close to the critical region at $H = 1$ T and a nominal temperature of $T = 180$ mK. The diffuse magnetic signal considered here is therefore the critical scattering outside the spin glass phase, but nevertheless the peak shape deep in the spin glass region is identical as far as investigated.

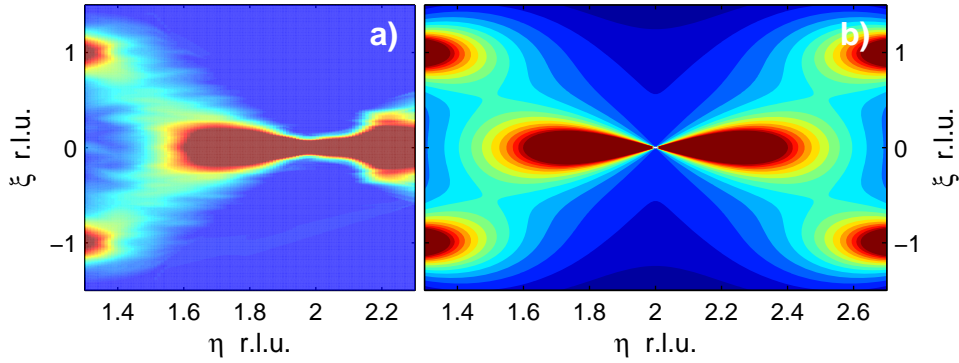


Figure 4.22: Magnetic scattering intensity distribution in reciprocal space plane $Q = (\eta, 0, \zeta)$ in $\text{LiHo}_{0.46}\text{Y}_{0.54}\text{F}_4$. (a) Pseudocolor map from measured intensities at $H = 1$ T and $T = 180$ mK. The data was symmetrized around the $Q = (\eta, 0, 0)$ mirroraxis. (b) Calculated correlation function using the parameters estimated from the data.

The constant intensity contour of the magnetic diffuse scattering has in reciprocal space a characteristic "butterfly" or "bow-tie" shape with a pinch along the crystallographic c-axis, i.e. the Ising axis. In real space this corresponds to clusters of parallel aligned spins. These clusters are extended along the c-axis, where the dipolar interaction is ferromagnetic, and they are shrunken towards the middle in transversal direction due to the antiferromagnetic in-plane coupling.

The cross-section for scattering from an Ising system in the quasielastic limit can be described with the following formulas [47].

$$\frac{d\sigma}{d\Omega} \propto \left(1 - \frac{Q_z^2}{Q_2^2}\right) \cdot f^2(\mathbf{Q}) \frac{\chi(\mathbf{Q}, T)}{\chi^0(T)}. \quad (4.2.1)$$

Here f denotes the magnetic formfactor for Ho³⁺ and $\chi^0(T)$ the single ion susceptibility of the system. In the simple meanfield expression the wave vector dependent susceptibility is given by the correlation length ξ in plane perpendicular to the Ising axis and a parameter describing the anisotropy.

$$\frac{1}{\chi(\mathbf{Q}, T)} \propto 1 + \xi^2 \left(q^2 + g \frac{q_z^2}{q^2} \right), \quad (4.2.2)$$

Here $\mathbf{q} = \mathbf{Q} - \tau^*$ is the momentum vector reduced by the reciprocal space vector τ^* according to the ordering. Expression 4.2.2 is characteristic for dipolar coupled uniaxial systems, as pointed out by Aharony [48]. This model was previously applied to describe the diffuse scattering in the spin glass compound LiHo_{0.167}Y_{0.833}F₄ [18] and the critical scattering in the ferromagnet LiTbF₄ [49]. The parameter g reflects the different effective correlation length in plane ξ and along the Ising axis ξ_{\parallel} . The latter can be defined as the inverse of the maximal half width half maximum along the c -axis, i.e. the lateral extension of the butterfly shaped half height contour. It then follows from expression 4.2.2 formally $\xi_{\parallel} = \frac{1}{2} g^{1/2} \xi^2$. The anisotropy can be explained as follows. Because the in plane dipolar interaction is antiferromagnetic, the in plane ferromagnetic correlations are only indirect, i.e. they are mediated through neighboring out-of-plane spins. For a diluted compound therefore an increase in g is expected.

The neutron scattering data, elastic scans in transversal and longitudinal directions, are fitted using the previously described model, see figure 4.23. A consistent parameter set ξ and g was determined. The correlation length of $\xi = (121 \pm 4) \text{ \AA}$ reflects that the system was measured close to the phase transition. More relevant is the anisotropy parameter $g = (1.34 \pm 0.33) \text{ \AA}^{-2}$, because it is supposed that its value can be considered as constant over a large temperature and field range and has a characteristic value for the particular compound. The experimentally determined g is reasonable if one considers the typical values reported in literature. In LiTbF₄ experimentally $g = (1.3 \pm 0.1) \text{ \AA}^{-2}$ was found close to T_c , whereas the theoretically expected high-temperature meanfield value is $g = 1.56 \text{ \AA}^{-2}$ [49]. For the spin glass compound LiHo_{0.167}Y_{0.833}F₄ the anisotropy is slightly enhanced with $g = (2.0 \pm 0.2) \text{ \AA}^{-2}$ [18].

Quantum Annealing - Susceptibility Results

In an Ising spin glass a preparation of the system in a minimal energy configuration can be achieved by adiabatically lowering of the temperature. The optimization process driven by thermal fluctuations, is the so called classical annealing (CA). In the experiment with LiHo_xY_{1-x}F₄ the CA protocol corresponds to cooling down the compound in zero applied

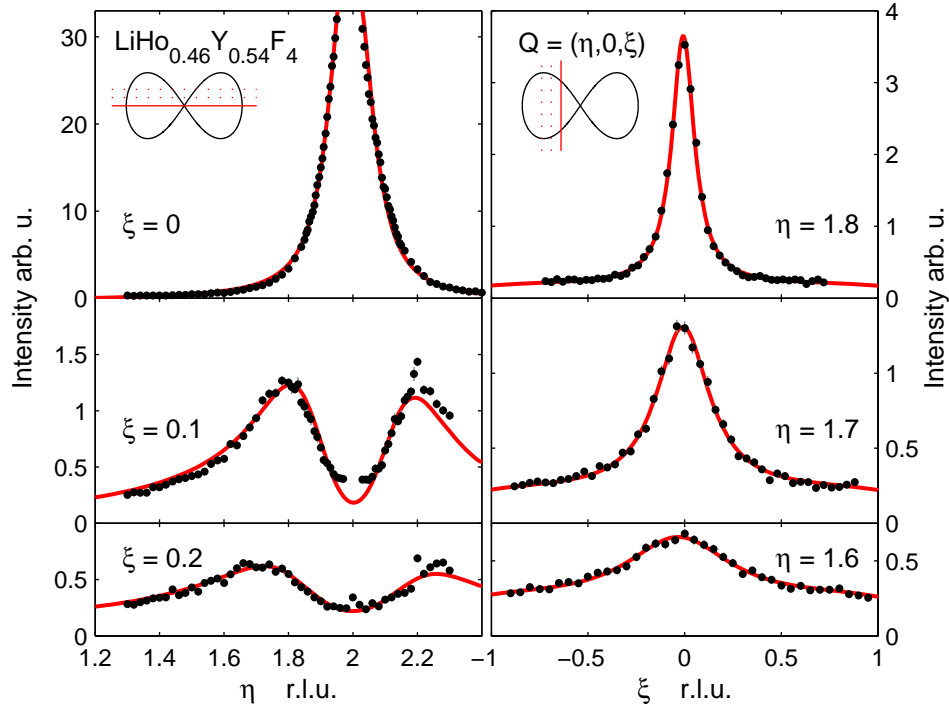


Figure 4.23: Neutron scattering intensities as function of momentum Q . The trajectories in reciprocal space for the transversal and longitudinal elastic scans are illustrated in the insets. The red lines correspond to fits according to the model described in the text.

field (ZFC). But in the transversal field Ising model the transversal field term induces a relaxation path by quantum mechanical tunneling effect. The field cooling protocol (FC), i.e. cooling down the compound in a high transversal field above H_c and adiabatically ramping down the field once the base temperature is reached, is referred as quantum annealing. The compound $\text{LiHo}_x\text{Y}_{1-x}\text{F}_4$, $x=0.44$, therefore allows to realize an experimental comparison of quantum annealing versus classical annealing.

Brooke et al. [6] have used ac-susceptibility spectroscopy to probe the relaxation times for spin reorientation in the glass phase depending on the annealing path chosen (figure 4.24). In the high-temperature paramagnetic and the high-field quantum-paramagnetic phase the data coincide. But once entering the spin glass regime both spectra deviate, in the QA case there is more spectral weight towards higher frequencies. On the low frequency side there is a logarithmic divergence $\chi'(f) = C \log(f/f_0)$, where C is a constant. The states prepared via quantum and classical cooling respectively show different characteristic frequencies f_0 . Quantum cooling

yield to a state for which relaxation times are up to a factor of 30 faster than those produced by classical cooling. The interpretation was that quantum tunneling is more effective than thermal fluctuations to explore the configuration space, hence quantum annealing forces the convergence to the optimum ground state [6].

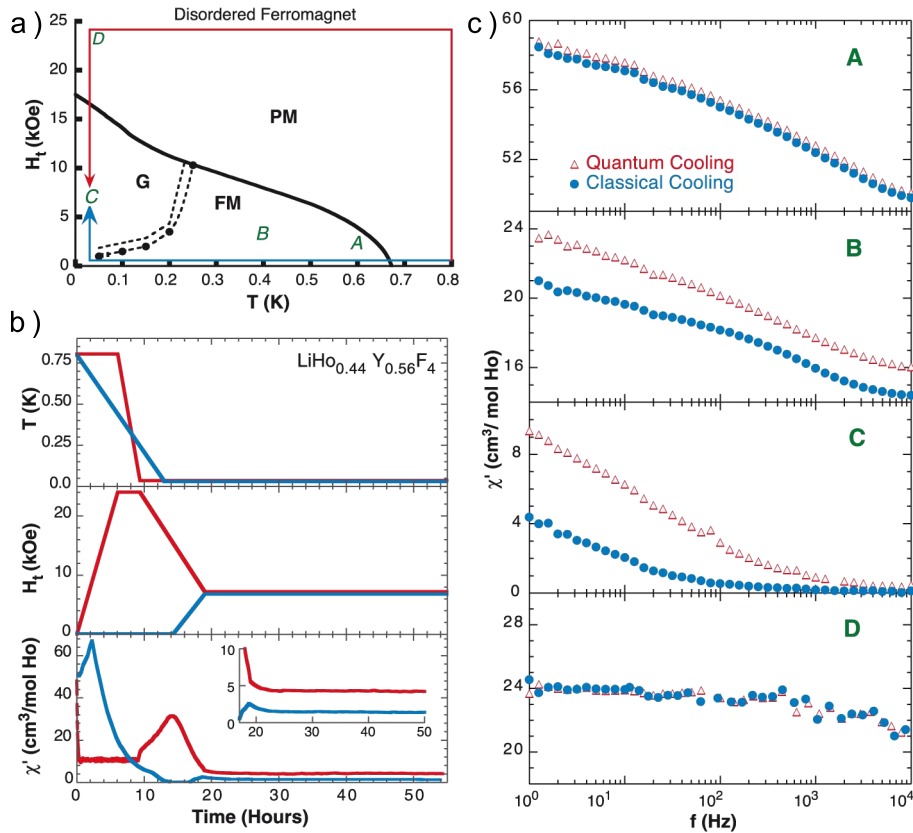


Figure 4.24: Ac-susceptibility spectroscopy of $\text{LiHo}_{0.44}\text{Y}_{0.56}\text{F}_4$ at the points A to D, indicated in (a), for both quantum and classical annealing protocol as reported in [6]. The cooling history previous to the measurements is shown in panel (b). Although the spectra begin together (A) in the classical ferromagnet, they start to diverge as temperature is lowered (B), until deep in the glassy phase (C) they exhibit widely different time scales and an unusual logarithmic dependence on frequency f . Crossing back into the quantum paramagnet (D) restores independence to the annealing history.

Quantum Annealing - Neutron Diffraction Results

By means of neutron diffraction the evolution of the magnetic correlation along the two different cooling protocols (fig. 4.11) was investigated in $\text{LiHo}_x\text{Y}_{1-x}\text{F}_4$, $x = 0.46$ and $x = 0.33$. Below the cross over temperature to the spin glass region in the phase diagram, the system either persists in the long range ordered state in the case of a zero field cooling path (ZFC) or evolves to a phase with glass like behavior in the case of cooling in an applied transversal field (FC). The two different phases become manifest in a narrow, resolution limited gaussian (ZFC), respectively a broad Lorentzian-like peak shape (FC) in the magnetic scattering signal (fig. 4.25). This reflects either true long range or short range ordering, respectively correlations. In the more diluted compound $x = 0.33$ the width is enhanced compare to $x = 0.46$, i.e. the correlation length decreases as a function of concentration.

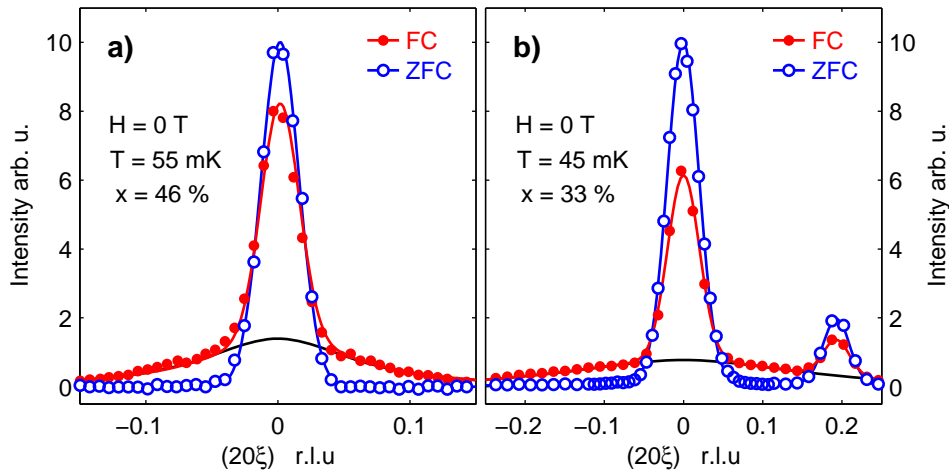


Figure 4.25: Scans through the Bragg peak (200) in the low temperature spin glass phase of $\text{LiHo}_x\text{Y}_{1-x}\text{F}_4$, $x=0.33$ and $x=0.46$, as a result of the field cooling respectively zero field cooling annealing path. The curves represent fits to a Gaussian-Lorentzian model as indicated in the text. The black curve is the magnetic only FC intensity, i.e. the nuclear scattering contribution is subtracted. The second peak in (b) originates from a misaligned grain of the multi crystal sample.

Rising the transversal field above H_c , the system enters the quantum paramagnetic phase where no difference between the two annealing protocols exists and the history dependence is canceled, as it was also reported from the susceptibility experiments [6]. Cooling in zero field then increasing the field above the critical field leads to the identical state as cooling down in the same field. Lowering the field later on again to zero the system always

ended up in the spin glass state with the Lorentzian-like peak shape, even if the system was prepared by zero field cooling before. The question was also if the short range correlated state prepared by field cooling show any relaxation towards the long range ordered state. Even over time spans of up to a day there was no significant change observable. The disordered correlated state is quasi stable and turned out to be fully reproducible in all the independent attempts during the experiment.

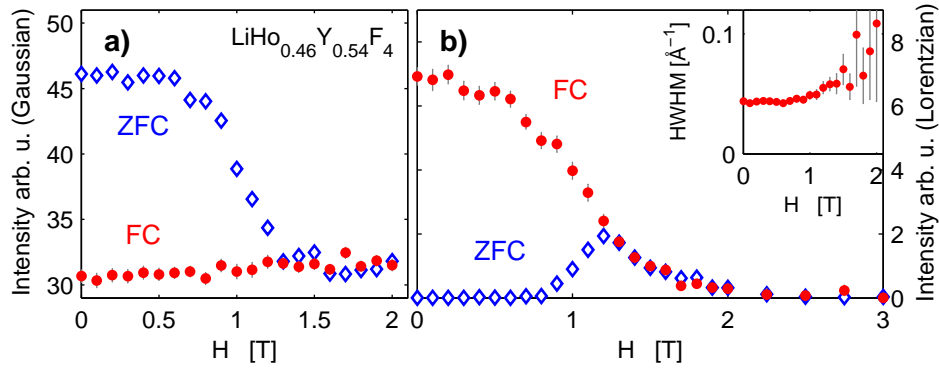


Figure 4.26: Magnetic correlations as a function of transversal field measured at $T = 55$ mK, for field cooling (FC) and zero-field cooling (ZFC). (a) Gaussian, (b) Lorentzian contribution determined from the determined from the fits to the neutron scans performed transversal through $Q = (200)$.

The evolution of the magnetic correlations and order parameter as a function of transversal field at base temperature is shown in figure 4.26 and 4.27, for $x = 0.46$ and $x = 0.33$, respectively. The transversal scans through $Q = (200)$ at each field point was extended in reciprocal space such that the diffuse part as well as the Bragg scattering was covered. As a model to fit the data a Gaussian plus a Lorentzian, folded by a gaussian corresponding to the finite instrumental resolution, is considered. An example is depicted in figure 4.25. In the ZFC case, starting deep in the glassy phase at $H = 0$ T, the Lorentzian part is zero and all the magnetic scattering is concentrated in the magnetic Bragg peak. By rising the transversal field the intensity of the gaussian decreases and vanishes at H_c . The Lorentzian part first remains zero, then increases rapidly and reaches its maximum at the critical field before vanishing again in the high field limit. This is exactly the signature as one would expect in the ferromagnetic phase, a power law in Bragg peak intensity, i.e. the order parameter at QPT accompanied by critical scattering. For the FC path, starting in the quantum paramagnetic high field phase, the diffuse magnetic scattering signal continuously increases as the field is reduced and reaches its maximum at $H = 0$ T. On the other hand the gaussian part remains constant over the whole range and is only con-

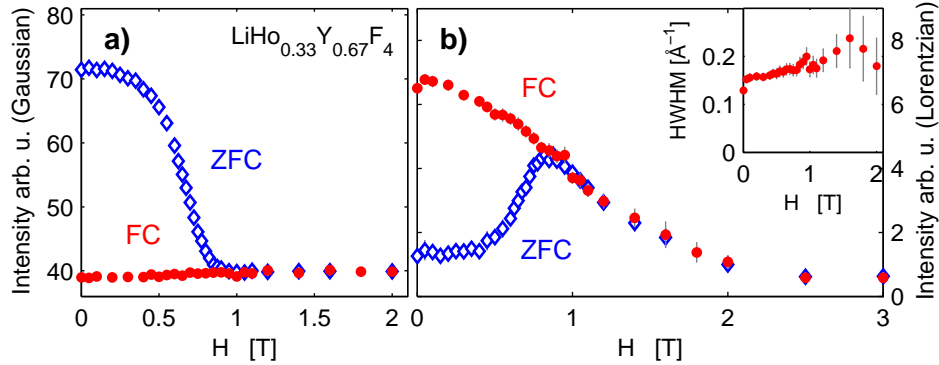


Figure 4.27: Magnetic correlations as a function of transversal field measured at $T = 50$ mK, for field cooling (FC) and zero-field cooling (ZFC). (a) Gaussian, (b) Lorentzian contribution determined from the fits to the neutron scans performed transversal through $Q = (200)$.

taining the contribution from the nuclear Bragg scattering. Remarkably the full magnetic intensity appears in form of diffuse scattering, no long range order at all can be established. In the inset of the figures 4.26 and 4.27 also the intrinsic width of the Lorentzian contribution for SG phase is indicated as a function of field. The width is slightly increasing with field reflecting that the length scale over which the spins are correlated is further reduced. But one has to mention that the determined length can not be converted directly to the correlation length, a certain proportionality constant has to be considered. This related to the way how the data was collected, the area detector of the E4-diffractometer integrates over a large window of the 2θ scattering angle. A readout of the particular pixel was made in several attempt to the data analysis. Nevertheless it does not lead to a further improvement because then also the intensity is reduced and the bad signal to noise ratio matters as well as the poor instrumental resolution. As shown in the previous paragraph the magnetic correlation has a butterfly like peak shape in reciprocal space. To fit the true correlation length this fine structure should be clearly resolved by the instrument. Therefore due to the available data quality the analysis of the 2θ -integrated signal with a generic Lorentzian model must be regarded as more trustworthily and meaningful.

Inelastic neutron spectroscopy instead of diffraction may provide further evidence in the difference of the two annealing protocols. The spectra of both cases FC as well as ZFC, measured at a temperature of around 200 mK and different field values close to the critical field $H_c(T) = 1$ T, are shown in figure 4.28. Below H_c at $H = 0.8$ T the inelastic intensity at zone center is doubled for the FC annealed system compared to the ZFC. But at

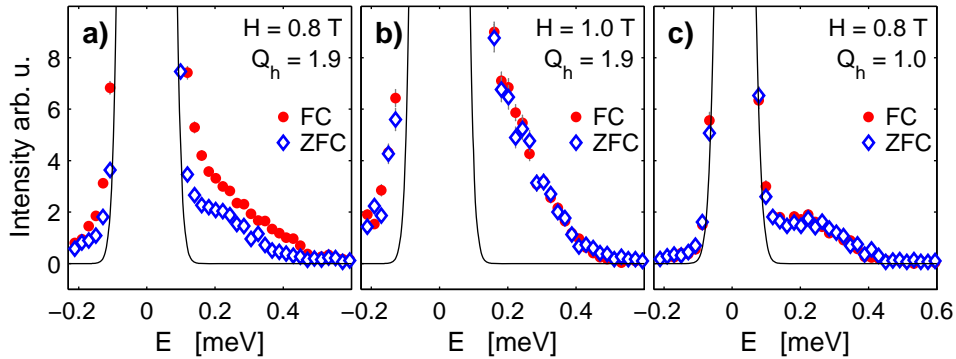


Figure 4.28: Spectra of LiHo_{0.46}Y_{0.54}F₄ measured below and at critical field for field cooled and zero field cooled annealing protocol. At zone center (a) the inelastic intensity is enhanced in the FC spin glass state, whereas at zone boundary there is no difference (c). In the quantum paramagnetic phase there spectra does not depend on the annealing protocol (b).

and above the critical field the spectra of both protocol coincides with each other. Remarkably the effect is only present at zone center, whereas at zone boundary there is no difference visible in the spectra at any field as far as considered.

Conclusions

Based only on the neutron scattering data one would conclude that the ZFC annealing path is more efficient than FC to prepare the system in the energetically optimal state, since the long range ordered ferromagnetic state is considered as the true ground state. Conversely via field cooling the system gets trapped in a non-equilibrium steady state, a side minima of the manifold energy landscape. This is exactly the contradiction to the conclusion drawn from the susceptibility data [6]. How can this discrepancy be solved? From the available information a definitive judgement is not appropriate and a further understanding is required to assemble all the aspect to obtain a consistent theoretical picture of the system.

First of all possible systematic sources that may cause a different result should be ruled out. One might be the timescale of the annealing protocol. Obviously in a large scale facility experiment it is not possible to achieve this with the same meticulousness as in the laboratory, it is a simple matter of available beam time. In the neutron experiment the consistency of the data recorded over days was checked carefully and there is no evidence that transient behavior is the source of the discrepancy. Nevertheless the

way of ruling out this systematic uncertainties would be to combine both experiments in an insitu neutron scattering ac-susceptibility experiment.

The common sense in the general discussion of quantum annealing is that this method is more efficient than the classical annealing [50]. There is various theoretical activity on this topic, in the investigation of toy-models, in particular the transverse field Ising model [51], for example using monte-carlo methods. But with regards to interpret the experimental findings in $\text{LiHo}_x\text{Y}_{1-x}\text{F}_4$ one should be aware that the system is oversimplified by the transverse field Ising model. This neglected complexity may be a crucial point. At least to interpret the neutron scattering data, here the following mechanism is suggested, similar to that proposed to explain the hysteresis effect in $\text{LiHo}_x\text{Y}_{1-x}\text{F}_4$, $x = 0.67$. The random longitudinal fields induced via diagonal dipolar coupling are proportional to the transversal field. By following the field cooling path this local random potential predefines the preferred alignment of the spins to clusters as the system enters the glassy state. Switching of the field, the system is not able to establish the homogenous ordered ferromagnetic ground state out of this previously formed trapped state where ordering or correlation is limited over the dimensions of certain clusters. The presence of longitudinal random field outperforms the quantum annealing process by cluster formation. On the other hand cooling down along the zero field route there are initially no random fields, because no symmetry is broken [10]. Therefore the system persists in the ferromagnetic state until the order will be destroyed by a field risen above its critical value.

4.2.3 LiHo_xY_{1-x}F₄, $x = 0.045$

The probably most exotic and one of least understood phenomena in LiHo_xY_{1-x}F₄ is the "anti-glass" state. In the following the term is explained and a short reference to the susceptibility investigation of coherent spin oscillations is given. Then the results from the time resolved small angle neutron scattering experiment with insitu ac-susceptibility investigation are presented. The appeal of the system are oscillating clusters with long lifetimes and addressable by frequency, hence it is supporting the vision to realize fourier indexed Qbits.

The Anti-Glass

In the very diluted limit of LiHo_xY_{1-x}F₄ around $x = 0.045$ there is no freezing to a spin glass down to the lowest temperatures experimentally accessible. Instead the system condensed in a spin liquid like state often referred as "Decoupled Cluster Glass" [52, 18] or "Anti-Glass" [8]. The term anti-glass is motivated by the characteristic spectral behavior which is contrary to that approved for common spin glasses.

In the case of a true spin glass, for example LiHo_{0.167}Y_{0.833}F₄, the spectral response $\chi''(f)$ is shifted towards lower frequencies and broadens as the temperature is lowered. This is related figuratively to a growing of the barriers in the energy landscape and a slowing down of the relaxation. Formally an exponential relaxation $\exp(-t/\tau)$ with a relaxation time τ is assumed, corresponding to the so called Debye form for χ in frequency space (paragraph 2.4). The spin glass system is characterized by a distribution of different relaxation times and the total response is finally obtained by superposition principle. The spectral change as a function of temperature is therefore obvious considering the way how the distribution is affected.

In contrast to the spectral behavior in glasses, in the case of LiHo_{0.045}Y_{0.955}F₄ the ac-susceptibility spectra sharpen with decreasing temperatures and is gapped on the low frequency side (figure 4.29). As model for the system a superposition of oscillators is proposed instead of relaxation dynamics with distribution of relaxation times [18, 8].

Recently a group from Waterloo (Ca) reported new susceptibility and specific heat investigations on various LiHo_xY_{1-x}F₄ compounds, also for $x = 0.045$, [53, 54]. Therein, the existence of the anti-glass and the widely referred experimental results from the Chicago group [52, 8, 7] are questioned and instead they found as contradiction common spin glass behavior. However it is not clear which of the two reports are more trustworthy and what the experimental subtleties are. A final judgement requires a further independent investigation.

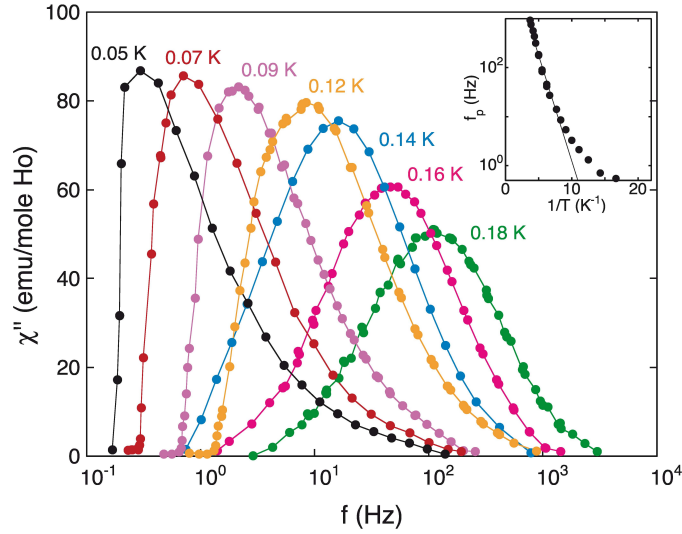


Figure 4.29: Susceptibility spectra of $\text{LiHo}_{0.045}\text{Y}_{0.955}\text{F}_4$ anti-glass at different temperatures [8]. The line width decreases with temperature and the spectra becomes gapped in the low temperature limit. The inset shows the deviation from classical Arrhenius behavior for the peak frequency.

Coherent Oscillations of Spin Clusters

The anti-glass state forms the host of probably one of the most exciting phenomena so far reported in the LiReF_4 compounds: In dilute $\text{LiHo}_x\text{Y}_{1-x}\text{F}_4$, $x = 4.5\%$ it was discovered that ac-pumping can produce long-lived 'holes' in the ac-susceptibility spectrum [8]. The authors cooled down a single crystal sample to subkelvin temperatures in a susceptometer setup that allows simultaneously applying a high-amplitude pump and a small-amplitude probe along the Ising axis.

As depicted in figure 4.30 the $f = 5$ Hz pump burns a sharp hole in $\chi''(f)$ at exactly this frequency. The phenomenology is therefore similar to optical hole burning in a solid state laser, the selective bleaching of the inhomogeneously broadened absorption spectrum. This effect in $\text{LiHo}_{0.045}\text{Y}_{0.955}\text{F}_4$ further indicates that the susceptibility spectra indeed originate from a set of oscillators rather than a distribution of relaxation times.

The response to the pump, i.e. the deepness of the hole burned in the spectra, saturates as a function of applied field h_{ac} and the associated phase shift tends to zero. The measured magnetization oscillation M , as it is called in [8], describe a Brillouin function $M = Ng_{\parallel}\mu_B \tanh(ng_{\parallel}\mu_B sh_{ac}/k_B T)$, where $s = 1/2$ for Ising spins. From the fits to the data a value of $n = 260$ as a number of spins per cluster can be estimated. This corresponds to

a cluster size of $\xi = 148 \text{ \AA}$ in diameter. Most remarkably the oscillation elapses almost dissipationless. Switching of the pump the oscillation persists for lifetimes up to the order of 10 seconds (figure 4.30).

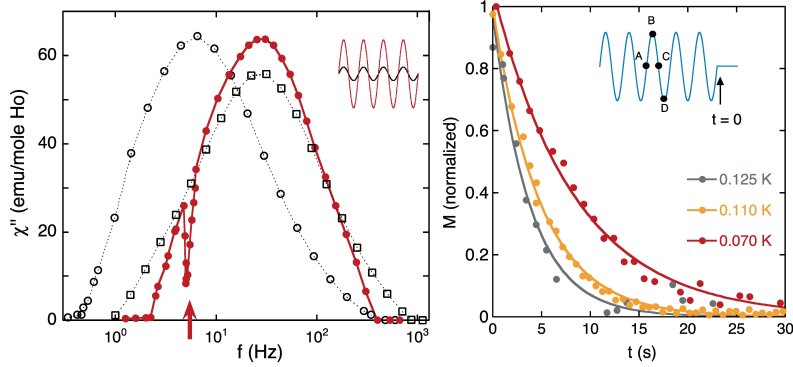


Figure 4.30: Hole burning effect LiHo_{0.045}Y_{0.955}F₄. To the left: Spectra with (red) and without (black) applying a pump signal of 5 Hz. To the right: Persistent magnetization oscillations after switching of the pump signal.

Time-Resolved SANS

By means of combining ac-susceptibility technics with time-resolved Small Angle Neutron Scattering there should be a possibility to gain further insight into the microscopic picture of the assumed spin clusters. In particular it could be investigated, how the size of the clusters and the lifetime of the oscillations are correlated to the specific pump-frequency and how the clusters can be manipulated by varying temperature and applying a transversal field. For this purpose three experiments have been performed at SANSI SINQ, with consecutively improved setups. The technical details to the experiment and in particular to the final setup are described in paragraph 2.5.

The first attempt was without any ac-susceptibility setup, a simple SANS experiment to localize the signal and to investigate its field and temperature dependence. From rough estimates only a weak signal compared to the usual background noise was previously expected. At length scales in range of the assumed cluster sizes no measurable signal could be detected. Instead the signal turned out to be broader in q , hence the objects of interest must belong to smaller length scales in the order of only a few lattice spacings. The magnetic origin of the scattering signal could be verified by its temperature and field dependence. Several Tesla and a change of about 1 K is required to cause only a marginal effect. The momentum dependence of the radial averaged signal $I(q)$ measured with the finally optimized instrumental configuration is depicted in figure 4.31.

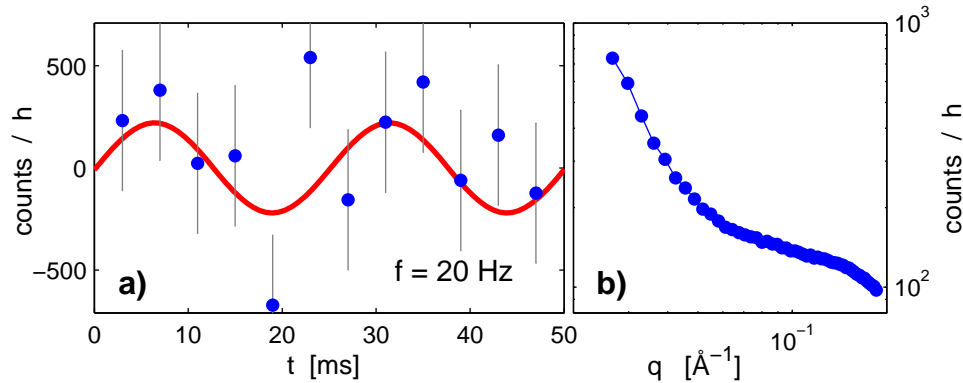


Figure 4.31: Time resolved SANS measurement at 200 mK while insitu ac-pumping at a frequency of 20 Hz. (a) Intensity as function of time bins, where the static time average has been subtracted. (b) Radial average of the static signal.

In case of the insitu susceptibility-SANS investigation several attempts have been made to detect a time resolved signal. A pump signal of 5, 10 and 20 Hz was applied at a sample temperature of 200 mK. Even with counting times in the range of a day there was no significant signal above the noise level visible. In figure 4.31 the intensity summed over a large sector of the detector is plotted as function of the collected time bins. Several choices of sectors have been analyzed but it was impossible to localize a q -range with a distinct signal. Subtracting the time-average from the time binned scattering intensity should lead to a signal with twice the frequency of the ac-pump. Twice the frequency because scattering is proportional to the moments squared. However although in many cases a harmonic function with the correct frequency fit the data slightly better than a straight line through zero, none were definitive (figure 4.31).

As a conclusion it was successfully demonstrated that such an experiment is from technically point of view feasible. Nevertheless statistical significance is one limiting factor. In a present state-of-the-art experiment, as it was here performed, there is neither a definitive proof nor disproof of the coherent oscillating spin cluster. What would be needed to get a conclusive answer? Presumably several weeks of beam time on a conventional neutron source like SINQ or a gain in neutron flux, which could be provided by the new next generation neutron sources like the planned ESS.

Summary 4.2:

In this chapter a neutron diffraction investigation of the compounds LiHo_xY_{1-x}F₄, with $x = 0.83, 0.67, 0.25, 0.2, 0.045$ was presented. Below a short summary of the main results:

- Long range ferromagnetic order could be observed for all compounds with $x \geq 0.25$. The ordering temperature T_c is suppressed proportionally to the concentration x .
- Below $x \leq 0.67$ the glassiness of the system is indicated by the appearance of history depended effects.
- In LiHo_xY_{1-x}F₄, $x = 0.33$ and $x = 0.46$, following a zero field cooling protocol one can prepare the system in the ferromagnetic state, whereas field cooling leads to a short range correlated state. In contrast to that, in an earlier dynamic susceptibility spectroscopy study the field cooling path, referred as quantum annealing, was interpreted as more efficient in establishing the ground state.
- From the hole burning effect in the susceptibility spectra of LiHo_{0.045}Y_{0.955}F₄ in the anti-glass phase the existence of coherently oscillating spin clusters was predicted. However, in a time resolved SANS investigation no conclusive evidence for such clusters could be achieved, because of statistical insignificance.

4.3 LiHoF₄ - Quantum Magnet in a Spin Bath

In LiHoF₄ quantum criticality can be studied in a system where the quantum phase transition is strongly affected by the interplay of the electronic spins with a nuclear spin bath. Although the effective transverse field Ising model provides in the case of LiHoF₄ a good approximative description of the real system, inelastic neutron scattering investigations have demonstrated that the innocently weak hyperfine interaction to the nuclear spins in fact has dramatic effects on the excitation spectrum around the quantum phase transition [11]. As a general hallmark a quantum critical point should be accompanied by a softmode in the characteristic excitations and a divergence in the coherence length. This even is a prediction from the meanfield/RPA calculation of the simplest version of the transverse field Ising model (see chapter 3.2). Instead Rønnow et al. [11] discovered that the softening of the electronic excitation in LiHoF₄ is forestalled by entanglement to the nuclear spins. The key results of this study is summarized in figure 4.32. At $H = H_c$ there remains a gap of around 0.25 meV at $q = (200)$, which is equivalent to the wavevector $q = (000)$ corresponding to a ferromagnetic ordering. Nevertheless, based on the present knowledge, the existence of a quantum phase transition in LiHoF₄ is regarded as indisputable. Therefore the question arises whether or not there exists a soft mode and if so which elementary excitations rather than the previously considered electronic mode are related to the quantum criticality. This question and an interpretation of the results will be addressed in more details in the next paragraphs.

The here presented work is a continuation of the inelastic neutron scattering investigation reported in [11, 24]. Experiments have been performed at the tree-axis spectrometers PANDA FRMII in Munich and V2 FLEX at HZB in Berlin. The same sample as in [11, 24] was used. As a first result the above motioned incomplete electronic soft mode can be confirmed, see figure 4.34. Furthermore the aim was to verify experimentally the predictions from [11], in particular the role of finite temperature on the critical dynamics.

4.3.1 Spin Bath and Decoherence

Development of novel solid state quantum devices is one of the most popular topics of contemporary applied physics. The challenge for preparation and manipulation of qbits in such devices is to preserve the entangled quantum states for a long enough time against decoherence effects. The origin for decoherence is coupling to a background environment, either delocalized excitations, an oscillator bath, or localized states, a spin bath. Examples are phonons in the first and nuclear spin in the second case. Coupling to an environment like phonons can be circumvented by freezing out, while for example the hyperfine interaction is intrinsically present in most of the

materials and can hardly be controlled from outside, except in special cases for which particular isotopes have no nuclear spin.

A theory of the spin bath has been developed in the work of N. V. Prokof'ev and P.C.E Stamp [55]. They addressed the role of coupling to nuclear spin originally in view of decoherence in localized magnetic clusters and single magnetic molecules. Ronnow et al. had the idea to adapt this notion of the spin bath to their system LiHoF₄ and show its importance for quantum phase transitions, that can be considered as an excellent arena for looking at fundamental quantum properties of strongly interacting spins [11]. The use of the term 'bath' may cause confusion, if one associates with the common definition of a bath as a reservoir. Here the term is considered in the sense of [55]: A spin bath is an environment constituted from localized, secondary degrees of freedom. Instead of considering the LiHoF₄ system as one unit, one can divide it into a subsystem of interacting electronic spins and the nuclear moments forming an environment. The main channel of the inelastic

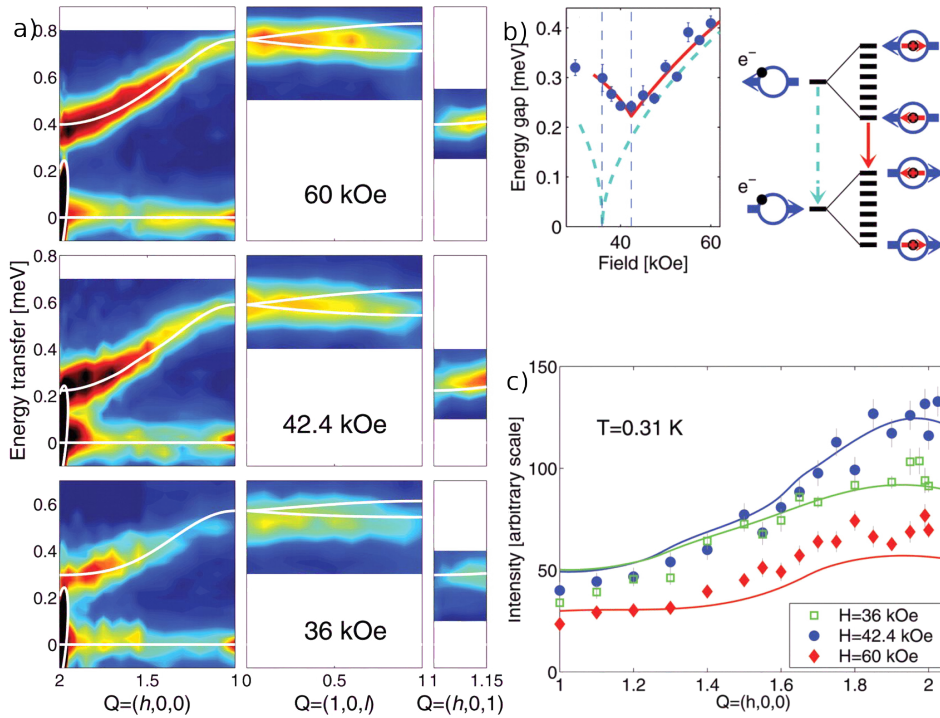


Figure 4.32: . Summarized results reported in [11]. (a) Pseudocolor representation of the inelastic neutron scattering intensity above at and below the critical field. (b) Incomplete softening of the electronic mode. (c) Intensities of the excitations along $q = (h00)$ at the same values of the field as in panel (a).

neutron scattering cross section is probing only the electronic spins. Formally this corresponds to a partial trace over the nuclear spin states. But tracing out the environment degrees of freedom in the density matrix of the joint system can be regarded as the mechanism leading to quantum decoherence. The hyperfine coupling of the electronic subsystem to the nuclear spin bath not only causes a gap in the energy spectrum at QCP but also modifies the form of the wave functions itself. The neutron scattering intensities of the excitations contain additional information because they are proportional to spatial Fourier transformed matrix elements of the momentum operators. The momentum dependence provides the real-space dynamical coherence length ξ_c of the excited state. In a clean system without hyperfine coupling there is $\xi_c \rightarrow \infty$ by approaching the quantum critical point. Therefore at $H = H_c$ the scattering intensities should diverge at reciprocal space points like $q = (200)$ equivalent to the ferromagnetic ordering wave vector. But in the real system only a broad maximum is found, with a ξ_c in the order of the spacing between the Holmium ions [11], see figure 4.32c. This means that the electronic subsystem remains subcritical. Furthermore Rønnow et al. remarked that these results imply that the hyperfine interaction limits the distance over which the electronic wave functions can be entangled and thus this is a direct demonstration of the limitation of quantum coherence in space via coupling to a nuclear spin bath [11]. But one has to be aware that what is probed with neutrons is a spin-spin-correlationfunction and not a proper entanglement measure. Therefore one should be cautious with conclusive statements about entanglement and decoherence. Furthermore, the calculations as RPA and $1/z$ may pretend to provide some insight, but clearly they are suitable to address this question only to certain extent. As a remark, the here mentioned $1/z$ calculation is a special diagrammatic series expansion method performed by J. Jensen to reproduce the phase diagram and excitation spectra in LiHoF_4 [11, 24]. To refine the theory of the spin bath and the decoherence effects in the particular case of LiHoF_4 is desirable and might also promote new interesting ideas for further experimental projects.

4.3.2 Nuclear-Electronic Criticality

The elementary excitations associated with the quantum phase transition in LiHoF_4 are considered to have entangled nuclear/electronic character and a much lower energy range of about 10-meV compare to the magnetic excitation of electronic origin [11]. Sufficiently low temperatures would reveal these modes as propagating and softening to zero at the QCP, but at the temperatures reachable in the experiments there is dephasing of the composite modes as consequence of thermalization [11]. As experimental evidence is the appearance of strong quasi-elastic scattering around $q = (200)$ at the

critical field has mentioned [11], visible in figure 4.32.

Although the resolution limitations of neutron scattering techniques do not allow elucidating the details of these low energy excitations, it is nevertheless possible to investigate field and temperature dependence of the quasielastic signal and map out its localization in reciprocal space (Figure 4.33). Indeed the intensity reaches its maximal value at critical field and around the ferromagnetic wave vector $q = (200)$. In contrast to the observation of the previous investigation [11] only a weak signal could be detected at low temperatures, i.e. closest to the QCP. But in [11] they assume to have a temperature $T = 310$ mK, if one considers the measured critical field $H_c(T)$ and the reported phase diagram of LiHoF₄ [9]. In the new experiment the thermalization was improved and therefore a lower temperature could be reached. Furthermore, the investigation of the quasielastic signal has been investigated for a series of temperatures in the whole range up to $T_c = 1.53$ K. The scattering is strongly increasing for increasing temperatures. The different temperatures in the two experiments could explain the difference in signal strength. Obviously the larger intensity at high temperatures has not its origin in scattering from the assumed quantum critical excitations. The system enters the classical critical region with the scattering related to thermal fluctuations. Therefore, we may speculate that

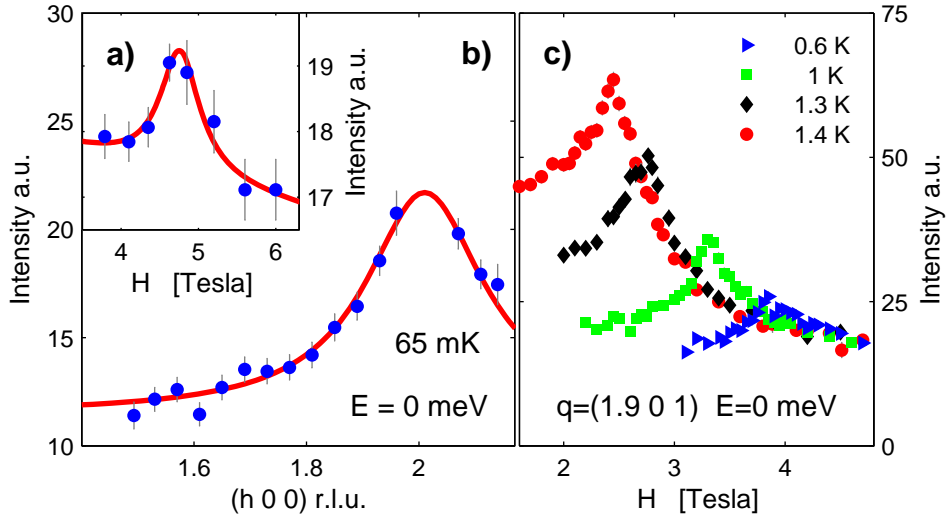


Figure 4.33: . Field and momentum dependence of the quasi elastic scattering associated with the critical excitation close to the QCP (a) and for increased temperatures (b). The strong signal enhanced temperatures must be considered as scattering from thermal fluctuations related to the classical critical region.

the weak signal observed at low temperatures is in fact also only a tail from this contribution. Nevertheless, one should not forget that the channel in the cross section describing scattering from the expected entangled nuclear/electronic modes is order of magnitudes lower than that of the usual considered channels. Therefore, one could conclude from the presented results that if these states are really visible in neutron scattering, then the signal is probably close to the noise level.

4.3.3 Temperature Effects

The theory of the spin bath applied to nanomagnets [55, 56] states that decoherence due to hyperfine interactions can be reduced by rising the temperature. The thermal fluctuations effectively decouple the system from the nuclear moments. Of course entering the oscillator bath dominated region has then an effect in the opposite direction. Therefore at intermediate temperature there should exist a window with minimal decoherence. In the case of LiHoF_4 the magnetic excitations constitute an oscillator bath and therefore similar behavior is suggested [11]. Rønnow et al. proposed as quantitative measure the ratio Δ/δ , where Δ denotes the gap at QCP and δ the field induced single ion splitting, which plays the role of a normalization. The decoherence window for the electronic subsystem is achieved if the ratio Δ/δ is minimal. The counterintuitive prediction for quantum critical systems is therefore that maximum (electronic) criticality is reached not as expected at $T = 0$ K, but rather at an intermediate temperature $0 < T < T_c$. From the $(1/z)$ calculation a minimum of the ratio Δ/δ at $T = 1$ K is reported [11]. The RPA calculations based on the full Hamiltonian as well as on reduced models are not able to reproduce this result, the ratio is not approaching a distinct minimum. But RPA is of course only the zero order approximation in the $(1/z)$ expansion.

To test the predictions about enhanced electronic criticality by decoupling from the spin bath at temperatures above $T = 0$ K neutron scattering spectra have been measured for a series of temperatures at the critical fields $H_c(T)$ and selected points in reciprocal space. In the experiment previous to the inelastic scans the critical fields $H_c(T)$ for each temperature was determined measuring the onset of the ordering parameter observable in the field dependence of a magnetic Bragg peak. The phase diagram is depicted in figure 4.36c. In the V2 experiment the gap of the characteristic excitation as well as the zone boundary energy was measured in an energy scan at $q = (2 - \epsilon, 0, 0)$ and $q = (1, 0, 0)$ respectively and for temperatures ranging from about 50 mK up to 1.5 K. In the experiment on the PANDA instrument the neighborhood of (200) position was not in the accessible q-range given by the chosen configuration. Therefore the investigation was performed around $q = (101)$, which is also equivalent to the ferromagnetic point. The

two different experiments in the end provided comparable results but the analysis is concentrated on the V2 data set, because it is more complete and has the better resolution. In figure 4.34 the full field dependence of the gap at high and low temperature is shown for the reciprocal space point $q = (1 + \epsilon, 0, 1)$. Furthermore for selected temperatures at critical field $H_c(T)$ the full dispersion relation along the high symmetry direction ($h00$) was mapped out (figure 4.34). Already from these color maps it is clearly visible that the gap, i.e. the excitation energy at zone center, weakens with increasing temperatures as predicted.

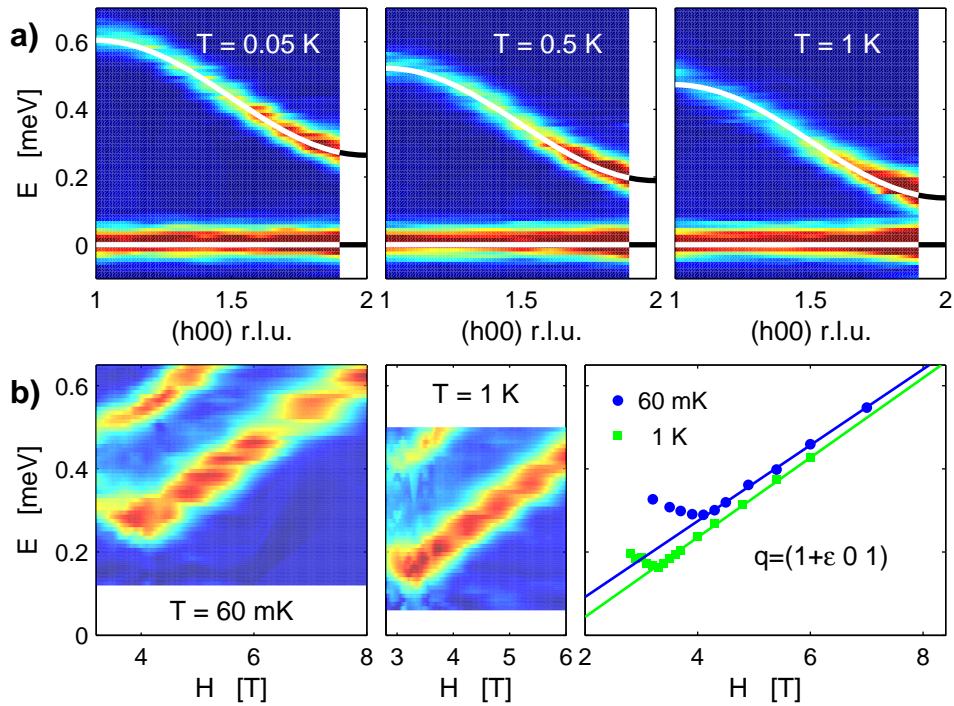


Figure 4.34: Dispersion relation (a) and field dependence (b) of the gap measured in the high and low temperature region.

In the analysis of the energy scans at the zone center and zone boundary a damped harmonic oscillator model is used to fit the data (Figure 4.35). Reminding the formula obtained for the dispersion in the Ising model and taking for the single ion splitting energy δ the mean value of both excitation energies may be a good choice. According to J. Jensen, the author of the $(1/z)$ calculation [24], one should instead consider more precisely the excitation energy at $q = (0.658, 0, 0)$. Therefore also scans at this point has been performed for selected temperatures and in following δ is obtained from this excitation energy. Nevertheless in the results this only implies a marginal

change, since δ acts as an arbitrary chosen normalization factor. The experimental data show that the dispersion along $(h00)$ can be very well modeled with a cosine function. To obtain the gap Δ the data for $q = (1.9, 0, 0)$ has been extrapolated to $q = (2, 0, 0)$, which cannot be direct experimentally determined due to the vicinity of the Bragg peak. The measured values for the three mentioned q -vectors are depicted in figure 4.36 plotted as function of the field. The excitation energy at zone boundary and δ are linear over the whole range, in particular $\delta \propto H_c(T)$ is fulfilled. One of the final results from the experiment is that the determined ratio Δ/δ is indeed increasing with temperature (figure 4.36), but does not establish a distinct minimum at intermediate temperature and it deviates significantly from the predicted curve in [11].

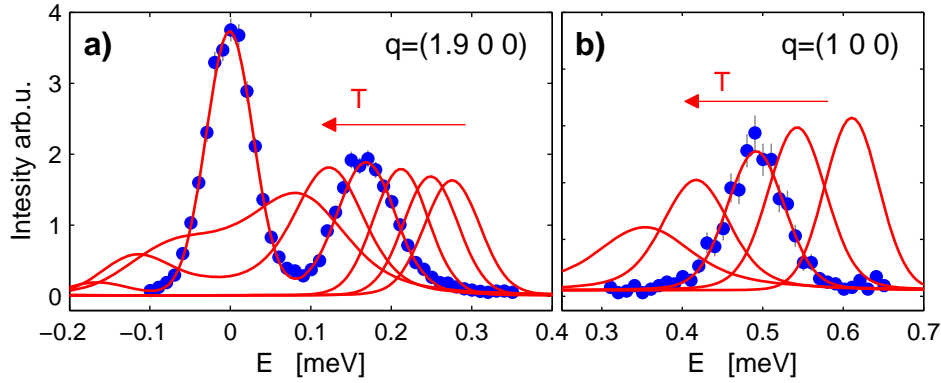


Figure 4.35: Examples of energy scans performed along the phase boundary and different temperatures in the range from 50 mK up to 1.5 K. The red lines represent the fits to a damped harmonic oscillator model as described in the text.

One further observation is the broadening of the spectral lines at increasing temperatures, directly visible in the scans (figure 4.35) and in the half width half maximum (figure 4.36d) determined from the damped harmonic oscillator line shape fitted to the data. The broadening at zone center and boundary are identical and can be described by the following phenomenological model:

$$\Gamma_{\text{DHO,WHM}} \sim e^{-\delta(H,T)/k_B T}. \quad (4.3.1)$$

The common interpretation for the increased line width would be at the first glance that the life time of the excitation is reduced due thermal fluctuations increasing in temperature. Surprisingly the broadening is independent of momentum. Here another explanation is suggested. In analogy to the terminology of optical systems the idea is that the broadening of the spectra is inhomogeneous rather than homogenous. The broadening is the result over

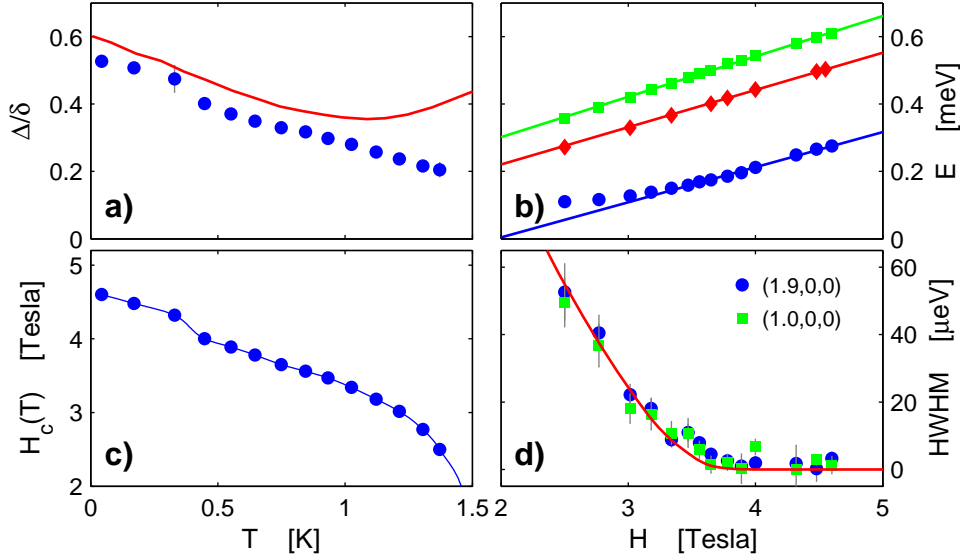


Figure 4.36: (a) Critical ratio Δ/δ determined along the phase boundary line. The red curve in (a) shows the result from the $(1/z)$ calculation in [11]. The measured excitation energies are depicted in panel (b) for $q = (1.9, 0, 0)$ in blue, $q = (1.0, 0, 0)$ in green and $q = (0.658, 0, 0)$ in red. (c) Phase boundary line. The half width half maximum of the spectral lines is increasing with temperature, as depicted in panel (d). Details are described in the text.

an incoherent sum of excitations different in energy due to local longitudinal fields caused by the thermally randomized nuclear moments. This idea will be highlighted in the following paragraph.

4.3.4 Effective model

Quantum criticality in LiHoF₄ is a rather complex problem due to the interplay between nuclear and electronic spins. It is not obvious how the full Hamiltonian could be truncated to a model only containing the crucial parts. But since the electronic excitations observed in the experiments are ineffective for quantum criticality one can argue that on the other hand a description of the latter may not require the details of the quantum phase transition of the system. The electronic subsystem, the incomplete softening of the modes and the temperature effects may be explained with a simpler effective model. This also circumvents hand waving arguments that stress the notion of entanglement and decoherence.

Due to the strong Ising character of the moments in LiHoF₄, only the inter-

actions involving the z-component of the spins are considered to obtain the effective Hamiltonian in leading order.

$$\mathcal{H} = -\frac{1}{2} \sum_{ij} J_{ij} \sigma_i^z \sigma_j^z - \Gamma \sum_i \sigma_i^x + \sum_i A I_i^z \sigma_i^z. \quad (4.3.2)$$

This problem can be solved by states separable in an electronic and nuclear part.

$$|\psi_{\mathcal{I}n}\rangle = |\phi_n\rangle \otimes |\mathcal{I}\rangle. \quad (4.3.3)$$

$$\begin{aligned} \mathcal{I} &= (\iota_1, \dots, \iota_N), & \iota_i &\in \{-I, -I+1, \dots, I-1, I\} \\ |\mathcal{I}\rangle &= \otimes_{i=1}^N |\iota_i\rangle, & I_i^z |\iota_i\rangle &= \iota_i |\iota_i\rangle. \end{aligned} \quad (4.3.4)$$

$$\mathcal{H} |\psi_{\mathcal{I}n}\rangle = \mathcal{H}_s(h_{\mathcal{I}}) |\phi_n\rangle \otimes |\mathcal{I}\rangle = E_{n\mathcal{I}} |\psi_{\mathcal{I}n}\rangle. \quad (4.3.5)$$

Hence the effective Hamiltonian is equivalent to the longitudinal random field Ising model in a transversal field,

$$\mathcal{H}_s(h) = -\frac{1}{2} \sum_{ij} J_{ij} \sigma_i^z \sigma_j^z - \Gamma \sum_i \sigma_i^x + \sum_i h_i \sigma_i^z, \quad (4.3.6)$$

where the random field $h_{\mathcal{I}} = (h_1, \dots, h_N) = A \cdot (\iota_1, \dots, \iota_N)$ is induced by the nuclear moments.

The meanfield/RPA solution of this problem is discussed in chapter 3.2. For zero longitudinal field there is soft mode for $q = 0$ at the quantum phase transition. For a nonzero h the system undergoes a cross over instead of a sharp transition, there remains a gap in the excitation spectra and the sharp onset of the order parameter is smeared out.

The scattering function, i.e. the cross section, for inelastic neutron scattering is given by the following expression.

$$\begin{aligned}
\mathcal{S}(q, \omega) &\sim \sum_{\mathcal{I}, \mathcal{I}'} \sum_{n, m} \frac{e^{-\beta E_{n\mathcal{I}}}}{Z} \langle \psi_{\mathcal{I}'m'} | S_i^\alpha S_j^\beta | \psi_{\mathcal{I}n} \rangle \delta(E_{n\mathcal{I}} - E_{m\mathcal{I}'} \pm \hbar\omega) \\
&= \sum_{\mathcal{I}, \mathcal{I}'} \sum_{n, m} \frac{e^{-\beta E_{n\mathcal{I}}}}{Z} \langle \phi_m | S_i^\alpha S_j^\beta | \phi_n \rangle \cdot \langle \mathcal{I}' | \mathcal{I} \rangle \delta(E_{n\mathcal{I}} - E_{m\mathcal{I}'} \pm \hbar\omega) \\
&= \sum_{\mathcal{I}} \frac{Z_{\mathcal{I}}}{Z} \sum_{n, m} \frac{e^{-\beta E_{n\mathcal{I}}}}{Z_{\mathcal{I}}} \langle \phi_m | S_i^\alpha S_j^\beta | \phi_n \rangle \delta(E_{n\mathcal{I}} - E_{m\mathcal{I}} \pm \hbar\omega).
\end{aligned} \tag{4.3.7}$$

Here $Z = \sum Z_{\mathcal{I}}$ and $Z_{\mathcal{I}} = \sum_n \exp(-\beta E_{n\mathcal{I}})$ denotes the partition sum over the complete system and the electronic subsystem respectively. In the considered channel of the cross section the nuclear spin states are formally traced out and therefore unaffected by the scattering process. The cross section can be written as incoherent sum over the scattering functions $\mathcal{S}_{\mathcal{I}}$ of the corresponding random field Ising system.

$$\mathcal{S}(q, \omega) = \sum_{\mathcal{I}} \frac{Z_{\mathcal{I}}}{Z} \mathcal{S}_{\mathcal{I}}(q, \omega). \tag{4.3.8}$$

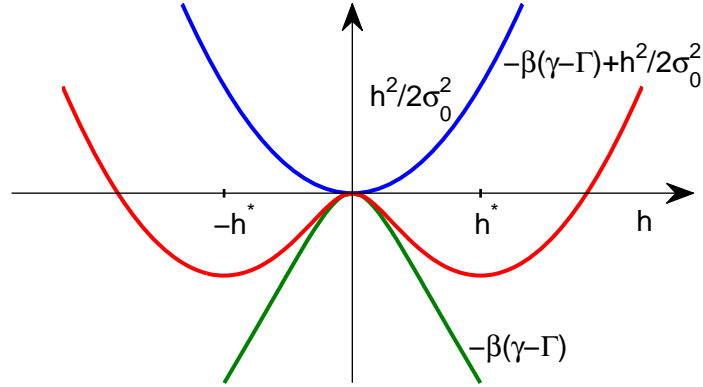
The relation 4.3.8 is an exact expression, but approximations can hardly be circumvented in evaluating the functions $\mathcal{S}_{\mathcal{I}}$ as well as the partition sum. In the following this will be done using the results from meanfield calculations. In this approximation all nuclear spin configurations with $\bar{h}_{\mathcal{I}} = h$ leading to identical expressions.

$$\mathcal{S}_{\text{meanfield}}(q, \omega) = \sum_h \mathbf{w}(h) \cdot \mathcal{S}_h(q, \omega), \quad \mathbf{w}(h) = \sum_{\{\mathcal{I} | \bar{h}_{\mathcal{I}}=h\}} \frac{Z_{\mathcal{I}}}{Z}. \tag{4.3.9}$$

The scattering function \mathcal{S}_h is obtained via RPA and fluctuation dissipation theorem. The partition sum in meanfield approximation is given as follows.

$$\begin{aligned}
Z_{\text{meanfield}}(h_{\mathcal{I}}) &= \sum_{n_i \in \{\pm 1\}} e^{-\beta \gamma n_i} = \sum_{m=0}^N \frac{N!}{(N-m)!m!} e^{-m\beta\gamma} e^{(N-m)\beta\gamma} \\
&= \frac{e^{N\beta\gamma}}{1 + e^{-2\beta\gamma}}.
\end{aligned} \tag{4.3.10}$$

The degeneracy $g(h)$, i.e. the number of nuclear spin arrangements \mathcal{I} with identical $\bar{h}_{\mathcal{I}} = h$ is for large system sizes N approximatively proportional to


 Figure 4.37: Effective longitudinal field h^* as minimum of $f(h)$

a normal distribution.

$$\begin{aligned}
 g(h) &= a(N) \cdot e^{-\frac{h^2}{2\sigma(N)^2}} & (4.3.11) \\
 a(N) &= \frac{1}{\sqrt{2\pi N}\sigma_0} \cdot e^{\log(2I+1)N} \\
 \sigma(N) &= \frac{\sigma_0}{\sqrt{N}} = A\sqrt{\frac{I(4I+1)}{3} - I^2} \cdot \frac{1}{\sqrt{N}}.
 \end{aligned}$$

Therefore it follows in the meanfield approximation for the weights in the functions $w(h)$ the following expression:

$$w(h) = g(h) \cdot \frac{Z(h)}{Z} \sim e^{N \cdot \left(\beta\gamma - \frac{h^2}{2\sigma_0^2} + \log(2I+1) \right)}. \quad (4.3.12)$$

Evaluating the sum in the formula of the total scattering function in the thermodynamic limit $N \rightarrow \infty$ only the leading weight function survives, i.e. that with maximal exponent.

$$\mathcal{S}(q, \omega) \propto \mathcal{S}_{h^*}(q, \omega) \quad \text{with} \quad f(h^*) = \min\{f(h) \mid -I \leq h \leq I\}. \quad (4.3.13)$$

$$f(h) := \frac{h^2}{2\sigma_0^2} - \beta(\gamma(h) - \Gamma). \quad (4.3.14)$$

The function $f(h)$ is plotted schematically in figure 4.37, for a fixed beta and Γ according to the meanfield-expression (3.2.8) for γ . The minimum of $f(h)$ is given by the root h^* of its derivative.

Obviously at zero temperature, i.e. $\beta = \infty$, the longitudinal field is $h^* = \pm I$ and therefore the gap maximal. For increasing temperatures the value h^* and as a consequence also the gap diminish. This meanfield like treatment of the model provides an explanation for the incomplete softening of the excitation and the temperature dependence of the gap. On the other hand the line width is infinitively sharp for all temperatures. This is most likely a shortfall due to the approximation made in calculating the partition sums $Z(h_{\mathcal{I}})$ and identifying all configurations $h_{\mathcal{I}}$ with equal averaged longitudinal field $\bar{h}_{\mathcal{I}}$ as identical. But the broadening of the line width can be understood qualitatively from expression (4.3.8). The total scattering function is an incoherent sum of the scattering functions for all the different nuclear spin configurations. Each of them shows a gap according to the particular $h_{\mathcal{I}}$. Of course each of these may have damped rather than sharp excitations. But presumably the main contribution to the broadening observed in the total cross-section is due to the weighted sum over differently shifted modes. The experimental fact for LiHoF₄ that the line width is showing a temperature difference independent of the wave vector q would be conform with this assumption. A more sophisticated treatment of the proposed model could provide a further insight.

The here presented evaluation of the proposed model so far provides similar results as if the full system, electronic and nuclear, is treated from begin in an RPA or more sophisticated in a $1/z$ calculation. But the advantage here is that the problematic steps in the approximation are done at a later stage in the treatment. Looking at the problem in this way leads to a further gain in understanding, at least qualitatively. Furthermore, the complexity of the system is cut down to a more abstract stage where a theoretical treatment is more feasible. The impractical task of solving LiHoF₄ with all its complications, of which most of them may be irrelevant, is shifted to the task of solving the transverse field Ising model in a random field. This would be then also the suitable frame to discuss decoherence and entanglement in the system.

4.3.5 Conclusion and Outlook

Quantum criticality in the compound LiHoF₄ turns out to be more complicated than in its simplest description in form of the transverse field Ising model. This provides an insight into the robustness of quantum criticality in non-perfect, hence realistic systems. Neutron scattering investigations demonstrate that the electronic excitations are gaped, instead of a softening at QCP, due to coupling to the nuclear moments. By increasing temperature thermal fluctuations reduce the influence of the spin bath, the gap diminishes and the electronic subsystem move closer to criticality. On the other hand the line width and quasielastic scattering increase. It has been demon-

strated that the essential experimental results obtained for the excitation spectra can be described effectively by the random longitudinal field Ising model in a transversal field. This is therefore also the suggested toy-model for further theoretical investigations.

With regards towards further experiments one can ask the questions, if there are ways for controlled external manipulation such that the quantum system can be decoupled from the spin bath and pure electronic criticality will be reestablished, similar as the thermal fluctuations do in an uncontrolled manner? The idea is to perform so called pump probe experiments, more precisely activation of the nuclear spins by irradiation with electromagnetic waves at NMR frequencies. The region of interest is located in the phase diagram where the phase boundary and excitations are highly affected by the hyperfine coupling. Without change in temperature and transverse field, but by allowing induced perturbations in the nuclear spins it should be possible to move the system across the quantum phase transition in the equivalent of a "super-cooled" state. Nevertheless the realization of such in-situ experiments is more complicated than it seems on the first glance and is from a technical point of view demanding, because it involves non-standard NMR techniques at very low temperatures and rather high fields.

Summary 4.3:

In this chapter a neutron spectroscopy investigation of the critical dynamics in the compound LiHoF₄ was presented. Below a short summary of the main results:

- At the quantum critical point there is no softmode in the characteristic (electronic) excitations due to the influence of hyperfine interactions to the nuclear momenta. Thereby LiHoF₄ offering an ideal system to study in a controlled way the robustness of quantum criticality in non-perfect (hence realistic) systems.
- The gap in the excitation spectra and the non-diverging coherence length of the electronic subsystem was interpreted as a decoherence effect induced by the coupling to the nuclear spin bath, i.e. a local environment of secondary degrees of freedom.
- It was demonstrated that thermal fluctuations tends to decouple the electronic subsystem from the spin bath. Hence the coherence window or maximal criticality of the electronic subsystem is reached at a nonzero temperature. However, by further increasing the temperature the system finally crosses over to the thermal critical regime, where the excitations spectra exhibit a significant damping.
- As an alternative to the spin bath interpretation it was proposed that LiHoF₄ can be considered effectively as a transverse field Ising model in a longitudinal random field.

4.4 LiErF₄ - QPT in a dipolar XY-Antiferromagnet

Notwithstanding the many possibilities of all LiReF₄ materials, great activity has centered on just two members of the family, LiTbF₄ and LiHoF₄, and their respective dilution series. The experiments described in the following paragraphs represent a major step forward in that they provide the first look at the magnetic order and both the quantum and thermal phase transitions for an antiferromagnetic member of the LiReF₄ family. The scenario of either ferromagnetic or antiferromagnetic order as a result of the subtle interplay between dipolar interaction and geometrical arrangements is subject of a longstanding discussion and pointed out already 60 years ago by Luttinger and Tisza [57].

The limited data published on the low temperature magnetic properties of LiErF₄ to date include susceptibility[32] and specific heat[33] measurements showing a transition around 380 mK. From the susceptibility measurements, first ferromagnetic then antiferromagnetic ordering were proposed, but up to date no neutron diffraction results exist such that the magnetic structure remained as an open question. Furthermore the low-temperature properties in an applied magnetic field and the phase diagram were unknown. Here, in this work a comprehensive neutron scattering investigation and specific heat study will be presented [58, 59].

Recall from paragraph 4.1.2 about crystal fields that one can derive within the ground-state doublet a minimal effective Hamiltonian that is suitable to describe the low-temperature magnetic properties of the system and also provides the starting point for future theoretical work. The effective spin operators can be written as $S^\alpha = C_\alpha \sigma^\alpha$, where $C_x = C_y = 3.480$ and $C_z = 0.940$, leading to the following Hamiltonian,

$$\mathcal{H}_{eff} = \sum_{ij\alpha\beta} \mathcal{J}_{ij}^{\alpha\beta} \sigma_i^\alpha \sigma_j^\beta + g_\perp (\sigma_i^y B^y + \sigma_i^x B^x) + g_\parallel \sigma_i^z B^z, \quad (4.4.1)$$

where σ denotes the Pauli operators and $\mathcal{J}_{ij}^{\alpha\beta} = (\mu_B g_L)^2 C_\alpha C_\beta D_{ij}^{\alpha\beta}$ the magnetic coupling tensor between the effective $S = 1/2$ spins. In this model only the dipole-dipole interaction $D_{ij}^{\alpha\beta}$ is considered, whereas the exchange interaction J_{ex} is ignored. The refinement of J_{ex} (section 4.5) states that the exchange coupling is close to zero and can therefore be neglected.

4.4.1 Phase Diagram and Magnetic Structure

The magnetic structure was determined from single-crystal measurements (E4 HZB) and verified by powder (DMC SINQ) neutron diffraction. At low temperatures, magnetic scattering appeared at Bragg positions ($h + k +$

$l = \text{odd}$) different from those of the structural peaks ($h+k+l = \text{even}$), proving directly that the magnetic structure is antiferromagnetic. Simple intensity inspection rule out antiferromagnetic orientation of the moments in the ab -plane, since that would give zero intensity at (100) and (010), which we observe to be among the strongest magnetic peaks, and the magnetic structure most consistent with the data is a bilayered antiferromagnetic ordering (BLAFM), as depicted in figure 4.38. The refinement powder diffraction yielded an ordered moment $\langle J^x \rangle = 2.2 \pm 0.1$, which is reduced from the value $\langle J^x \rangle_{MF} = 3.0$ predicted by a mean-field calculation.

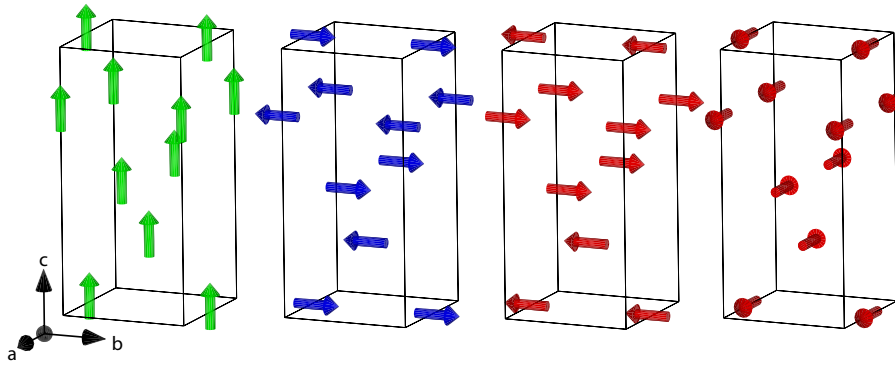


Figure 4.38: a) Magnetic structures of LiReF₄: ferromagnetic order (green) as in the case of LiHoF₄, nearest neighbour antiferromagnetic order (blue) and bi-layered antiferromagnetic order (red). In the case of LiErF₄ the bi-layered antiferromagnetic (BLAFM) structure is preferred due to planar crystal field anisotropy and dominance of dipole interactions over exchange coupling between the magnetic moments.

For the BLAFM structure, two crystallographic-equivalent configurations exist, one with moments along the a -axis and one with moments along the b -axis. In reality the crystal will either divide into several domains of each or the configurations might superpose coherently. From the zero-field neutron diffraction data, it is not possible to conclude which scenario takes place. A very small field of 300 Oe along the crystallographic b -axis causes the (100)-type reflections to vanish (see fig. 4.39). This crossover like behavior is not interpreted as a phase transition but as a redistribution of domains. Since in neutron scattering moments along the scattering vector do not contribute to the intensity, the (100) reflection is associated with the configuration, where the moments point along the b -axis. Momenta parallel to the field are energetically less preferable than those lying perpendicular, because the latter can tilt towards the field with little cost of interaction energy. Hence we conclude that the zero-field structure is a distribution of spatially separated domains with moments along a and b , respectively, and that above 300 Oe

a single domain is populated.

For the magnetic ordering temperature a value of $T_N = 373 \pm 5$ mK was found, in good agreement with previous reports. The field dependence of the characteristic magnetic Bragg peaks measured at a temperature $T=100$ mK is shown in fig. 4.39d), for magnetic fields applied along the crystallographic c - and b -axes. For a field along the c -axis, the intensity of the (010) peak, which corresponds to the order parameter squared, decreases and disappears at a sharp quantum phase transition with $H_{c\parallel} = 4.03 \pm 0.02$ kOe. For a

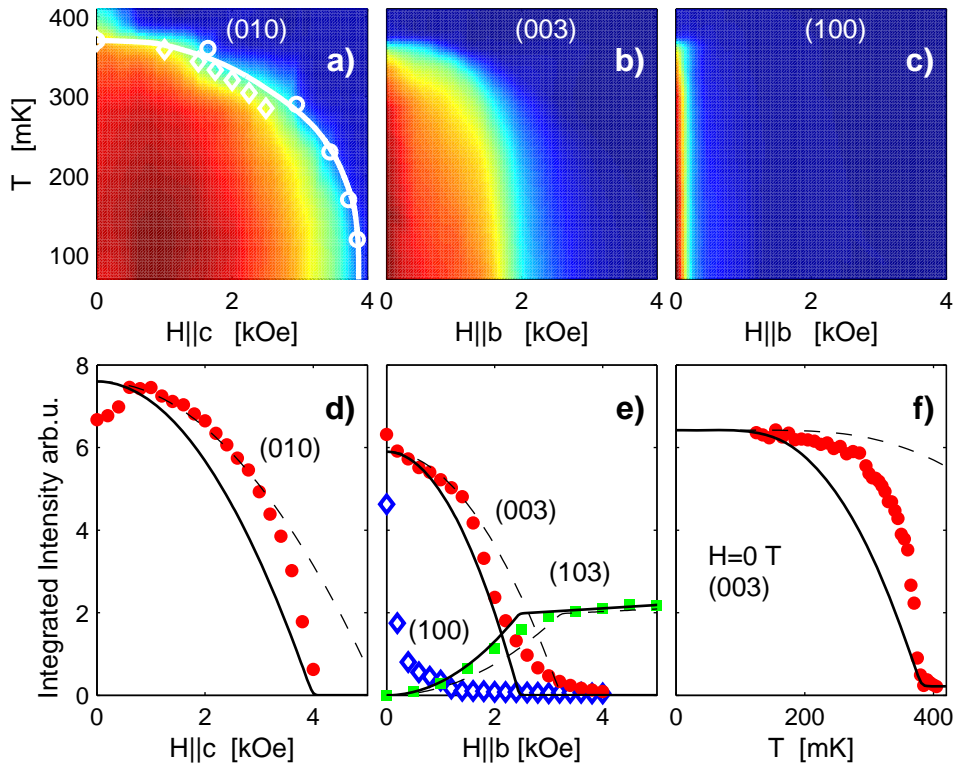


Figure 4.39: a-c) Field-temperature phase-diagrams with color-representation of the neutron scattering intensity of the magnetic Bragg peaks: (010) with $H\parallel c$, (003) and (100) with $H\parallel b$ ($\perp c$). Diamonds mark the peak in specific heat measurements. d,f) Field dependence of magnetic Bragg peak intensities at a temperature of 100 mK in the case of a field along c : (010) and along b : (100), (103), (003). e) Temperature dependence of the (003) intensity. In a,d-f), dashed lines are mean-field calculations using the refined parameters. Solid lines are the same calculations with temperature and field axes scaled by 0.52 and 0.76, respectively, to match the measured T_N and H_c . For both field directions the same scaling factor was used.

field applied along the crystallographic b-axis, the (100) peak disappears first due to mono-domain formation. The (003) peak, which is independent of *ab*-domains, decreases towards $H_{c\perp} = 2.0 \pm 0.2$ kOe, but with a long tail remaining out to 4 kOe. Simultaneously, the (103), which measures the uniform FM component, increases strongly towards a kink at $H_{c\perp}$, corresponding to maximal polarization of the ground-state doublet. Above $H_{c\perp}$ it shows a weak linear increase, achieved by mixing-in with higher lying crystal field levels.

In the case of LiHoF₄ a mean-field RPA model is able to predict the phase diagram and the excitation spectra within the limits of the approximation. Using the refined crystal-field parameters the mean-field calculation, as presented in chapter 3.3, yielding the correct ordered structure and a qualitatively correct phase diagram. However, the calculated transition points $T_N = 728$ mK, $H_{c\perp} = 3.25$ kOe and $H_{c\parallel} = 5.25$ kOe are significantly overestimated. In contrast to LiHoF₄, the nearest-neighbour exchange coupling parameter cannot be used to fine-tune the phase diagram, since in the bilayered structure each moment has two parallel and two anti-parallel neighbors, hence canceling out the exchange term. Including the hyperfine interaction in the mean-field calculation had little effect. In this case the calculated critical values are $H_{c\parallel} = 5.75$ kOe and $T_N = 735$ mK.

It was also verified that the effective model (4.4.1) gives indistinguishable results, and indeed the obtained critical values in the single ion mean-field treatment are $H_{c\parallel} = 5.0$ kOe and $T_N = 705$ mK. An attempt to improve the calculation was undertaken by dividing the lattice into blocks of eight spins, which then are diagonalized together. Nearest neighbor interactions beyond the block were included using periodic boundary conditions. Further interactions were treated as self-consistent mean fields. The results showed a 7.5% reduction in T_N compared to the simple single ion mean-field approach. Albeit not sufficient to match the experiment, this indicates that a role is played by entangled states, which are allowed by simultaneous diagonalization of small clusters but not in the semi-classical mean-field description. More generally, it should be anticipated that fluctuations are more significant due to both the antiferromagnetic coupling and the less constraining planar anisotropy, as compared to the FM system with Ising anisotropy. Therefore a more sophisticated approximation beyond mean-field RPA is needed to describe the system accurately.

Scaling the temperature and field to match T_N and $H_c(0)$, the $H_c(T)$ curve is well described (Fig. 4.39a), but both the increase of the measured Bragg peak intensity as a function of temperature and field are more abrupt than the mean-field prediction (Fig. 4.39d,e). Deep in the ordered phase, the mean-field calculation may work, but towards the transition, fluctuations gain in importance. The onset of magnetic Bragg intensity, proportional

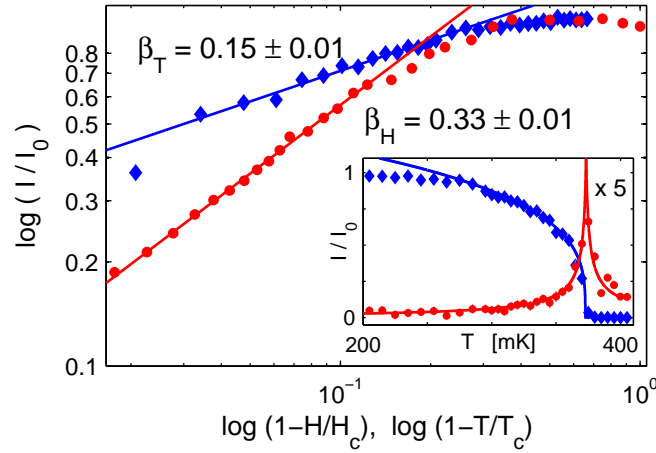


Figure 4.40: Critical behavior of LiErF_4 in the ordered regime as a function of T at $H = 0$ (blue) and an applied field H along the c -axis at $T = 80$ mK (red). Lines are power law fits described in the text. Inset: From the raw neutron diffraction data, the intensity of the magnetic Bragg peak (blue) and the contribution originating from critical scattering around T_c has been separated (red), providing an independent determination of the critical temperature T_c .

to the order parameter squared, follows a power law for the thermal phase transition at $H = 0$ T as well as for the QPT in an applied field along the c -axis (Fig. 4.40). By analysis of the peak shape in the raw diffraction data, it was possible to separate the critical scattering contribution to the integrated intensity from the pure magnetic Bragg peak (figure 4.40 inset). The divergence of the critical scattering signal provides a second independent determination of T_N and coincides with the onset of the order parameter. The extracted critical exponents are $\beta_T = 0.15 \pm 0.01$ and for the quantum phase transition $\beta_H = 0.33 \pm 0.01$, respectively, significantly deviating from the $\frac{1}{2}$ expected in the mean-field model.

4.4.2 Specific Heat

To further elucidate the nature of the (thermal) phase transition, specific heat as a function of temperature was measured for several fields (figure 4.41). Most pronounced is the anomaly marking the magnetic ordering transition, in good agreement with the phase diagram established with neutrons (figure 4.39f). Well above the magnetic ordering anomaly, the specific heat is dominated by the single ion crystal field and Zeeman terms in the single ion Hamiltonian, the phonon contribution and the magnetic interaction.

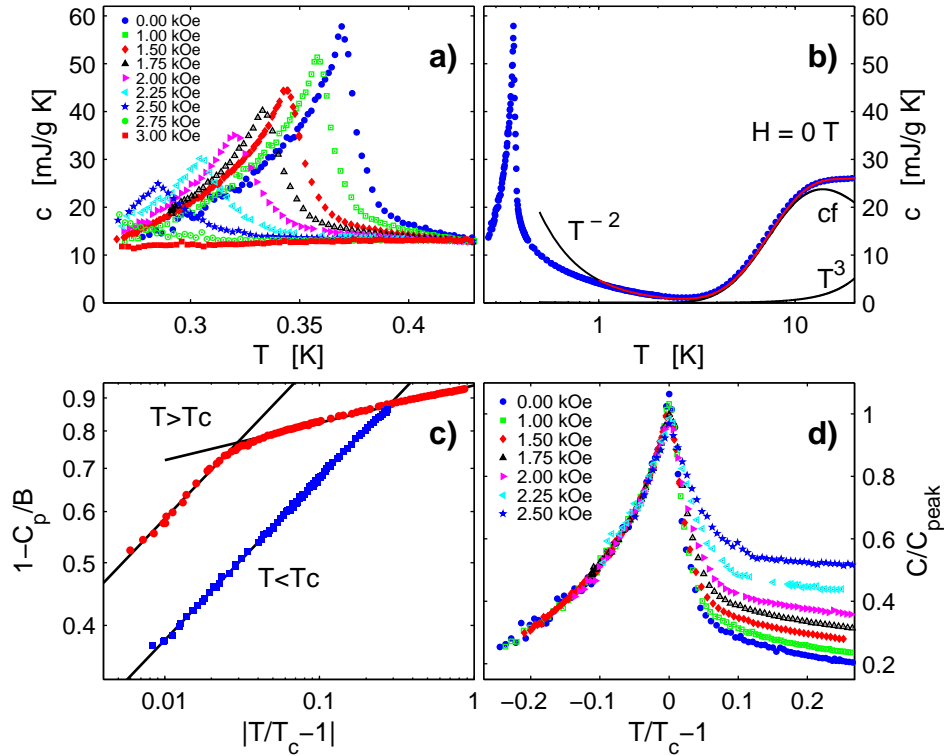


Figure 4.41: Specific heat as a function of temperature for several fields along the c -axis (a). The specific heat for temperatures well above the magnetic phase transition can be described by a simple model shown as red curve (b). It contains the crystal field Shottky anomaly, a phonon contribution T^3 and for the magnetic interactions in leading order of the high temperature expansion a βT^{-2} temperature dependence. Power law behavior of specific heat at $H = 0$ T and determination of critical exponents (c). Specific curves measured at different field values shifted to the same peak center and normalized by peak height to compare the evolution of peak shape (d). Below T_c the data collapse on a unique curve whereas above T_c the enhancement of the fluctuations closer to the QCP leads to an increase in the peak width.

The single-ion contribution can be calculated, and agree well with the data, further confirming the accuracy of our crystal field determination. Subtracting the crystal field contribution leaves a phonon contribution above 10 K scaling as ρT^3 , yielding $\rho = (6.6 \pm 0.1) \cdot 10^{-7}$ J/gK, significantly lower than reported in literature for LiReF₄[33], the reason being that in previous work the contribution from higher-lying crystal field levels was not subtracted before estimating the phononic term. Below 3 K, the specific heat increases due to interactions, which in a high-temperature expansion would follow to

leading order T^{-2} temperature dependence [33]. Most important for this study is a very pronounced tail above the ordering anomaly, which is much more pronounced than in the cases of LiHoF_4 and LiTbF_4 [33, 60, 61].

In the critical regime around the magnetic ordering anomaly, the specific heat was fitted by a universal power law dependence in the reduced temperature $t = T/T_c - 1$:

$$C_p = A|t|^{-\alpha} + B \quad t = T/T_c - 1 \quad (4.4.2)$$

for $T > T_c$ and a similar equation for $T < T_c$ with primed parameters. As a rule $\alpha = \alpha'$ must be satisfied, and satisfying the further constraint $B = B'$ a good fit was achieved simultaneously below the transition and above the transition, up to $t \simeq 0.03$. The best estimate for critical exponents are $\alpha = -0.29 \pm 0.04$. For $t > 0.03$ the curve tends towards a power law with much lower exponent $\alpha = -0.07 \pm 0.04$. Again, these critical parameters are substantially different from the mean-field result and the logarithmic corrections from renormalization group results that adequately describe the ferromagnetic Ising systems LiHoF_4 and LiTbF_4 . To emphasize the growth of the fluctuation regime as the quantum phase transition is approached, the $c_p(T)$ curves for different fields can be plotted on top of each others, scaling by peak height and peak temperature (figure 4.41 c). Below T_c there is a collapse to one unique curve, while above T_c a change in peak shape and a growth the critical tail is visible.

4.4.3 Order by Disorder

A possible way to understand both the ordered magnetic structure and the non-mean-field critical behavior is the phenomenon of order-from-disorder [62]. The meaning of this term is the following. Given a degenerate ground-state manifold, i.e. all the states have the same internal energy. At any nonzero temperature the quantity that is minimized is not the internal energy but rather the free energy. The states are favorable around which the largest phase space volume is accessible by thermal fluctuations. In other words, due to the existence of soft fluctuations the system predominantly afford time in exploring the vicinity of these states and gets effectively trapped. The entropy implies a selection of states in the degenerate energy manifold and induces an ordering transition.

On the mean-field level (i.e. neglecting fluctuations), there is in LiErF_4 a continuously degenerate ground-state manifold, which is obtained by rotating spins in adjacent layers of the BLAFM structure alternately clockwise and anti-clockwise by an angle ϕ . Nevertheless, in real material the symmetry is broken and the ordered structures where moments point along the a- or b-axis are selected, i.e. there is the restriction $\phi \in 0, \pi/2, \pi, 3\pi/2$.

Using a random-phase-approximation (RPA), the initial slope of the dispersions, and thereby the low-energy density of states as a function of ϕ . The slope is minimal and the low energy density of states maximal when the moments point along the a- or b-axis. As fluctuations suppress the ordering transition from the mean-field value, the fluctuating system will spend most of its time close to the $\phi = 0, \pi/2, \pi, 3\pi/2$ states, which lifts the degeneracy and selects these moment directions when ordering does set in. Indeed, this conclusion was also reached by Henley[63], who used second order perturbation theory to argue that order-from-disorder favors the co-linear ground states of isotropic dipolar coupled magnets on square, hexagonal and diamond lattices. Henley's work was inspired by reports of antiferromagnetic transitions at very low temperatures, 17 – 30 mK, in the susceptibility of $\text{RePO}_4(\text{MoO}_3)_{12} \cdot 30\text{H}_2\text{O}$, hosting Re=Er, Dy, Gd ions in a diamond lattice[64]. The tetragonal Scheelite lattice of LiErF₄ is in fact a distorted version of the diamond lattice and therefore Henley's argument remains valid also in this case. As conclusion order by disorder is causing a reduction to a four fold h_4 degeneracy.

4.4.4 Universality Class

As already pointed out the classical phase transition features unexpected critical exponents $\alpha = -0.28 \pm 0.04$ and $\beta = 0.15 \pm 0.02$, far beyond mean-field. For the classical, dipolar and quantum 3D Heisenberg model values $\alpha = -0.13$ to -0.198 are predicted and β falls into the range of 0.3 to 0.35 for all the common 3D universality classes. It has to be mentioned that random fields or multicritical points can affect significantly critical exponents. However no 3D model was found in literature with the observed combination of α and β . Further exponents that can be considered are δ , which reflects magnetization versus field, and the "anomalous dimension" η , which is associated with the spatial correlation function exactly at the critical point.

$$M \propto H^{\frac{1}{\delta}}, \quad \langle S_0 S_r \rangle \propto |r|^{d-2+\eta}. \quad (4.4.3)$$

The Rushbrooke $\alpha + 2\beta + \gamma = 2$, Widom $\gamma = \beta(\delta - 1)$ and the hyperscaling relations $2 - \alpha = d\nu$ and $\gamma = (2 - \eta)\nu$ imply finally

$$\delta = \frac{2 - \alpha}{\beta} - 1, \quad \eta = 2 - d \frac{\delta - 1}{\delta + 1}. \quad (4.4.4)$$

The fundamental exponents η and δ are super-universal depending only on the spatial dimension.

$$\begin{aligned}
\text{3D (Ising, XY, Heisenberg):} & \quad \delta = 4.7, & \eta = 0.03. \\
\text{2D (Ising, XY}/h_4\text{):} & \quad \delta = 15, & \eta = 0.25.
\end{aligned} \tag{4.4.5}$$

The determined value for LiErF_4 of $\delta = 15.2$ is very close the expectation for the 2D but again far away from the 3D case. Assuming 2D fluctuations yields $\eta = 0.26$, signaling strong fluctuations, consistent with the large reduction in transition temperature compared to the mean-field prediction.

The Mermin-Wagner theorem excludes long-range order in pure 2D XY models, but even infinitesimal h_4 anisotropy leads to conventional order slightly above the so-called Kosterlitz-Thouless transition. Weak h_4 anisotropy results in the effective exponents $\eta \simeq 0.35$ and $\beta \simeq 0.23$ [65], which quickly approach $\eta = 0.25$ and $\beta = 0.125$ on increasing h_4 . Indeed, for LiErF_4 not only δ and η but also the directly measured exponents agree with the 2D XY/ h_4 model. The value $\beta = 0.15$ suggests medium to strong h_4 anisotropy, and $\alpha = -0.28$ is consistent with a recent Monte-Carlo study on a bi-layer square lattice finding $\beta = 0.18 \pm 0.02$ and $\alpha \simeq -0.4$ [66]. It must therefore be concluded that the thermal transition in LiErF_4 belongs to the 2D XY/ h_4 universality class, the effective dimensional reduction likely being due to the frustrated nature of the dipolar coupling [59].

4.4.5 Magnetic Correlations

A phase transition from a disordered to an ordered magnetic state is in general accompanied by critical scattering. To investigate this diffuse scattering in neutron diffraction is more challenging than measuring the onset of the magnetic Bragg peak, because the rather weak intensity is outspread over a certain region in reciprocal space. In LiHoF_4 in contrast to the thermal phase transition at $T=T_c$ in the case of the quantum phase transition only a weak quasi elastic scattering was observable. However for LiErF_4 there is a measurable signal also around H_c .

The experiment has been performed on the RITAI spectrometer at SINQ, the sample oriented with c-axis perpendicular to the scattering plane. The field was applied along the c-axis. The analyzer was fixed on the elastic position during the whole experiment, since due to the low energy scale in the system it is impossible to further resolve the dynamical structure of the critical scattering anyway. This implies that the detected signal is effectively integrated over energy. But nevertheless the use of the instrument with the analyzer instead of a simple diffraction setting improved the signal to noise ratio. That this is a crucial point for the feasibility of the experiment was highlighted by previous unsuccessful attempts on several diffractometers.

The critical scattering in LiErF_4 is located around the magnetic Bragg peaks equivalent to (100). Although highly anisotropic the intensity distribution

over the reciprocal space does not show a characteristic butterfly like shape in contrast to the ferromagnetic compound Li(HoY)F₄. In the scattering plane ($hk0$) the momentum dependence of the signal can be described by a Lorentzian model. For example around $\mathbf{q}^* = (100)$, the width is broad along the ($h00$) and narrow along the ($0k0$) axis. The full anisotropy in reciprocal space was mapped out at $H = 3.4$ kOe slightly above the critical field of $H_c = 3.05$ kOe, see figure 4.42. This anisotropy seems to be independent of the applied field, as seen in further scans along the Q_h and Q_k direction. The data can be described approximatively by the phenomenologically model

$$\chi(\mathbf{Q}) \propto \frac{1}{\Gamma^2 + g^2 q_h^2 + q_k^2}, \quad (4.4.6)$$

with $\mathbf{q} = \mathbf{Q} - \mathbf{q}^*$, where \mathbf{Q} denotes the scattering vector. The anisotropy factor is roughly $1/g = 2$ to 3 . Unfortunately there is no appropriate theoretical predictions specific to the case of LiErF₄ which would allow a more conclusive evaluation. The available data itself is also too inaccurate to predict and verify directly such a sophisticated model.

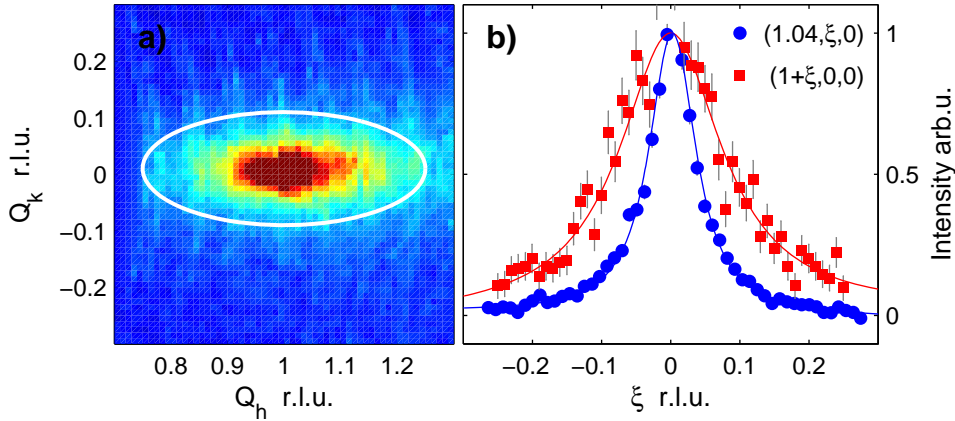


Figure 4.42: Anisotropy of critical scattering in reciprocal space. (a) Pseudocolor map of neutron scattering intensity at $H = 3.4$ kOe. The white ellipse with aspect ratio of 2.5 is plotted to visualize the anisotropy. (b) Scans in perpendicular directions to each other, normalized to peak height.

The width of the critical scattering is related to the reciprocal of the correlation length. Towards the phase transition the correlation length ξ diverges, hence the width of the peak tends to zero and the scattering intensity diverges. The experimentally investigated evolution of the critical scattering as function of the field at fixed temperature is summarized in figure 4.43. The scans have been performed slightly off the Bragg peak (100) in Q_k direction. The data is fitted with a Lorentzian line shape folded with a Gaussian to

incorporate correctly the finite instrumental resolution. The intrinsic width clearly decreases towards the phase transition, but the peak did not get resolution limited. Of course in the scans there is a small offset in Q_h which was chosen to circumvent in the signal the contamination from the Bragg peak. Taking into account this offset, by considering also the anisotropy, the determined nonzero width at H_c can be reproduced, at least approximatively. Therefore the hypothetical scan exactly through \mathbf{q}^* would indeed provide a vanishing width and diverging intensity, as expected. Unfortunately the data quality and the uncertainty in the model for the peak shape does not allow to extract the critical exponent ν of the correlation length ξ in trustworthy way. Nevertheless in panel (c) of figure 4.43 the integrated intensity is depicted in a log-log scale. Over a certain range there is indeed a power law like field dependence, but close to H_c there are defective deviations, i.e. the uncontrolled inaccuracies start to matter.

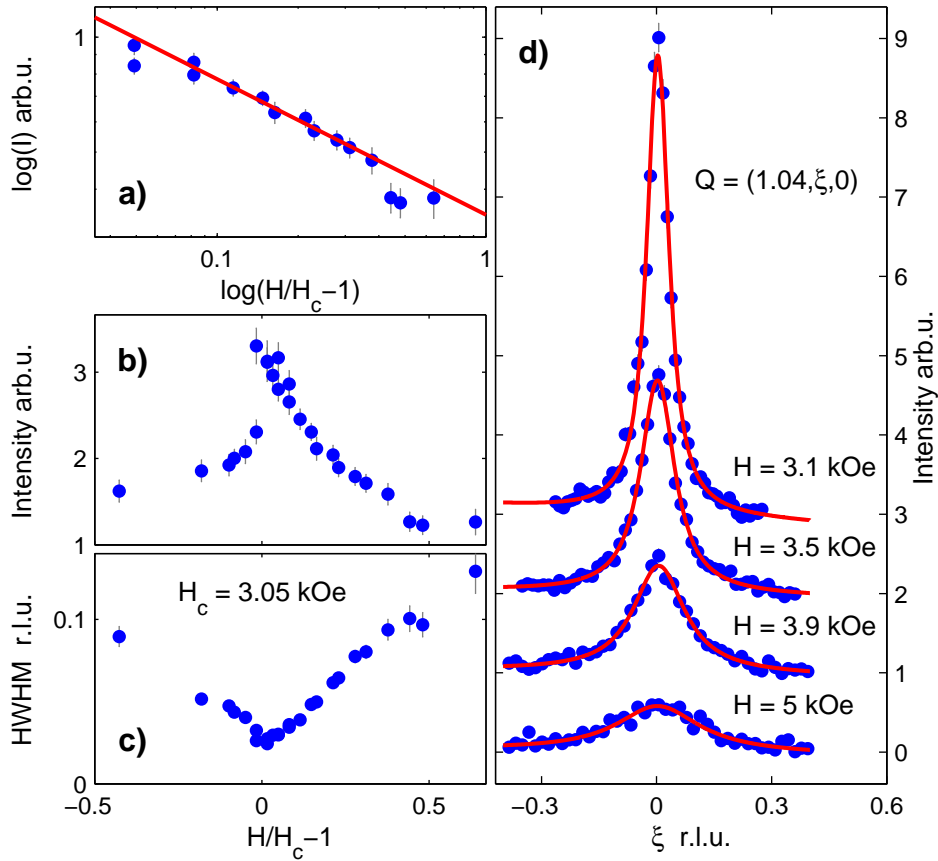


Figure 4.43: Elastic scans along $\mathbf{Q} = (1.04, \xi, 0)$ at a series of applied field values and at constant temperature.

Summary 4.4:

In this chapter a investigation of the phase diagram of LiErF₄ by means of neutron diffraction and specific heat measurements was presented. Below a short summary of the main results:

- LiErF₄ exhibit bilayered antiferromagnetic ordering below $T_N = 373 \pm 5$ mK.
- In a field applied along the c-axis the system undergoes a quantum phase transition at $H_{c\parallel} = 4.03 \pm 0.02$ kOe.
- The critical exponents α and β have been determined.
- Thermal phase transition in LiErF₄ belongs to the universality class of the XY/h₄ model in 2 dimensions, i.e. a dimensional reduction takes place.
- The fourfold anisotropy in the ordered phase originate from order-by-disorder.

4.5 LiErF₄ - Excitations and Critical Dynamics

In LiHoF₄ the weak hyperfine coupling to the nuclear spins has dramatic effect on the quantum phase transition. A QPT should be accompanied by softening of the characteristic excitation, but in LiHoF₄ the magnetic excitation of the electronic subsystem remains gapped due to coupling to the nuclear spin bath. Details are discussed in chapter 4.3. Unfortunately it is not possible to substitute Ho isotopes without nuclear spins, since only one stable isotope exists. In Er the hyperfine coupling constant is weaker than in for LiHoF₄ and only 20% of the natural occurring isotopes have a nuclear spin at all. Therefore one central question in LiErF₄ is the existence of a soft mode at QPT.

4.5.1 Excitations in the ordered phase at $H = 0$ T

The dispersions along the high symmetry directions of the crystal has been measured in zerofield as well as in the quantum disordered phase, i.e. a field of 1.5 T along the c-axis or 1 T along the a-axis respectively. In the zerofield investigation we measured along (h0l) for $l = 0, 1, 1.5, 2$ fixed and different h on TASP but also along (10l) and (00l) on PANDA. Because of the limited instrumental resolution the spectra are smeared out and it was only in particular cases possible to distinguish and fit discrete modes. The dispersion along (h00) could be determined assuming a damped harmonic oscillator model, see figure 4.44. Remarkably, the spectrum is gapped at zone center. The RPA calculation is able to predict the correct slope of the dispersion but underestimates the gap by a factor of two. Furthermore, all measured data have been evaluated using the calculated RPA excitation spectra convoluted with the experimental resolution as a model. Examples of this fits are depicted in figure 4.45&4.46. The light blue area under the fitting curve represents the magnetic signal, the yellow the contribution of incoherent scattering, which could be determined from the energy scans in the high field phase. At some points in reciprocal space in addition to that also a quasi elastic contribution has to be included in the model. This contribution can be interpreted as a phenomenological correction for the neglected fluctuations in the RPA model. The two equivalent domains of the magnetic structure has also to be considered in the RPA calculations for the magnetic excitations. In zero field equal population is expected. The contributions originating from the two different domains are indicated in Fig. 4.45 by white lines. The agreement of the fit with the data is a direct manifestation of two domain model. Hence it is an independent evidence for the correctness of the underlying magnetic structure.

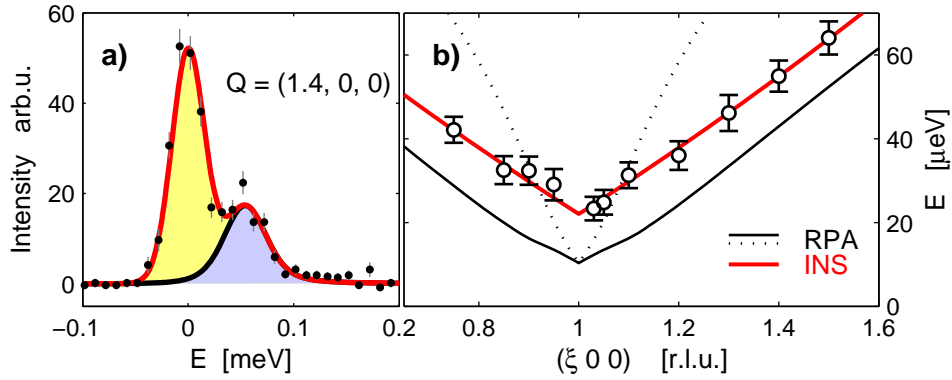


Figure 4.44: Dispersion relation at $H = 0$ T in the ordered phase of LiErF₄ along the high symmetry direction $q = (h00)$. At zone center $q = (100)$ the spectra is gaped and shows an almost linear dispersion-relation. The red solid corresponds to an phenomenological polynomial approximation to the dispersion extracted from the data using a simple damped harmonic oscillator model. The black curves are the two modes obtained in an RPA-Calculation for two possible domains, but only the mode depicted as a solid line has a significant contribution to the scattering intensity. The RPA-calculation is able to predict the dispersion-relation but underestimates the gap of the spectra.

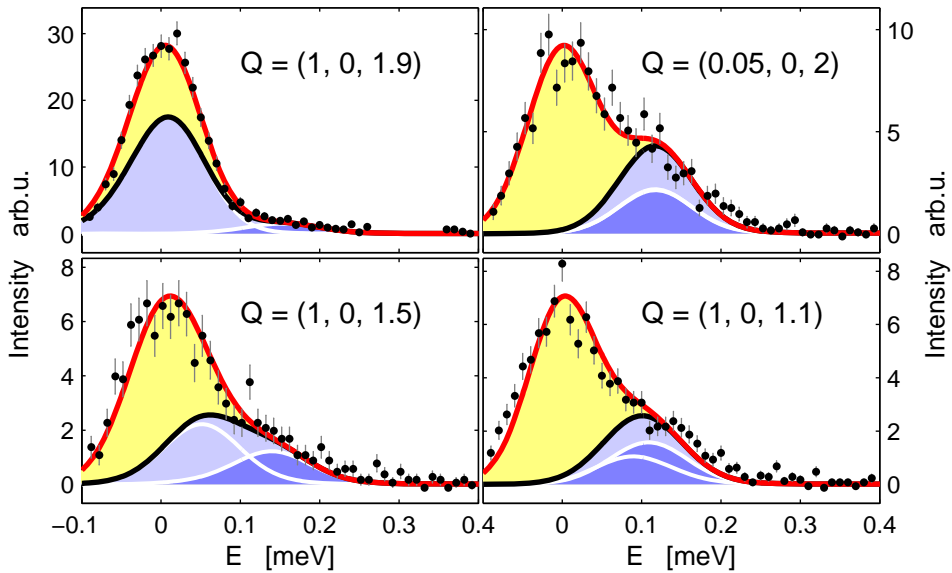


Figure 4.45: Excitations in the ordered phase at $H = 0$ T at selected points in reciprocal space. The fitted curve is the prediction from RPA-calculation assuming a two domain model in the magnetic structure as described in the text.

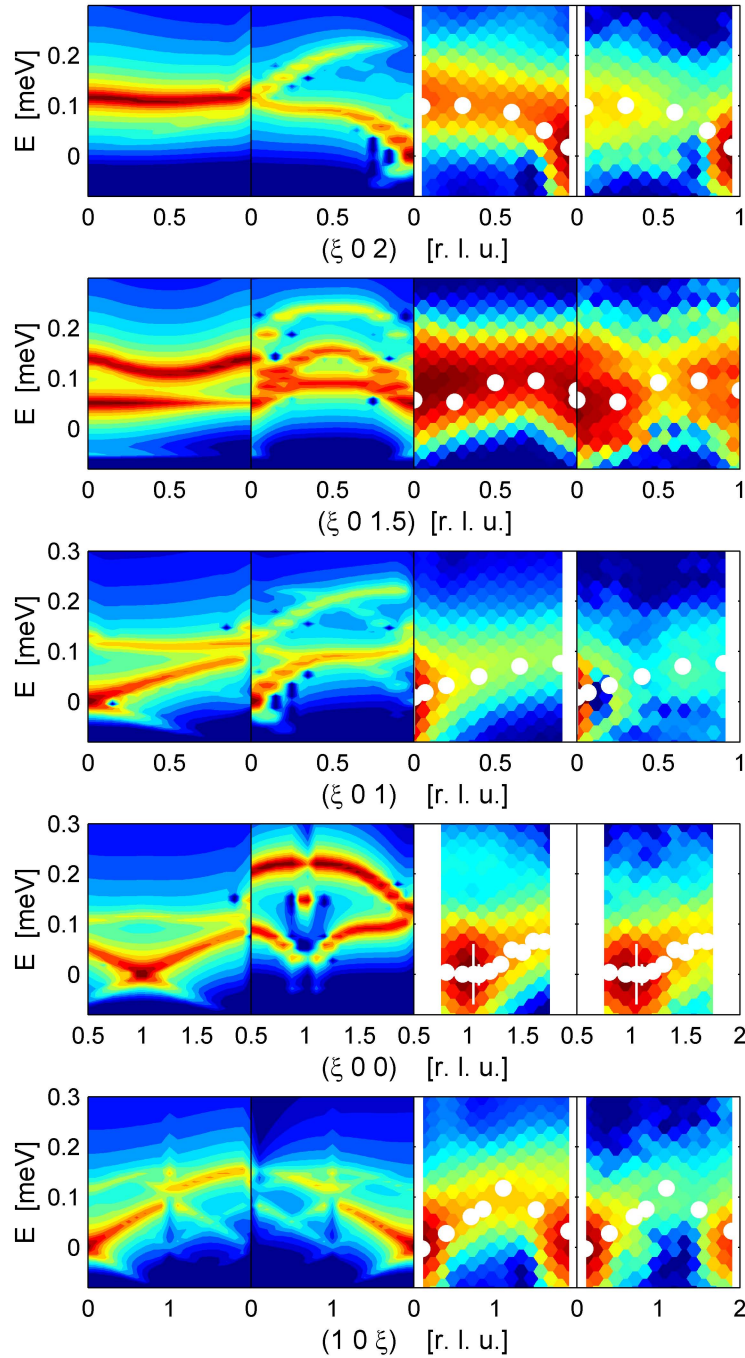


Figure 4.46: Excitation spectra in the ordered phase along selected directions in reciprocal space. From left to right the two first panels represent the RPA-Calculated spectra for the two different domains, the third is the sum of the latter two convoluted with the experimental Resolution and in the outer right panel the measured data subtracted by the incoherent line is depicted. The white points corresponds to the dispersion obtained by a fit to the data with a one mode damped harmonic oscillator model.

4.5.2 Excitations in the phase above H_c

Applying a field the dispersion is lifted to higher energies and the inelastic signal can be separated from the incoherent line. On the other hand are fluctuations in the polarized higher field phase less pronounced than close to the antiferromagnetic ordered region. Therefore MF/RPA can be regarded as a reliable first approximation to describe the excitation spectra, see figure 4.47. Although due to the limited achievable resolution it is not possible to distinguish directly from the data all details in the excitation spectra, a correspondence of experiment and calculation is confirmed. This opens the opportunity to refine the last unknown parameter in the Hamiltonian, the exchange coupling constant. In Figure 4.48 the data is compared with the RPA spectra calculated for different values of \mathcal{J}_{ex} , ranging from -0.3 up to $0.3 \mu\text{eV}$. The coupling constant not only changes the dispersion but also influences the meanfield and therefore the single ion splitting. To get rid of this influence an energy offset is included in the fit. From the refinement based on the measured dispersion relation and the RPA calculation, it can be concluded that the exchange interaction is negligible compare to the dominant dipole-dipole coupling. A strong exchange coupling constant $|J_{ex}| > 0.1 \mu\text{eV}$ would induce a further separation of the two modes in the spectra along $Q=(001)$, see for example figure 4.47. In particular a split-

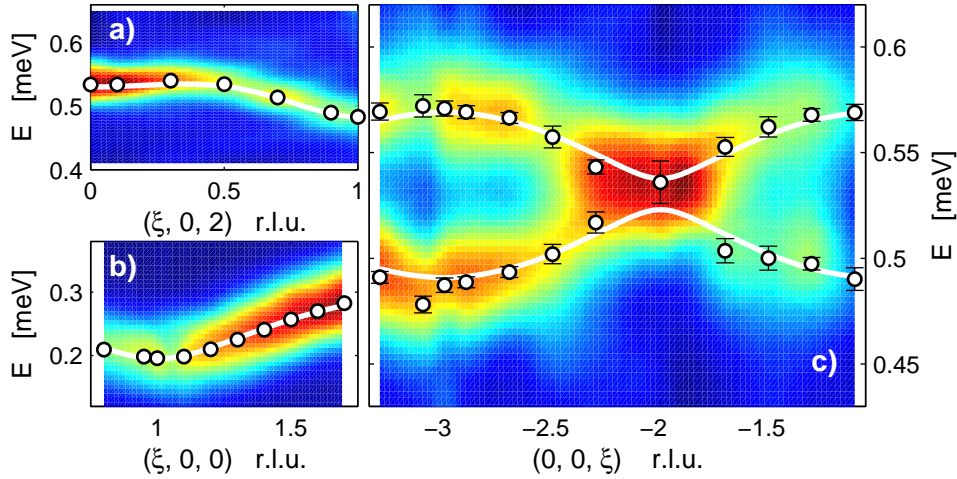


Figure 4.47: Excitation spectra of LiErF₄ in the high field (paramagnetic) phase above the QPT. The applied field is either $H_{\parallel a} = 1.0$ T, as in panel (a) and (c), or $H_{\parallel c} = 1.5$ T in (b). The absence of a distinct splitting at zone boundary $q = (00\bar{2})$ within experimental resolution, indicates that the so far unknown exchange coupling constant is orders of magnitudes lower than the dominant dipole-dipole coupling.

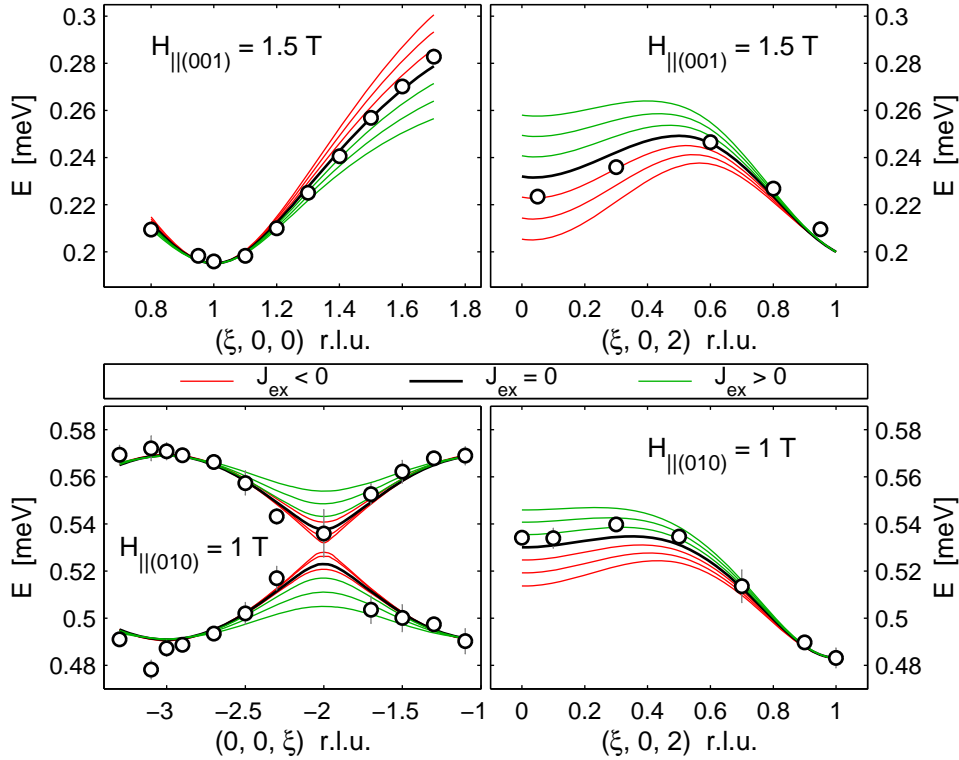


Figure 4.48: Dispersions in the high field phase in comparison to the RPA spectra calculated for distinct values of J_{ex} ranging from -0.3 to $0.3 \mu\text{eV}$. The applied field and its direction is indicated. To visualize the effect of varying J_{ex} , the calculated spectra are shifted by a fixed energy offset as described in the text.

ting at the zone boundary would be expected. But inside the experimentally achievable resolution, the two modes at $q = (00\bar{2})$ are almost degenerated (figures 4.48&4.47). In the full refinement based on the measured dispersions along four selected directions in reciprocal space, for the exchange coupling a value of $J_{ex} = 0.0 \pm 0.1 \mu\text{eV}$ has been obtained. Therefore, the dipole-dipole coupling is the dominant and only significant interaction in the model of LiErF_4 .

4.5.3 Softmodes at QPT

The most remarkable result of this inelastic neutron scattering investigation is the demonstration of the complete softening of the characteristic excitations at the QCP. This is the hallmark of a quantum phase transition, and in the case of LiErF_4 this is even expected from a simple RPA point of

view. Within the experimental resolution the gap is closing when the field is approaching its critical value, i.e. at the quantum phase transition. This was demonstrated in both configurations, in a field applied along the c-axis (figure 4.49) as well as along the a-axis (figure 4.50).

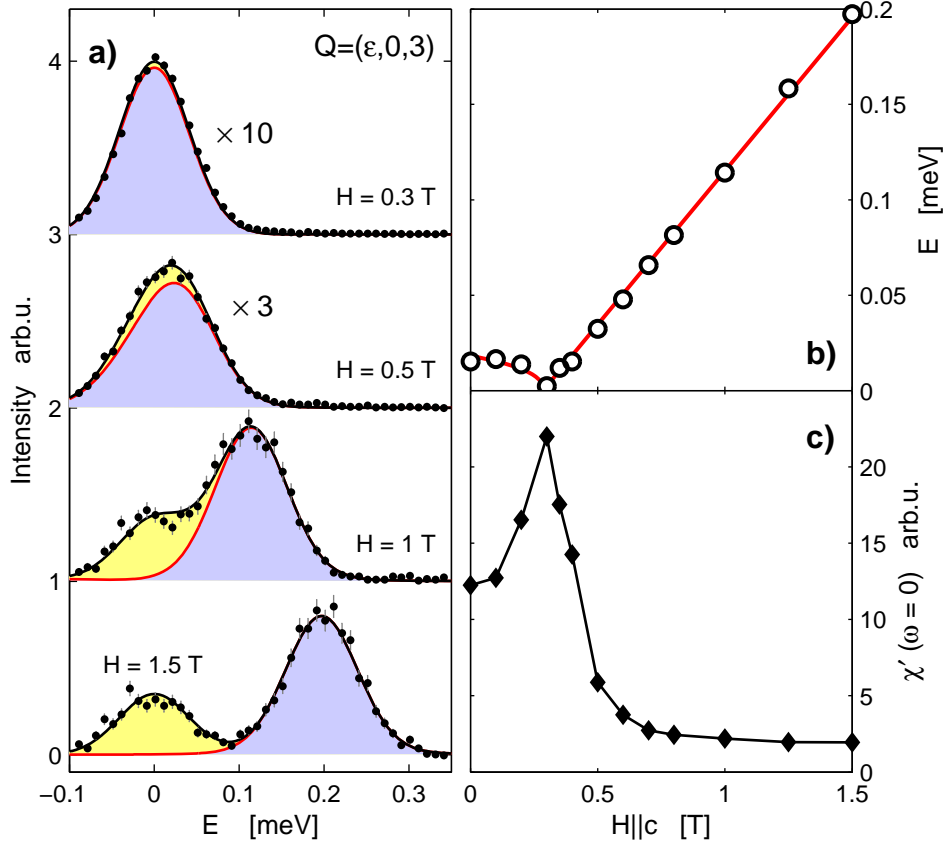


Figure 4.49: Softening of the characteristic excitation around the QCP in LiErF₄ applying a field along the crystallographic c-axis. (a) Energy scans at $Q = (0.05, 0, 3)$ at different field values. The solid line fits to a damped harmonic oscillator model (blue) adding a fixed contribution for the incoherent scattering (yellow) measured at higher field phase. (b) the energies of the critical mode extracted from the data as a function of the applied field tends to zero reaching the QPT. As expected for a softmode the scattering intensity, i.e. χ' , diverges.

The excitation energy was determined fitting the data to a damped harmonic oscillator model. To correct for the incoherent scattering contribution, scans at higher field can taken into account, where all the inelastic magnetic signal is lifted to higher energies. The excitations are sharp compared to the in-

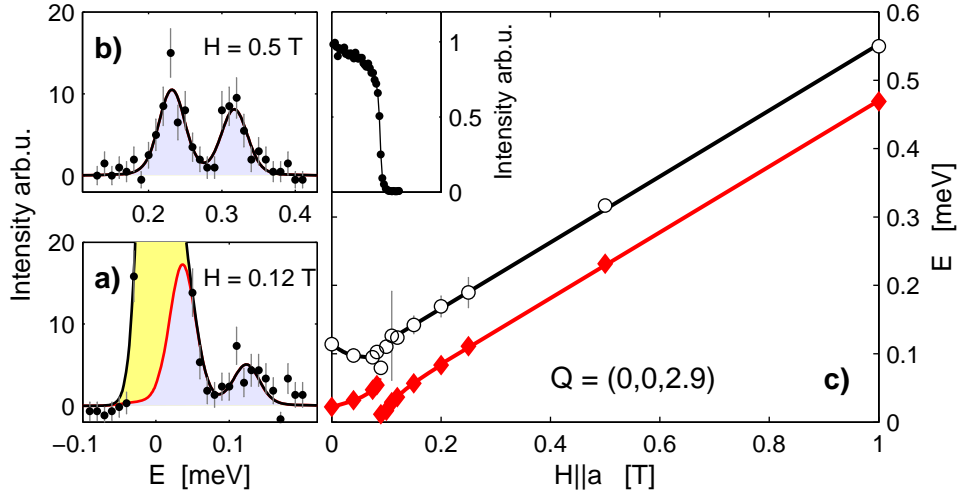


Figure 4.50: Softening of the characteristic excitation around the QCP in LiErF_4 applying a field along the crystallographic a-axis. (a-b) Energy scans at $Q = (003 + \epsilon)$ at different field values. The solid lines represent fits to a two mode damped harmonic oscillator model (blue area) adding a fixed contribution for the incoherent scattering (yellow area) measured at higher field phase. (c) Energies of the two modes extracted from the data as a function of the applied field. Inset: Onset of the magnetic Bragg peak (003) at QCP. The critical field extracted from the ordering parameter corresponds to the field where the critical mode becomes soft.

strumental resolution and there is no significant broadening of the line width as a function of the field either. A fit assuming infinite sharp excitations instead of a damped harmonic oscillator model provides a comparable result. At the QCP the softening of the characteristic modes is accompanied by a divergence of the scattering intensity, see figure 4.49. Formally the quantity of interest is the generalized susceptibility $\chi'(\omega = 0, \vec{q})$. This value can in principle be calculated from the fitted parameters of the damped harmonic oscillator model. Unfortunately in the interesting region where the energy approaches zero, the result is highly affected by the uncertainties of the experiment and the data evaluation. A more rigid value is the integrated intensity which can be determined by numerical integration of the data. In the present experimental configuration and due to the flat dispersion $\mathcal{S}(\omega, \mathbf{q})$ can be considered constant in \mathbf{q} over the range affected by the resolution. Therefore within this approximation the resolution function integrates out in the following expression for the intensity integrated over energy.

$$I_{\text{int.}} = \int_{-\infty}^{\infty} I(\omega) d\omega \propto \int_{-\infty}^{\infty} \frac{1}{1 - e^{-\beta\hbar\omega}} \chi''(\mathbf{Q}, \omega) d\omega. \quad (4.5.1)$$

Assuming a sharp excitation with energy ω_q and recall Kraemers Kronig relation the integrated intensity $I_{\text{int.}}(\mathbf{q})$ is proportional to $\chi'(\omega = 0, \mathbf{q}) \cdot \omega_q$. In figure 4.49 the field dependence of the excitation energy and χ' at zone center is depicted.

4.5.4 Conclusions

In summary a comprehensive inelastic neutron scattering investigation of the dipolar coupled quantum antiferromagnet LiErF₄ has been presented. A meanfield-RPA model is able to predict the excitation-spectra in the ordered as well as the paramagnetic high field phase within the limits of the approximation and the experimental achievable resolution. The refinement of the interactions constant proofs that the system is dominated by dipolar coupling. As the most remarkable result the existence of a softmode at the QPT can be confirmed. LiErF₄ can be regarded as a much cleaner realization of a quantum critical system as LiHoF₄, due to the fact that the quantum phase transition is not affected by secondary degrees of freedom like hyperfine interaction to the nuclear spins.

Summary 4.5:

In this chapter a neutron spectroscopy investigation of the magnetic excitations in the compound LiErF₄ was presented. Below a short summary of the main results:

- The excitations in the ordered phase were measured along high symmetry directions in the ordered phase. Within the limited experimental resolution the spectra are qualitatively close to the RPA prediction. However, in the experimental data a gap of around 20 μeV at $H = 0$ T is indicated.
- In the disordered high field phase the spectra is lifted towards higher energies. The determined dispersion relation is in agreement with the RPA prediction up to a certain global scaling factor. The refinement based on the measured dispersion states that the exchange coupling is at least two orders of magnitude smaller than the dominant dipolar interaction.
- As a hallmark of the quantum phase transition there exist a soft-mode in the characteristic excitations at the QCP.

4.6 $\text{LiHo}_x\text{Er}_{1-x}\text{F}_4$

The mixture of two or more different rare-earth ions in LiReF_4 enhances the range of possibilities in tuning the magnetic properties of the material, instead of the so far considered doping with nonmagnetic Yttrium. Remarkably there are no investigations about the magnetic behavior of any of these dilution series reported in literature, as far as we knew. Furthermore, the recent discussion about off-diagonal coupling effects in $\text{LiHo}_x\text{Y}_{1-x}\text{F}_4$ [10, 27, 29] promotes the idea for a new realization of a random field magnet by means of doping with Erbium ions instead of Yttrium. Because of the planar xy-anisotropy in LiErF_4 , the Erbium moments in $\text{LiHo}_x\text{Er}_{1-x}\text{F}_4$ will be coupled to the Ising like Holmium moments mainly through the off-diagonal components of the dipole interaction. It is assumed that Er will be more efficient than Yttrium to enhance the off-diagonal coupling effects such that the system exhibits already at low dilution concentrations a crossover to a spin-glass like phase. The non-percolation-like dilution may have the further advantage to circumvent lower energy scales and spatial decoupling as in the case $\text{LiHo}_x\text{Y}_{1-x}\text{F}_4$, making the $\text{LiHo}_x\text{Er}_{1-x}\text{F}_4$ compounds better suitable for experimental investigations.

Several compounds with different dilution concentrations have been recently characterized by means of ac-susceptibility at Laboratory for Quantum Magnetism EPFL [67]. In the following the phase diagram will be discussed. For the particular representant $\text{LiHo}_{0.25}\text{Er}_{0.75}\text{F}_4$ the presence of strong antiferromagnetic correlations in absence of long range order was demonstrated by a neutron scattering investigation combined with an insitu susceptibility measurement. Nevertheless the performed studies are only a first glimpse on the physics of $\text{LiHo}_x\text{Y}_{1-x}\text{F}_4$ and still far away from a final conclusive picture.

4.6.1 Phase Diagram

Starting from the pure compound LiHoF_4 and introducing a marginal concentration of Er-ions has mainly the effect of suppressing T_c , whereas long range ferromagnetic ordering is not affected. This is indicated in the compound $x = 0.8$ by the frequency independence of the temperature T_f which is denoting the position of the peak in susceptibility χ' . In contrast, for the more diluted compounds, explicit $x = 0.5$, $x = 0.3$ and $x = 0.2$, the peak in χ' shifts towards higher temperatures for increasing frequency. From the frequency dependence of T_f it can be assumed that in these compounds the system enters either a superparamagnetic or a spin glass like phase.

The phase diagram of $\text{LiHo}_x\text{Y}_{1-x}\text{F}_4$ theoretically expected from a simple virtual-crystal (VC) meanfield calculation (see paragraph 3.3) is shown in

figure 4.51. In this model, below a certain critical temperature T^* the Erbium or Holmium subsystem tends to align and exhibits long range ordering. Remarkably there exists also a region of coexistence in the phase diagram where both types of ions align. Although VC-meanfield could never be an adequate framework to reproduce glassiness, the calculated phase boundary line is close to the measured T_f over the whole range of x . It is not surprising that the calculation overestimates T_f , because the effect of randomness is not considered adequately. Therefore, the deviation increase as one moves in the phase diagram further away from the pure compounds.

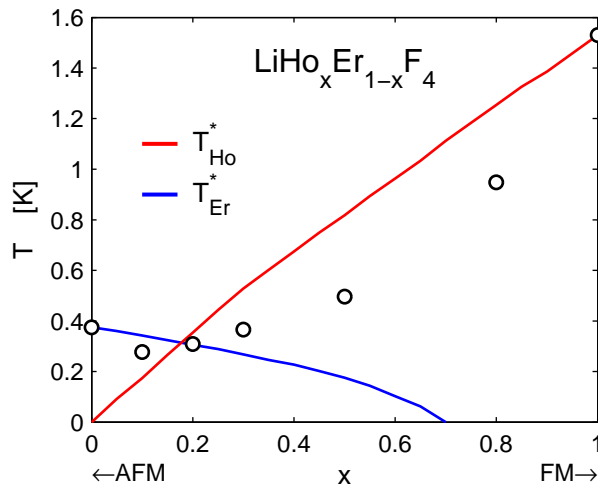


Figure 4.51: Phase diagram calculated via virtual-crystal meanfield approximation. T_{Ho}^* and T_{Er}^* denotes the critical temperatures, where the Holmium respectively, Erbium moments aligne. Both temperatures are scaled such that they match T_c in the case of the pure compounds. The measured crossover temperatures T_f by means of ac-susceptibility at $f = 990$ Hz [67] are reduced compared to the expected T^* .

4.6.2 Magnetic Correlations in LiHo_{0.25}Er_{0.75}F₄

In the scans around the points in reciprocal space related to ferromagnetism no significant magnetic signal was observed neither in form of diffuse nor in form of Bragg scattering down to temperatures of 170 mK. The small changes in Bragg peak intensity on top of the strong nuclear scattering contribution, found in a comparison of measurements at different fields and temperatures was unfortunately only within the statistical error bars. Furthermore, one has to be aware of possible systematic perturbations, like positioning errors in consecutive runs or field induced shifts in the sample

position, that could cause such small changes in intensity. Based on the available data one must conclude that ferromagnetic ordering, long range as well as short range, is unlikely.

Around the points in reciprocal space related to antiferromagnetism, e.g. $Q = (100)$, a strong diffuse magnetic scattering signal could be observed (figure 4.52). The correlation length estimated from a Lorentzian fit is $\xi = (3.9 \pm 0.1) \text{ \AA}$ at $T = 170 \text{ mK}$. In a field applied perpendicular to the scattering plane, i.e. along the crystallographic y -axis, the peak-intensity of the scattering signal decreases continuously and vanishes at fields around 0.7 T completely. As a function of temperature there is no sharp transition visible in the signal, instead the intensity varies continuously and persists marginally even beyond the critical temperature T_N of the pure compound LiErF_4 . Hence $\text{LiHo}_{0.25}\text{Er}_{0.75}\text{F}_4$ exhibits a crossover to a disordered phase with short range antiferromagnetic correlations. Furthermore the correlation length is decreasing as a function of increasing field or temperature. So far it is a point of speculation if true long range antiferromagnetic order may establish in the limit of zero temperature.

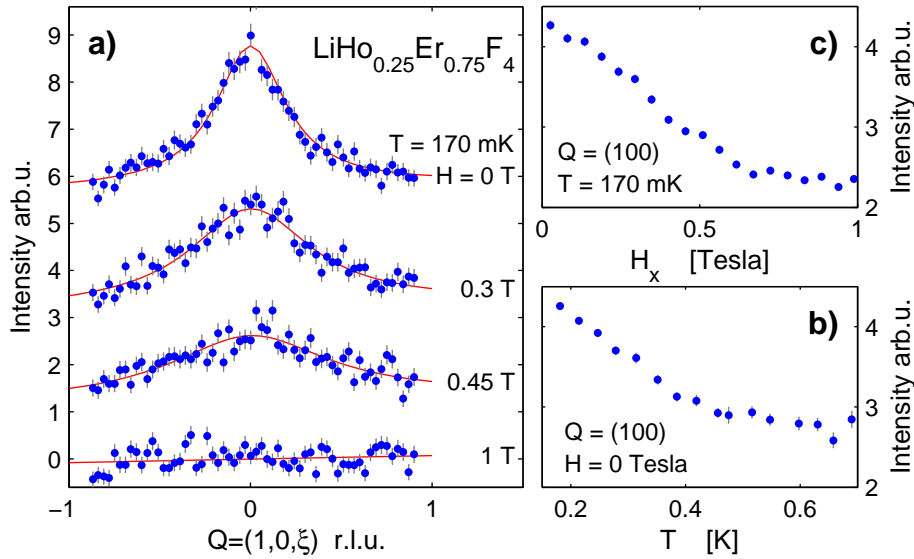


Figure 4.52: Antiferromagnetic Correlations around $Q=(100)$ in $\text{LiHo}_{0.25}\text{Er}_{0.75}\text{F}_4$. a) Reciprocal space scans at different applied fields in plane and corresponding Lorentzian fits. b,c) Peak intensity of the correlations as a function field and temperature.

Summary 4.6:

In this chapter a first preliminary study on the mixed Li(HoEr)F₄ was presented. Below a short summary of the main results:

- The ac-susceptibility data implies for LiHo_xEr_{1-x}F₄ $x = 0.8$ conventional ferromagnetic order, whereas for the more diluted compounds $x = 0.5$, $x = 0.3$ and $x = 0.2$, spin glass like or superparamagnetic behavior was observed.
- The phase diagram of LiHo_xEr_{1-x}F₄ was calculated by means of a virtual-crystal meanfield approximation.
- Neither long range order nor ferromagnetic correlations were observed in a neutron diffraction investigation of LiHo_{0.25}Er_{0.75}F₄. Instead the system exhibit a crossover to a disordered phase with short range antiferromagnetic correlations.

Chapter 5

Conclusions and Outlook

The compounds of the LiReF_4 -series (Re=rare earth) providing several simple model systems, where experimental observations can be compared quantitatively with theoretical predictions. These compounds host a rich variety of collective phenomena and quantum effects. The understanding of such model systems may also generate an important contribution to the wider field of quantum phase transitions and spin glasses. In this thesis a number of new experimental results have been achieved for different LiReF_4 compounds, mainly by means of neutron diffraction and spectroscopy.

LiHoF_4 is a physical realization of a transverse field Ising model. However, the real system turned out to be more complicated, the marginal hyperfine coupling to the nuclear spins intersects the quantum phase transition. Hence, LiHoF_4 offering an ideal system to study in a controlled way the robustness of quantum criticality in non-perfect (hence realistic) systems. Instead of a true softmode at the QPT, the excitations of the electronic subsystem remain gapped. This was interpreted as a decoherence effect due to coupling to the nuclear spin bath, i.e. a local environment that is constituted from secondary degrees of freedom. Raising the temperature the coupling to the spin bath weakens due to thermal fluctuations. Based on the measured excitation spectra, one can conclude that the minimal, effective model to describe comprehensively the LiHoF_4 system is the transverse field Ising model in a longitudinal random field.

By dilution with nonmagnetic yttrium $\text{Li}(\text{HoY})\text{F}_4$ evolve from a long range ordered Ising ferromagnet to a random field magnet and a spin glass. Many experimentally observed effects are referred as 'quantum', but in our understanding at least some aspects of $\text{Li}(\text{HoY})\text{F}_4$ are consistent with a classical or semi-classical picture. The system is thoroughly investigated and particularly well understood, although there exist some discrepancies in the reported experimental results and a vivid theoretical dispute about modeling issues. However, there is a general agreement about the importance

of random fields induced by off-diagonal terms in the dipolar coupling. In this thesis the first extensive neutron scattering investigation of $\text{Li}(\text{HoY})\text{F}_4$ versus transverse field was presented. One of the most remarkable findings was the microscopic insight into the history dependence behaviour found in the compounds $\text{LiHo}_x\text{Y}_{1-x}\text{F}_4$, $x = 0.33$ and $x = 0.46$. Following a zero field cooling protocol one can prepare the system in the ferromagnetic state, whereas cooling in an applied transversal field leads to a disordered short range correlated state. However, an earlier dynamic susceptibility spectroscopy study draw the contrary conclusion. Therein the field cooling path, or the quantum annealing, was interpreted as more efficient in establishing the ground state.

LiErF_4 is a realization of a planar antiferromagnet that exhibits layered ordering and undergoes a quantum phase transition in a magnetic field. Remarkably, the system shows a complete softening of the characteristic excitations when approaching the critical field, regarded as one of the hallmarks of a quantum phase transition. Furthermore, as a conclusion drawn from the critical exponents, the thermal phase transition falls into the 2D universality class XY/h_4 , implying that dimensional reduction takes place. The emergence of symmetry breaking is interpreted as a consequence of the effect referred as “order-by-disorder”. As a further project in LiErF_4 an additional specific heat investigation around the QCP is planned. Based on the so far available neutron scattering data, we suggest that the critical exponents will be consistent with a classical 3D universality class. This expectation is in accordance to the rule that the problem of a QPT in a d -dimensional system can be transformed on a $d+1$ dimensional classical system. A second further project will be the investigation of the scaling behaviour of the quantum fluctuations in the quantum critical regime. The intention is to verify universal ω/T -scaling at the critical field as well as the non-universal ω/T -scaling away from the critical field. However, these measurements are experimentally rather ambitious, because of the limited resolution achievable in inelastic neutron.

Considering the fact that the most regarded studies about LiReF_4 are related the diluted compounds $\text{Li}(\text{HoY})\text{F}_4$, one can assume that there must exist also promising collective quantum effects in other $\text{Li}(\text{ReY})\text{F}_4$ systems, for example $\text{Re}=\text{Er}$. Also the mixture of two or more different rare-earth ions may enhances the range of possibilities in tuning the magnetic properties of the material. In this thesis already a first preliminary study on $\text{Li}(\text{HoEr})\text{F}_4$ was presented.

Furthermore, there exists the vision to realize sophisticated pump-probe experiments on LiReF_4 compounds. This would be a step forward beyond the level of simple characterization and explanation of a given material towards actively manipulating and controlling the system, also outside of

equilibrium. One example presented in this thesis was the time resolved SANS experiment to observe coherent oscillating spin clusters. A further project, already mentioned in a previous chapter, is the NMR experiment in LiHoF_4 , which aims to control the coupling strength of the spin bath with the electronic subsystem. Only the simplicity of LiReF_4 and the fact that the physics of these systems is well investigated and characterized make such experiments feasible. Nevertheless, the realization of in-situ experiments is more complicated than it seems on the first glance, because it involves the combination of several technics on a high-end level and under extreme conditions.

One of the most challenging open issues for further projects is the theoretical description of the experimentally observed phenomena and a verification of the preliminary descriptive interpretations. The new neutron scattering results and the reported susceptibility data should be combined to more sophisticated, comprehensive picture. A sophisticated theory beyond mean-field/RPA would be also desirable, because it may promote new ideas for further experimental projects.

Appendix

A Crystallographic Details of LiReF_4

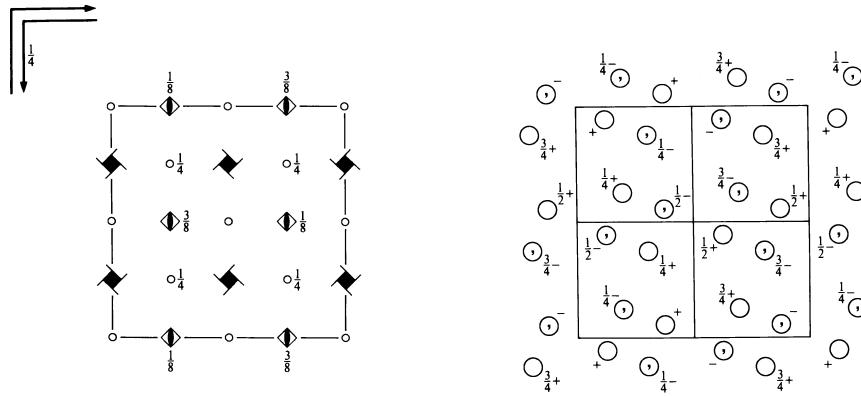


Figure A.1: Symmetries of space group $I4_1/a$ as given the International Tables of Crystallography (no. 88, choice 2) [68]. The symbols correspond to the symmetry operations, the notation is explained in [68].

The positions of the ions within the unit cell of LiReF_4 are listed in table A.1. The asymmetric unit, which defines the position of the fluorine ions, has to fulfill the general restrictions

$$0 \leq x \leq \frac{1}{4}, \quad 0 \leq y \leq \frac{1}{4}, \quad 0 \leq z \leq 1.$$

In case of LiReF_4 the values for the asymmetric unit are reported for the particular compound $\text{LiTb}_{0.3}\text{Y}_{0.7}\text{F}_4$ [69]

$$x = 0.21887(8), \quad y = 0.41394(7), \quad z = 0.45618(4).$$

Multiplicity	Wyckoff letter		Coordinates	
Site Symmetry			$(0, 0, 0)+$	$(\frac{1}{2}, \frac{1}{2}, \frac{1}{2})+$
16	f	1	(1) x, y, z (2) $\bar{x} + \frac{1}{2}, \bar{y}, z + \frac{1}{2}$ (3) $\bar{y} + \frac{3}{4}, x + \frac{1}{4}, z + \frac{1}{4}$ (4) $y + \frac{3}{4}, \bar{x} + \frac{3}{4}, z + \frac{3}{4}$ (5) $\bar{x}, \bar{y}, \bar{z}$ (6) $x + \frac{1}{2}, y, \bar{z} + \frac{1}{2}$ (7) $y + \frac{3}{4}, \bar{x} + \frac{1}{4}, \bar{z} + \frac{1}{4}$ (8) $\bar{y} + \frac{3}{4}, x + \frac{3}{4}, \bar{z} + \frac{3}{4}$	
4	b	$\bar{4}$	$0, \frac{1}{4}, \frac{5}{8}$	$\frac{1}{2}, \frac{1}{4}, \frac{7}{8}$
4	a	$\bar{4}$	$0, \frac{1}{4}, \frac{1}{8}$	$\frac{1}{2}, \frac{1}{4}, \frac{3}{8}$

Table A.1: Crystallographic positions within the unit cell according to the space group $I4_1/a$, reproduced from [68] (no. 88, choice 2). The Re^{3+} ions occupy the sites with Wyckoff-Label 4b, Li^{3+} 4a and F^- 16f.

	c [\AA]	a [\AA]
LiTbF_4	10.873	5.181
LiYbF_4	10.59	5.132
LiTmF_4	10.64	5.15
LiDyF_4	10.83	5.189
LiHoF_4	10.75	5.175
LiYF_4	10.74	5.175
LiErF_4	10.70	5.162

Table A.2: Lattice constants of a few LiReF_4 compounds according to [70].

B Representation of the group S_4

The crystal field Hamiltonian in LiReF_4 is invariant under the symmetry $\bar{4}$ or S_4 in Schoenflies notation. The Eigenvalue problem can then be solved in the four subspaces according to the four irreducible representations A,B,E' and E''. The S_4 group is the cyclic group of the order 4 and contains following elements:

$$e, \quad s_4, \quad c_2 := s_4^2, \quad s_4^3$$

where s_4 is a 90° mirror-Rotation around the c-axis, i.e. can be written as the matrix

$$s_4 = \begin{pmatrix} 0 & -1 & 0 \\ 1 & 0 & 0 \\ 0 & 0 & -1 \end{pmatrix}.$$

The Operator \mathbf{J} transform like an axial vector, like $\mathbf{J} \rightarrow R\mathbf{J}$ under a rotation R but $\mathbf{J} \rightarrow \mathbf{J}$ under space inversion. The mirror rotation s_4 can be considered as an inversion plus a rotation and therefore one obtains the transformations

$$s_4 : \begin{array}{lll} x \mapsto y & J_x \mapsto -J_y & J_+ \mapsto iJ_+ \\ y \mapsto -x & J_y \mapsto J_x & J_- \mapsto -iJ_- \\ z \mapsto -z & J_z \mapsto J_z. \end{array}$$

Since the group is commutative, all representations are one dimensional. The character table is given as below and the subspaces can then be found in the canonical way by means of projectors determined from the characters.

χ	e	s_4	c_2	s_4^3
A	1	1	1	1
B	1	-1	1	-1
E'	1	i	-1	-i
E''	1	-i	-1	i

Bibliography

- [1] S. Sachdev, *Quantum Phase Transitions* (Cambridge University Press., Cambridge, 1999).
- [2] M. Vojta, Reports on Progress in Physics **66**, 2069 (2003).
- [3] S. L. Sondhi, S. M. Girvin, J. P. Carini, and D. Shahar, Rev. Mod. Phys. **69**, 315 (1997).
- [4] K. Binder and A. P. Young, Rev. Mod. Phys. **58**, 801 (1986).
- [5] J. Brooke, T. F. Rosenbaum, and A. G., Nature **413**, 610 (2001).
- [6] J. Brooke, D. Bitko, T. F. Rosenbaum, and G. Aeppli, Science **284**, 779 (1999).
- [7] S. Ghosh, T. Rosenbaum, G. Aeppli, and S. Coppersmith, Nature **425**, 48 (2003).
- [8] S. Ghosh, R. Parthasarathy, T. F. Rosenbaum, and G. Aeppli, Science **296**, 2195 (2002).
- [9] D. Bitko, T. F. Rosenbaum, and G. Aeppli, Phys. Rev. Lett. **77**, 940 (1996).
- [10] M. Schechter and N. Laflorencie, Physical Review Letters **97**, 137204 (2006).
- [11] H. M. Ronnow *et al.*, Science **308**, 389 (2005).
- [12] A. Kopp and S. Chakravarty, Nature Physics **1**, 53 (2005).
- [13] A. Tkachuk and V. Shumilin, Lasers and Electro-Optics Europe, 1994 Conference on 137 (28 Aug-2 Sep 1994).
- [14] G. L. Squires, *Introduction to the theory of thermal neutron scattering* (Dover Publications, Mineola, NY, 1996).
- [15] *Neutron and X-ray Spectroscopy*, edited by F. Hippert *et al.* (Springer, Dordrecht, 2006).

-
- [16] K. Kiefer, Diplomarbeit, Institut für Technische Physik, Universität des Saarlandes, Saarbrücken, 1997.
- [17] K. Kiefer, Dissertation, Institut für Technische Physik, Universität des Saarlandes, Saarbrücken, 2004.
- [18] D. H. Reich *et al.*, Phys. Rev. B **42**, 4631 (1990).
- [19] K. W. H. Stevens, Proceedings of the Physical Society Section A **65**, 209 (1952).
- [20] M. T. Hutchings, in *Solid State Physics*, edited by F. Seitz and D. Turnbull (Academic Press, New York, 1964), Vol. 16, Chap. Point-Charge Calculations of Energy Levels of Magnetic Ions in Crystalline Electric Fields, p. 227.
- [21] G. J. Bowden and R. G. Clark, Journal of Physics C: Solid State Physics **14**, L827 (1981).
- [22] J. Jensen and A. R. Mackintosh, *Rare Earth Magnetism: Structures and Excitations* (Clarendon Press, Oxford, 1991).
- [23] P. B. Chakraborty *et al.*, Physical Review B (Condensed Matter and Materials Physics) **70**, 144411 (2004).
- [24] H. M. Ronnow *et al.*, Physical Review B **75**, 054426 (2007).
- [25] A. Biltmo and P. Henelius, Physical Review B (Condensed Matter and Materials Physics) **76**, 054423 (2007).
- [26] Z. Slanič, D. P. Belanger, and J. A. Fernandez-Baca, Phys. Rev. Lett. **82**, 426 (1999).
- [27] D. Silevitch *et al.*, Nature **448**, 567 (2007).
- [28] S. Fishman and A. Aharony, Journal of Physics C: Solid State Physics **12**, L729 (1979).
- [29] S. M. A. Tabei *et al.*, Physical Review Letters **97**, 237203 (2006).
- [30] S. M. A. Tabei, F. Vernay, and M. J. P. Gingras, Physical Review B (Condensed Matter and Materials Physics) **77**, 014432 (2008).
- [31] M. Schechter, Physical Review B (Condensed Matter and Materials Physics) **77**, 020401 (2008).
- [32] P. Beauvillain, J. P. Renard, and P. E. Hansen, **10**, L709 (1977).
- [33] G. Mennenga, L. J. de Jong, and W. J. Huiskamp, J. Magn. Magn. Mat. **44**, 48 (1984).

-
- [34] J. Magariño, J. Tuchendler, P. Beauvillain, and I. Laursen, *Physical Review B* **21**, 18 (1980).
- [35] H. P. Christensen, *Phys. Rev. B* **19**, 6564 (1979).
- [36] P. E. Hansen, T. Johansson, and R. Nevald, *Phys. Rev. B* **12**, 5315 (1975).
- [37] S. Salaun *et al.*, *J. Phys.: Condensed Matter* **9**, 6941 (1997).
- [38] S. Gifeisman, A. Tkachuk, and V. Prizmak, *Optics and Spectroscopy* **44**, 68 (1978).
- [39] C. Görller-Walrand and K. Binnemans, in *Handbook on the Physics and Chemistry of Rare Earths, Chapter 155 Rationalization of crystal-field parametrization*, edited by J. K. A. Gschneidner and L. Eyring (North-Holland, Amsterdam, 1996), Vol. 23, p. 121.
- [40] H. P. Jenssen *et al.*, *Phys. Rev. B* **11**, 92 (1975).
- [41] H. P. Christensen, *Phys. Rev. B* **19**, 6573 (1979).
- [42] D. I. Abubakirov, K. Matsumoto, H. Suzuki, and M. S. Tagirov, *Journal of Physics: Condensed Matter* **20**, 395223 (4pp) (2008).
- [43] S. Al'tshuler, A. Kudryashov, M. Teplov, and D. Terpilovskii, *JETP Lett* **35**, 299 (1982).
- [44] A. Sugiyama, M. Katsurayama, Y. Anzai, and T. Tsuboi, *Journal of Alloys and Compounds* **408-412**, 780 (2006), proceedings of Rare Earths'04 in Nara, Japan.
- [45] C. Ancona-Torres, D. M. Silevitch, G. Aeppli, and T. F. Rosenbaum, *Physical Review Letters* **101**, 057201 (2008).
- [46] R. B. Griffiths, *Phys. Rev. Lett.* **23**, 17 (1969).
- [47] S. Lovesey, *Theory of neutron scattering from condensed matter* (Clarendon Press, Oxford, 1984).
- [48] A. Aharony, *Phys. Rev. B* **8**, 3363 (1973).
- [49] J. Als-Nielsen, *Phys. Rev. Lett.* **37**, 1161 (1976).
- [50] A. Das and B. K. Chakrabarti, *Reviews of Modern Physics* **80**, 1061 (2008).
- [51] G. E. Santoro, R. Martoncaronak, E. Tosatti, and R. Car, *Science* **295**, 2427 (2002).

-
- [52] D. H. Reich, T. F. Rosenbaum, and G. Aeppli, *Phys. Rev. Lett.* **59**, 1969 (1987).
- [53] J. A. Quilliam, S. Meng, C. G. A. Mugford, and J. B. Kycia, *Physical Review Letters* **101**, 187204 (2008).
- [54] J. A. Quilliam *et al.*, *Physical Review Letters* **98**, 037203 (2007).
- [55] N. V. Prokof'ev and P. C. E. Stamp, *Reports on Progress in Physics* **63**, 669 (2000).
- [56] P. C. E. Stamp and I. S. Tupitsyn, *Phys. Rev. B* **69**, 014401 (2004).
- [57] J. M. Luttinger and L. Tisza, *Phys. Rev.* **70**, 954 (1946).
- [58] C. Kraemer, Diplomarbeit, Laboratory for Neutron Scattering ETH&PSI, ETH Zurich, Zurich, 2006.
- [59] C. Kraemer, N. Nikseresht, K. Kiefer, and H. M. Rønnow, in preparation for *Nature Physics* (2009).
- [60] G. Ahlers, A. Kornblit, and H. J. Guggenheim, *Phys. Rev. Lett.* **34**, 1227 (1975).
- [61] J. Nikkel and B. Ellman, *Phys. Rev. B* **64**, 214420 (2001).
- [62] J. Villain, R. Bidaux, J. Carton, and R. Conte, *JOURNAL DE PHYSIQUE* **41**, 1263 (1980).
- [63] C. L. Henley, *Phys. Rev. Lett.* **73**, 2788 (1994).
- [64] S. J. White *et al.*, *Phys. Rev. Lett.* **71**, 3553 (1993).
- [65] A. Taroni, S. T. Bramwell, and P. C. W. Holdsworth, *Journal of Physics: Condensed Matter* **20**, 275233 (15pp) (2008).
- [66] L. A. S. Mól and B. V. Costa, *Physical Review B (Condensed Matter and Materials Physics)* **79**, 054404 (2009).
- [67] J. Piatek, Diplomarbeit, Laboratory for Quantum Magnetism (LQM), École Polytechnique Fédérale de Lausanne (EPFL), 2009.
- [68] *International Tables for Crystallography* (Kluwer, Dordrecht, 2002), Vol. A: Space-group symmetry.
- [69] K. Kjaer, J. Als-Nielsen, I. Laursen, and F. K. Larsen, *Journal of Physics: Condensed Matter* **1**, 5743 (1989).
- [70] S. K. Misra and J. Felsteiner, *Phys. Rev. B* **15**, 4309 (1977).

Acknowledgement

I would like to thank my direct supervisor, Prof. Henrik M. Rønnow giving me the chance to work on this project. He introduced me to the subject and it was a privilege to learn my first steps in neutron scattering from one of the leading experts in this field. Although he was involved also in many other project in parallel and was charged with the titanic challenge to build up a new Laboratory during this time, he tried to do always his best in supporting me. I appreciated his understanding also in controversial issues. Furthermore I am grateful that he render possible for me to work at the London Center of Nanotechnology for a while.

Especially I would like to to thank Prof. Joel Mesot and Prof. Manfred Sigrist for their advise, great support and promotion during all stages of my PhD.

This project was essentially based on experiments at large scale facilities. I am thankful for all the assistance I received from many responsables in charge for instruments as well as sample environment at SINQ, HZB, FRM2, ILL, IPNS and LLB. Further, I appreciate having the opportunity to perform complementary thermodynamic measurements together with Klaus Kiefer. Karl Krämer I thank for growing single crystals for our experiments. In particular I would like to acknowledge my coworkers at the Laboratory for Quantum Magnetism at EPFL and the many people of Laboratory of Neutron Scattering and PSI, who supported me in preparing and performing my work and with whom I shared serval interesting discussions.

My colleges Benedikt Thielemann, Julia Preu and Johannes Leiner I want to thank joining with me an office at PSI and LCN, and for having a nice and inspiring company during all these years. Especially Beni was a great companion in accomplishment of the PhD. I could benefit a lot, from his experience, scientific excellence and from the illuminating discussions we had about many aspect, also beyond science.

Great thanks go to my family, my friends, and first of all to Iris. I am thankful for their understanding and their vivid support I received during this hard working and ambivalent time.

Curriculum Vitae

Surname: Kraemer
First Name: Conradin
Date of Birth: 31.08.1981
From: Bern
Nationality: Swiss

1998-2001 Mathematisch-Naturwissenschaftliches
Gymnasium Neufeld in Bern.

2001-2006 Studies in Physics at ETH Zurich.

2006 Diploma-Thesis at
Laboratory for Neutron Scattering ETH&PSI.

2006 Graduating with Diploma in Physics ETH Zurich.

2006-2009 PhD student affiliated at
Laboratory for Neutron Scattering ETH&PSI,
Laboratory for Quantum Magnetism EPFL.

2008/2009 Visiting research student at
London Center for Nanotechnology.

2009 Dissertation submitted to ETH Zurich for
the degree of Doctor of Science.